DISSERTATION

submitted to the
Combined Faculty of Natural Sciences and Mathematics
of Heidelberg University, Germany
for the degree of
DOCTOR OF NATURAL SCIENCES

Put forward by

Sebastian Fritjof Thomas, M.Sc.
born in Frankfurt am Main

Oral examination: November 25, 2020

QUANTIFICATION OF BRAIN TISSUE OXYGENATION USING MAGNETIC RESONANCE IMAGING

—

SIMULATION AND IN VIVO STUDY

Referees: Prof. Dr. Lothar R. Schad
Prof. Dr. Peter Bachert

Für meine Eltern

ZUSAMMENFASSUNG

Der Sauerstoffverbrauch des Gehirns bietet wichtige Informationen über dessen Funktion und ist bei Erkrankungen wie Gehirntumoren für Therapieplanung und Verlaufskontrolle von erheblichem Interesse. Insbesondere der Sauerstoffextraktionsanteil (OEF) eignet sich als Biomarker, da er im gesunden Gewebe homogen ist, jedoch in Pathologien frühzeitig einen Kontrast entwickelt. Ziel dieser Arbeit war es, eine robustere Magnetresonanztomographie (MRT)-basierte Methode zur Bestimmung des OEF im Gehirn zu entwickeln und klinisch anzuwenden. Die Methode verwendet ein mathematisches Modell, das neben dem OEF auch von weiteren korrelierten Parametern abhängt. Dadurch reagiert die Rekonstruktion sehr empfindlich auf Rauschen und ist unter klinischen Bedingungen nicht anwendbar. In dieser Arbeit wurden daher zwei neue Ansätze untersucht: Die erste Methode erweitert den normalen Fitprozess um einen Regularisierungsterm, der eine Konvergenz der Parameter im physiologisch sinnvollen Bereich bevorzugt. Die zweite Methode basiert auf einem künstlichen neuronalen Netz (ANN), das an simulierten Daten trainiert und anschließend zur Rekonstruktion von in vivo Daten verwendet wurde. Beide Methoden waren in der Lage, in gesunden Probanden homogenere Karten im Vergleich zur Standardmethode zu ermitteln. Die Regularisierungsmethode ergab einen OEF von $(33.7 \pm 2.0)\%$ in grauer Hirnsubstanz (GM) und $(34.2 \pm 2.1)\%$ in weißer Hirnsubstanz (WM). Die ANN Methode ergab einen OEF von $(35.2 \pm 1.3)\%$ in GM und $(33.1 \pm 1.7)\%$ in WM. Im Rahmen von zwei in vivo Studien wurde der OEF bei Rauchern und bei Patienten mit Hirntumoren bestimmt. Bei den Rauchern zeigte der OEF keine signifikanten Unterschiede sowohl im Vergleich vor und nach dem Rauchen einer Zigarette als auch im Vergleich mit Nichtrauchern. Die Anwendung bei Patienten mit Hirntumoren ergab einen signifikant erhöhten OEF in der Tumorregion im Vergleich zur kontralateralen Seite ($p < 0.05$). Die vorgestellten Methoden führten unter klinischen Bedingungen zu präziseren Ergebnissen und könnten in der Zukunft eine klinische Implementierung der MRT-basierten Sauerstoffmessung ermöglichen.

ABSTRACT

The oxygen consumption of the brain provides important information about its function and is of particular interest for therapy planning and monitoring in diseases such as brain tumors. Especially, the oxygen extraction fraction (OEF) is suitable as a biomarker because it is homogeneous in healthy tissue but develops contrast early in pathologies. The aim of this work was to develop and clinically apply a more robust magnetic resonance imaging (MRI)-based method for the determination of OEF in the brain. The method uses a mathematical model that depends not only on the OEF but also on other correlated parameters. Thus, the reconstruction is very sensitive to noise and is not applicable under clinical conditions. In this thesis, two new approaches were investigated: The first method extends the normal fit process by a regularization term, which prefers a convergence of parameters in the physiologically meaningful range. The second method is based on an artificial neural network (ANN), which was trained on simulated data and subsequently used for the reconstruction of in vivo data. Both methods were able to produce more homogeneous maps in healthy subjects compared to the standard method. The regularization method found an OEF of $(33.7 \pm 2.0)\%$ in gray matter (GM) and $(34.2 \pm 2.1)\%$ in white matter (WM). The ANN method yielded an OEF of $(35.2 \pm 1.3)\%$ in GM and $(33.1 \pm 1.7)\%$ in WM. In two in vivo studies, the OEF was determined in smokers and in patients with brain tumors. In smokers, the OEF did not show significant differences both before and after smoking a cigarette and in comparison with never-smokers. The application in patients with brain tumors showed a significantly increased OEF in the tumor region compared to the contralateral side ($p < 0.05$). The presented methods led to more precise results under clinical conditions and may allow a clinical implementation of MRI-based oxygen measurement in the future.

ACKNOWLEDGEMENTS

Of course, this work would not have been possible without the help, advice and support of many others:

First of all, I would like to thank Prof. Lothar Schad for giving me the opportunity to write my PhD thesis at his chair. I am particularly grateful for his trust, support and the provided space for creativity. I would also like to thank Prof. Bachert for kindly agreeing to review this thesis and Dr. Sebastian Domsch for helping me get started at CKM.

Furthermore, I would like to thank my cooperation partners at the Zentralinstitut für Seelische Gesundheit: Prof. Sabine Vollstädt-Klein for all the advice about the study design and statistics, Alycia Lee and Natalie Hartig for their help and the entertaining talks during the evening scan times and Michael Rieß for sharing his knowledge about the practical aspects of MR scanning. I gratefully acknowledge the clinical cooperation with the Department of Neuroradiology, especially Dr. Alex Förster and Dr. Bettina Mürle for their help measuring the tumor patients.

For kindly proofreading this thesis, I would like to thank Dr. Tanja Uhrig, Dr. Simon Hubertus, Dr. Matthias Malzacher and Dr. Ruomin Hu.

Neben der fachlichen Zusammenarbeit möchte ich mich beim gesamten CKM vor allem für die einzigartigen Erlebnisse bedanken, die ich im Laufe meiner Promotionszeit mit euch haben durfte. Die interessanten Diskussionen, wilden Kickerrunden und Boulderabende, lustigen Konferenz- und Urlaubsreisen werden mir immer in Erinnerung bleiben. Insbesondere möchte ich hierbei Simon und Matze hervorheben, mit denen ich das beste Büro der Welt teilen durfte. Vielen Dank für die tolle Freundschaft, die stete Hilfsbereitschaft, die verrückten Funfacts und die grandiosen Witze!

Außerdem danke ich all meinen Freunden aus Mannheim und Frankfurt, insbesondere Jan und David für die mittlerweile über mehrere Dekaden gepflegte Freundschaft.

Ein besonderer Dank gilt natürlich meiner Familie: Tatjana, Kevin und am allermeisten meinen Eltern für die unglaubliche Unterstützung. Ihr seid meine größten Vorbilder!

CONTENTS

LIST OF FIGURES

LIST OF TABLES

ACRONYMS

ANN	Artificial Neural Network
ASL	Arterial Spin Labeling
BOLD	Blood Oxygen Level Dependent
CBF	Cerebral Blood Flow
CMRO2	Cerebral Metabolic Rate of Oxygen
CSF	Cerebrospinal Fluid
DBV	Deoxygenated Blood Volume
DCE	Dynamic Contrast Enhanced
DICOM	Digital Imaging and Communications in Medicine
EPI	Echo Planar Imaging
FID	Free Induction Decay

fMRI	functional Magnetic Resonance Imaging
FOV	Field of View
GESSE	Gradient Echo Sampled Spin Echo
GM	Gray Matter
GRE	Gradient Echo
Hb	Hemoglobin
Hct	Hematocrit
LD	Labeling Duration
LS	Least Squares
mGRE	multi Gradient Echo
MNI	Montreal Neurological Institute
MP	multiparameter
MPRAGE	Magnetization Prepared Rapid Gradient Echo
MR	Magnetic Resonance
MRI	Magnetic Resonance Imaging
mSE	multi Spin Echo
NMR	Nuclear Magnetic Resonance
OEF	Oxygen Extraction Fraction
pCASL	pseudo-Continuous Arterial Spin Labeling
PD	Proton Density
PET	Positron Emission Tomography
PLD	Post-Labeling Delay
qBOLD	quantitative Blood Oxygen Level Dependent
QSM	Quantitative Susceptibility Mapping
ROI	Region of Interest
RF	Radio Frequency
SD	Standard Deviation
SE	Spin Echo
SNR	Signal to Noise Ratio
SSE	Sum of Squares Error
TE	Echo Time
TR	Repetition Time
WHO	World Health Organization
WM	White Matter
ZI	Zentralinstitut für Seelische Gesundheit

1 INTRODUCTION

The human brain consumes about 50 ml of O_2 per minute, which accounts for about 20% of the body's total oxygen consumption [Rink and Khanna, 2011]. The Cerebral Metabolic Rate of Oxygen ($CMRO_2$) is determined by the Cerebral Blood Flow (CBF) and the Oxygen Extraction Fraction (OEF); the latter representing the ratio of consumed to delivered oxygen in the tissue. Impairments of the oxygen supply can lead to severe damage. If the CBF is interrupted, consciousness is lost within 10 seconds and irreversible damage to brain tissue occurs within minutes [Saver, 2006].

Many pathologies are associated with an altered oxygenation, such as multiple sclerosis [Fan et al., 2014] or stroke [An et al., 2014; Ibaraki et al., 2004]. In particular, for the diagnosis and treatment of brain cancer, the tissue oxygenation yields valuable information. Glioblastoma multiforme is the most aggressive type of brain cancer with a median survival time of only about 12 to 15 months [Wen and Kesari, 2008]. The treatment usually consists of a surgical resection and subsequent radio- and chemotherapy. Glioblastomas infiltrate the surrounding tissue, which has a huge impact on tissue oxygenation and perfusion. Knowledge about the oxygenation can be used for tumor grading [Stadlbauer et al., 2017] and is important for radiotherapy since the radiosensitivity of the tissue is affected by its oxygenation level [Hockel et al., 1996; Rofstad et al., 2000; Wang et al., 2006].

Apart from pathologies, the oxidative brain metabolism can be affected by substances that are administered to the body, such as nicotine via cigarette smoking [Vafaee et al., 2015]. Although smoking is a widespread habit all over the world, resulting in 8 million preventable deaths globally in 2017 [Stanaway et al., 2018], there is still no consensus about the effects of nicotine administration on the brain metabolism. So far, Positron Emission Tomography (PET) studies using ^{15}O as a tracer have found the global CBF to decrease [Yamamoto et al., 2003], increase [Skinhoj et al., 1973; Vafaee et al., 2015] and remain unchanged [Shinohara et al., 2006] after smoking. In addition to these whole brain changes in brain metabolism, regional changes in CBF have been found for the visual cortex, thalamus and cerebellum in several studies [Domino et al., 2000, 2004; Rose et al., 2003; Zubieta et al., 2005]. However, a general agreement has not been reached here, either. $CMRO_2$ has similarly shown smoking-induced global and regional changes when examined with PET; also yielding mixed findings [Skinhoj et al., 1973; Vafaee et al., 2015]. Although both CBF and $CMRO_2$ are measures of general brain metabolism, they are not necessarily closely coupled for smoking-evoked changes, where changes in CBF are often found to exceed those in $CMRO_2$. Their ratio, the OEF, has seldom been examined with regard to smoking [Skinhoj et al., 1973]

and might provide another useful assessment of smoking-induced changes in brain oxygenation and perfusion.

^{15}O PET is considered to be the gold standard for oxygenation measurements. However, this modality comes along with several disadvantages, such as the exposure to ionizing radiation and low resolution. Moreover, the half-life of ^{15}O is only 2 minutes, which renders the technique expensive and hinders wide accessibility. This encourages the use of Magnetic Resonance Imaging (MRI)-based methods, which could be easily implemented into the clinical routine.

The main advantages of MRI compared with other modalities are its non-invasiveness, the lack of ionizing radiation and the ability to create a strong contrast between different kinds of soft tissue. In particular for applications in the brain, it enables the acquisition of tomographic images with high resolution and contrast. In addition to morphological imaging offering insight into the anatomical information of tissue structure, a variety of functional imaging methods is applied in clinical routine. Functional imaging methods are sensitive to physical and physiological processes occurring in living tissue, such as diffusion, perfusion or oxygen consumption. Measuring these functional processes is especially valuable if the tissue functionality has been altered by disease progression, while the macroscopic tissue structure has not yet been affected.

In order to measure the oxygen consumption using MRI, the Blood Oxygen Level Dependent (BOLD) contrast is utilized, which was discovered by Ogawa et al. [1990]. It derives from the different magnetic properties of oxygenated and deoxygenated hemoglobin [Pauling and Coryell, 1936]. The change in the magnetic susceptibility leads to an oxygenation dependent dephasing of the Magnetic Resonance (MR) signal. The deoxygenated blood acts as an endogenous contrast agent originating from the body itself. The BOLD contrast is routinely employed for measuring brain activity in functional Magnetic Resonance Imaging (fMRI), which detects small changes in brain oxygenation as a response to the task-based stimulation of individual brain regions. However, quantitative oxygenation measurements of the brain's baseline state are rarely performed. The quantification of the BOLD effect was first theoretically described by Yablonskiy and Haacke [1994]. The influence on the MR signal was mathematically modeled by assuming the blood vessel network in the brain to consist of randomly oriented paramagnetic cylinders and calculating their influence on the magnetic field. By fitting the quantitative Blood Oxygen Level Dependent (qBOLD) model to the MR data, the model parameters can be extracted. Using a special acquisition sequence called GESSE theoretically allows for a separation of different relaxation processes influenced by quantities, such as the OEF and the Deoxygenated Blood Volume (DBV) [Yablonskiy, 1998].

With this method, promising results have already been achieved in vivo [An and Lin, 2002a; He et al., 2008]. However, due to the required high Signal to Noise Ratio (SNR), very long measurement times are necessary. This leads to poor quantification quality for clinically reasonable measurement settings.

Until now, the standard reconstruction of oxygenation parameters from the GESSE sequence uses a voxel-wise Least Squares (LS) fit of the qBOLD model to the time evolution of the acquired data. The main challenge of bringing this method into clinical use lies in the robust parameter reconstruction while keeping the acquisition time short. In particular, the strong interdependence of OEF and DBV can lead to a large variation of both parameters in the standard LS regression. One possibility is to extend the measurement by additional MR sequences. This way, the fit parameters can be determined more reliably via independent measurements. This approach is referred to as multiparameter (MP) method [Christen et al., 2011, 2012a].

In this work, the main task was to tackle the lack of robustness of the qBOLD method using GESSE. Two techniques to mitigate the sensitivity to noise of the measured data were explored in order to improve the reconstruction quality for a limited clinical acquisition time:

First, a regularization term was added to the LS reconstruction, which incorporates prior information into the fit. Thus, the fit was brought to converge in a physiologically meaningful range yielding more realistic results. The regularization method was first demonstrated in vivo on healthy volunteers. Here, the effects of different weighting factors on the reconstructed parameters were visualized. For a quantitative analysis, the accuracy and precision of the reconstruction of OEF and DBV were assessed in a simulation phantom of the brain. In contrast to the in vivo data, the ground truth was known in this case.

The second approach employs an Artificial Neural Network (ANN) for the parameter reconstruction. ANNs are increasingly used in medical imaging for applications, such as pattern recognition or segmentation [Nasrabadi, 2007; Zöllner et al., 2010; Maier et al., 2019; Schnurr et al., 2019]. In particular for oxygenation mapping, promising results have already been demonstrated [Domsch et al., 2018; Hubertus et al., 2019b]. The underlying idea is that the network is trained on data with a known ground truth. This allows the network to learn the features within the data that predict the parameters in question. Once it has learned the relationship between data and parameters, the ANN can be applied to new data. For training, simulated data can be used, which has the advantage that large data sets can easily be generated. In case of qBOLD, the trained network is used for the regression of acquired in vivo data and thus for the estimation of OEF and DBV.

These novel methods were applied within two in vivo studies: In the smoker study, a group of 20 smokers and a group of 10 never-smokers were examined. The smokers were scanned once before and after smoking one cigarette. This way, a comparison could be drawn between smokers in the pre- and post-smoking state for examining acute effects. Additionally, chronic effects of smoking could be assessed by comparing the smokers to never-smokers. In the tumor study, a group of three brain tumor patients were examined. The parameters OEF, CBF and $CMRO_2$ in the tumor region were compared to the healthy tissue on the contralateral side.

2 BASIC PRINCIPLES

This chapter gives a brief overview of the theoretical concepts underlying this thesis. It starts with the fundamental description of the nuclear spin and its behavior in a magnetic field and continues with the application of radio frequency fields, in order to excite a measurable signal. Further developments in the spatial encoding of the signal allows the creation of tomographic images, which is known as MRI. The fact that the signal is dependent on many external factors enables the use of MRI in a great variety of tasks.

In particular, the application in oxygenation mapping is covered. Furthermore, physiological basics of brain metabolism are briefly introduced.

2.1 NUCLEAR MAGNETIC RESONANCE

The spin – as an intrinsic property of electrons – was first discovered with the Stern-Gerlach experiment in 1922. The analog property of the *nuclear* spin was detected in the hydrogen nucleus by Rabi in 1938. In 1946, Bloch and Purcell were able to manipulate nuclear spins with radio frequency fields and detect the induced signal. This discovery formed the basis for Nuclear Magnetic Resonance (NMR) and was honored with the Nobel Prize for Physics in 1952. The following description is presented in analogy to Levitt [2008].

2.1.1 *Nuclear Spin*

Atomic nuclei consist of protons and neutrons. Similar to their mass or electric charge, they both have an intrinsic property called spin associated with the quantum number $s = 1/2$. The spin is a form of angular momentum, although no rotational motion is involved as described by the classical angular momentum. The total angular momentum of a nucleus is determined by the sum over all protons and neutrons. In order to be relevant for NMR experiments, the spins of a nucleus must not cancel out each other. The resulting nuclear spin $\vec{I} > 0$ is associated with a magnetic moment

$$\vec{\mu} = \gamma \vec{I} \quad . \tag{2.1}$$

The proportionality factor is called gyromagnetic ratio γ and is defined as

$$\gamma = g \cdot \frac{\mu_N}{\hbar} \tag{2.2}$$

with the nucleus-specific g-factor, the reduced Planck constant

$$\hbar = \frac{h}{2\pi} = 1.0545 \cdot 10^{-34}\,\mathrm{Js} \tag{2.3}$$

Table 2.1: List of several nuclei that occur in the human body with their spin, magnetic moment, gyromagnetic ratio and relative abundance in the body. Table adapted from [Haacke et al., 1999].

Nucleus	I	μ/μ_N	$\gamma/2\pi$ [MHz/T]	c [mol/l]
^{1}H	1/2	2.79	42.58	88
^{23}Na	3/2	2.22	11.27	$80 \cdot 10^{-3}$
^{31}P	1/2	1.13	17.25	$75 \cdot 10^{-3}$
^{17}O	5/2	-1.89	-5.77	$17 \cdot 10^{-3}$
^{19}F	1/2	2.63	40.08	$4 \cdot 10^{-6}$

and the nuclear magneton μ_N

$$\mu_N = \frac{e\hbar}{2m_p} \quad . \tag{2.4}$$

Here, the elementary charge $e = 1.602 \cdot 10^{-19}\,\mathrm{C}$ and the proton mass $m_p = 1.673 \cdot 10^{-27}\,\mathrm{kg}$ are used. Inserting the g-factor for protons $g_p = 5.586$, the gyromagnetic ratio results to

$$\gamma = 267.513 \cdot 10^{-6}\,\frac{\mathrm{rad}}{\mathrm{s \cdot T}} \quad . \tag{2.5}$$

Several nuclei that occur in the human body are listed in Table 2.1 with their respective magnetic properties.

In order to understand the quantum mechanical description of the spin, the angular momentum operator needs to be considered. The three components of the spin angular momentum operator $\hat{I}$ fulfill the cyclic commutation relationship

$$\left[\hat{I}_x, \hat{I}_y\right] = i\hbar\epsilon_{xyz}\hat{I}_z \tag{2.6}$$

with ϵ_{xyz} denoting the Levi-Civita symbol. Furthermore, it can be shown that the operators $\hat{I}^2$ and $\hat{I}_z$ commute

$$\left[\hat{I}_z, \hat{I}^2\right] = 0 \quad . \tag{2.7}$$

Without loss of generality, only the component along the z-axis is considered. Therefore, mutual eigenstates exist for $\hat{I}^2$ and $\hat{I}_z$. These eigenstates are determined by two quantum numbers I and m. They can take the values

$$I = 0, \frac{1}{2}, 1, \frac{3}{2}, ... \tag{2.8}$$

$$m = -I, -I+1, ..., I-1, I \quad . \tag{2.9}$$

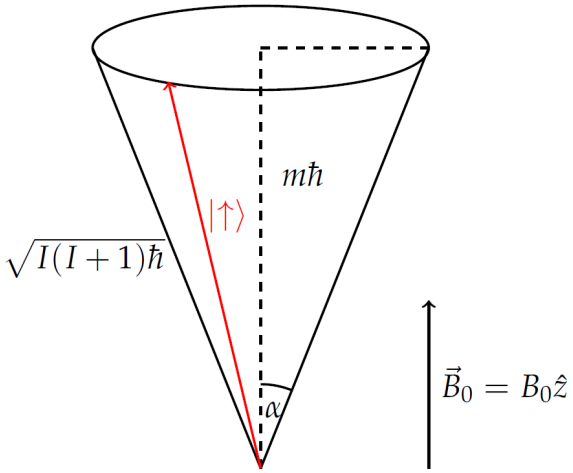

Figure 2.1: The magnitude and the projection onto the z-axis of the proton nuclear spin in the spin-up state. It follows an opening angle of the cone of $\alpha = 54.7°$. Figure adapted from Hubertus [2019].

The eigenstates $|I, m\rangle$ – written in Dirac notation – follow the eigenequations

$$\hat{I}^2|I, m\rangle = \hbar^2 I(I+1)|I, m\rangle \tag{2.10}$$

$$\hat{I}_z|I, m\rangle = \hbar m|I, m\rangle \quad . \tag{2.11}$$

The nuclear spin quantum number I determines the number of allowed states of m, i. e. $(2I+1)$. The quantum number m describes the spatial projection onto the z-axis in units of $\hbar$. The squared magnitude of $\hat{I}$ is determined by $I(I+1)\hbar$, as depicted in Figure 2.1.

Considering the hydrogen nucleus, which consists of a single proton, the nuclear spin $I = s = \frac{1}{2}$. Therefore, m can take two values

$$m = \pm\frac{1}{2} \quad . \tag{2.12}$$

Without an external magnetic field, the states are degenerated. Note that in the context of NMR and MRI, the magnetic flux density $\vec{B}$ is commonly referred to as magnetic field.

2.1.2 *Zeeman Effect*

When an external magnetic field is present, the energy levels split up and are no longer degenerated. This is known as Zeeman Effect. The splitting of the energy levels of the hydrogen nucleus is depicted in Figure 2.2. These two eigenstates can be described as spin-up $|1/2, +1/2\rangle = |\uparrow\rangle$ and spin-down $|1/2, -1/2\rangle = |\downarrow\rangle$. Hereinafter, it is assumed that the external magnetic field is oriented along the z-direction

$$\vec{B}_0 = B_0\hat{z} \quad . \tag{2.13}$$

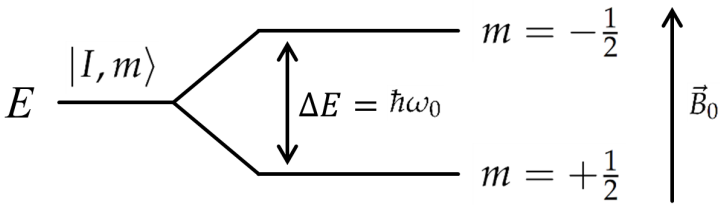

Figure 2.2: Splitting of the energy levels of the hydrogen nucleus from a degenerated state into two distinct states in the presence of an external magnetic field. The lower energy state is the spin-up state, which is parallel to the magnetic field. The higher energy level is the spin-down state, which is antiparallel. The energy difference ΔE arises.

Using the two eigenvectors as a basis, the eigenequations can be formulated

$$\hat{I}^2|\uparrow\rangle = \frac{3}{4}\hbar^2|\uparrow\rangle \tag{2.14}$$

$$\hat{I}^2|\downarrow\rangle = \frac{3}{4}\hbar^2|\downarrow\rangle \tag{2.15}$$

$$\hat{I}_z|\uparrow\rangle = +\frac{1}{2}\hbar|\uparrow\rangle \tag{2.16}$$

$$\hat{I}_z|\downarrow\rangle = -\frac{1}{2}\hbar|\downarrow\rangle \quad . \tag{2.17}$$

The three angular momentum operators can be expressed as matrices using that eigenbasis

$$\hat{I}_x = \frac{\hbar}{2}\begin{pmatrix} 0 & 1 \\ 1 & 0 \end{pmatrix}, \quad \hat{I}_y = \frac{\hbar}{2i}\begin{pmatrix} 0 & 1 \\ -1 & 0 \end{pmatrix}, \quad \hat{I}_z = \frac{\hbar}{2}\begin{pmatrix} 1 & 0 \\ 0 & -1 \end{pmatrix} \quad . \tag{2.18}$$

For calculating the energy levels of the two states, the Hamiltonian $\hat{\mathcal{H}}$ needs to be defined. The Hamiltonian for the interaction of a spin with a static field B_0 can be expressed using Equation 2.1

$$\hat{\mathcal{H}} = -\hat{\vec{\mu}} \cdot \vec{B}_0 = -\gamma B_0 \hat{I}_z \quad . \tag{2.19}$$

In this case, the time-independent Schrödinger equation can be applied

$$\hat{\mathcal{H}}|\psi\rangle = E|\psi\rangle \quad . \tag{2.20}$$

By inserting Equation 2.19 and the individual spin states $|\uparrow\rangle$ and $|\downarrow\rangle$, the energy levels can be determined

$$E_\uparrow = -\frac{1}{2}\hbar\gamma B_0 \tag{2.21}$$

$$E_\downarrow = +\frac{1}{2}\hbar\gamma B_0 \tag{2.22}$$

with the difference between these levels

$$\Delta E = \hbar\gamma B_0 \quad . \tag{2.23}$$

This energy gap can be overcome by the absorption or emission of a photon. The corresponding frequency is called Larmor frequency and is defined as

$$\omega_0 = \gamma B_0 \quad . \tag{2.24}$$

It plays a crucial role as the resonance frequency in all NMR and MRI experiments. At a field strength of $B_0 = 3\,\mathrm{T}$ and with the gyromagnetic ratio for protons, the Larmor frequency amounts to $f_0 = \frac{\omega_0}{2\pi} = 127.7\,\mathrm{MHz}$.

2.1.3 *Macroscopic Magnetization*

When performing an NMR experiment, not a single spin but a macroscopic volume consisting of a large quantity of spins is considered. Assuming thermal equilibrium, the occupation probability p_m of the Zeeman states is described by the Boltzmann statistics

$$p_m = \frac{1}{Z} \cdot e^{\frac{-E_m}{k_B T}} \tag{2.25}$$

with the Boltzmann constant $k_B = 1.38 \cdot 10^{-23}\,\mathrm{J/K}$, the temperature T and the state sum

$$Z = \sum_m e^{\frac{-E_m}{k_B T}} \quad . \tag{2.26}$$

For protons, the occupation ratio of the higher and lower energy state can thereby be calculated as

$$\frac{N_{m=-1/2}}{N_{m=+1/2}} = e^{\frac{-\Delta E}{k_B T}} = e^{\frac{-\gamma \hbar B_0}{k_B T}} \quad . \tag{2.27}$$

Assuming the body temperature of $T = 310\,\mathrm{K}$ and a field strength of $B_0 = 3\,\mathrm{T}$, the occupation ratio yields a spin excess for the lower energy state of only about $2 \cdot 10^{-5}$. However, this small fraction is compensated by the large amount of spins in a typical sample. For example, 1 ml of water contains a number of hydrogen nuclei in the order of 10^{20}. Thus, it is justified to consider a macroscopic magnetization M_0. An expression for M_0 can be found in accordance with Curie's law

$$M_0 \approx \frac{\rho \gamma^2 \hbar^2}{4 k_B T} B_0 \tag{2.28}$$

with the spin density ρ and the assumption that $k_b T \gg \gamma \hbar B_0$, which is valid at room temperature. It can be concluded that the macroscopic net magnetization is approximately proportional to the external magnetic field and inversely proportional to the temperature. As a macroscopic quantity, the magnetization vector is treated classically from now on.

2.1.4 *Signal Excitation*

In the classical picture, all the spins within the sample are randomly oriented except for a small net magnetization vector that points along the z-axis. The

magnetic moments in all other directions cancel each other out because there is no phase coherence among them. The net magnetization aligned with the external magnetic field, however, is not sufficient to measure a signal.

Let us consider a magnetization vector in an external magnetic field

$$\frac{\mathrm{d}\vec{M}}{\mathrm{d}t} = \vec{M} \times \gamma \vec{B}_0 \quad . \tag{2.29}$$

In case of the magnetization vector being parallel to the magnetic field, the torque will be zero. On the other hand, if there exists a component of $\vec{M}$ perpendicular to $\vec{B}_0$, the magnetization vector will perform a precession motion around the z-axis with the Larmor frequency ω_0. This is consistent with the quantum mechanical derivation for a single spin.

In order to measure a signal, the magnetization vector must be tilted away from its equilibrium position. This can be achieved by using a transmit coil, which emits a Radio Frequency (RF) pulse. This pulse must be perpendicular to $\vec{B}_0$ and tuned to the Larmor frequency in order to be resonant to the precession.

Under the condition that the RF field is left circularly polarized with the frequency ω_1 in the x-y-plane, $\vec{B}_1$ can be written as

$$\vec{B}_1 = \begin{pmatrix} B_1 \cos(\omega_1 t) \\ -B_1 \sin(\omega_1 t) \\ 0 \end{pmatrix} \quad . \tag{2.30}$$

In this case, Equation 2.29 can be extended to

$$\frac{\mathrm{d}\vec{M}}{\mathrm{d}t} = \vec{M} \times \gamma(\vec{B}_0 + \vec{B}_1) \tag{2.31}$$

$$= \vec{M} \times \gamma \begin{pmatrix} B_1 \cos(\omega_1 t) \\ -B_1 \sin(\omega_1 t) \\ B_0 \end{pmatrix} \quad . \tag{2.32}$$

The resulting motion can be described in a simpler way by changing the reference frame. Thus, we define a rotating frame of reference with the angular velocity $-\omega_1$ around the z-axis. Now Equation 2.31 becomes

$$\frac{\mathrm{d}\vec{M}'}{\mathrm{d}t} = \vec{M}' \times \gamma \begin{pmatrix} B_1 \\ 0 \\ B_0 - \frac{\omega_1}{\gamma} \end{pmatrix} \quad . \tag{2.33}$$

It follows that the z-component of the effective magnetic field will disappear if the RF field is applied with the Larmor frequency $\omega_1 = \omega_0$. The precession will now take place around the x'-axis, which results in the magnetization vector being tilted away from the z-axis.

By adjusting the RF pulse in terms of its amplitude B_1 and its duration τ, a certain flip angle α can be generated

$$\alpha = \gamma \int_0^\tau B_1(t)\mathrm{d}t \quad . \tag{2.34}$$

In case of rectangular excitation pulses and for small flip angles, this simplifies to

$$\alpha = \gamma B_1 \tau \quad . \tag{2.35}$$

2.1.5 *Relaxation*

As soon as the magnetization is no longer manipulated by a B_1 field, relaxation processes begin. These ensure that the magnetization returns to the initial state. A distinction is made between effects that affect the longitudinal (parallel to B_0) and the transverse component (perpendicular to B_0). The former are referred to as spin-lattice relaxation and are associated with the time constant T_1. The latter are called spin-spin relaxation with the time constant T_2.

SPIN-LATTICE RELAXATION This type of relaxation occurs due to the fact that the energetically most favorable state for the magnetization is parallel to B_0. In order for the longitudinal component to change, energy must be released. Since the protons are in thermal contact with the surrounding tissue, energy can be transferred to it via thermal motion in the form of vibration and rotation. The name spin-lattice relaxation comes from the fact that the surrounding medium in the beginning of NMR was usually a solid. The process can be described by

$$\frac{\mathrm{d}M_z}{\mathrm{d}t} = \frac{1}{T_1} \cdot (M_0 - M_z) \tag{2.36}$$

with the initial magnetization M_0 and the relaxation constant T_1. A solution for this differential equation is the exponential function

$$M_z(t) = M_z(0) \cdot e^{-t/T_1} + M_0 \cdot (1 - e^{-t/T_1}) \tag{2.37}$$

with the longitudinal magnetization at the beginning of the relaxation process $M_z(0)$. A visualization of this equation can be found in Figure 2.3. T_1 is dependent on the type of surrounding tissue as well as the magnetic field strength. The reason is that a more efficient energy transfer leads to a faster relaxation. The efficiency of the energy transfer is determined by how well the tumbling rate ω_{tum} of the tissue matches the Larmor frequency. Typical relaxation times for several tissues are listed in Table 2.2.

The return of the magnetization vector towards the z-axis inevitably leads to a decrease of the transverse component. However, there are additional effects that lead to a transverse relaxation, which are covered in the next paragraph.

SPIN-SPIN RELAXATION Immediately after excitation, the spins are in the same phase of their precession motion. They add up to a net transverse magnetization. However, this phase coherence is lost if the spins experience

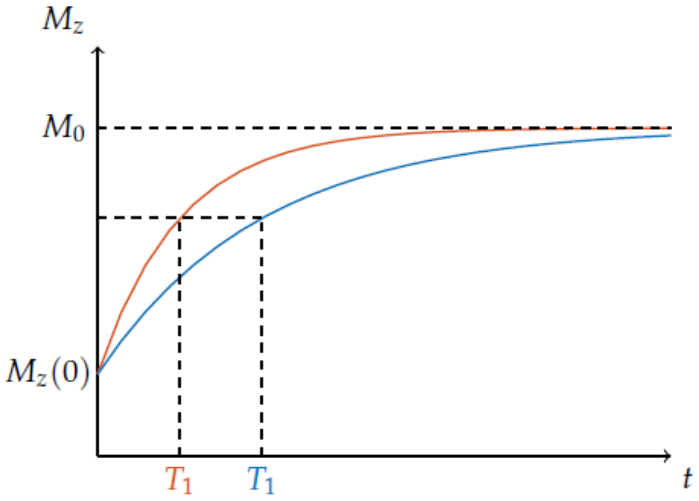

Figure 2.3: Relaxation of the longitudinal component of the magnetization to its initial state described by an exponential function. Figure adapted from Hubertus [2019].

different magnetic fields and thus precession frequencies. Magnetic field fluctuations occur since the spins influence each other via the dipole-dipole interaction randomly over time as a result of the Brownian motion. These random changes lead to a dephasing of the spins and a loss in transverse magnetization. The process is depicted in Figure 2.4.

The relaxation can be described by

$$\frac{\mathrm{d}\vec{M}_{xy}}{\mathrm{d}t} = -\frac{1}{T_2} \cdot \vec{M}_{xy} \tag{2.38}$$

in the rotating frame of reference. This equation is solved by the exponential function

$$\vec{M}_{xy} = \vec{M}_{xy}(0) \cdot e^{-t/T_2} \tag{2.39}$$

with the initial transverse magnetization $M_{xy}(0)$ and the relaxation constant T_2. The transverse signal decay is visualized in Figure 2.5. The time constant T_2 is almost independent of the external magnetic field and depends mainly on the surrounding tissue. At a low ω_{tum} the dipole fields do not fluctuate as much. A significant phase difference can be acquired within a short time. With increasing tumbling rate, however, these fluctuations are more and more averaged out. In a solid, the dipole fields are rather static and, therefore, T_2 is shorter compared to liquids. Typical values are given in Table 2.2.

RELAXATION TIME T_2^* Additionally to the tissue specific T_2 effect, spin dephasing can also occur due to external magnetic field inhomogeneities. If these inhomogeneities are static, the signal loss caused by them can be restored using a Spin Echo (SE), which will be described in Section 2.1.8. The

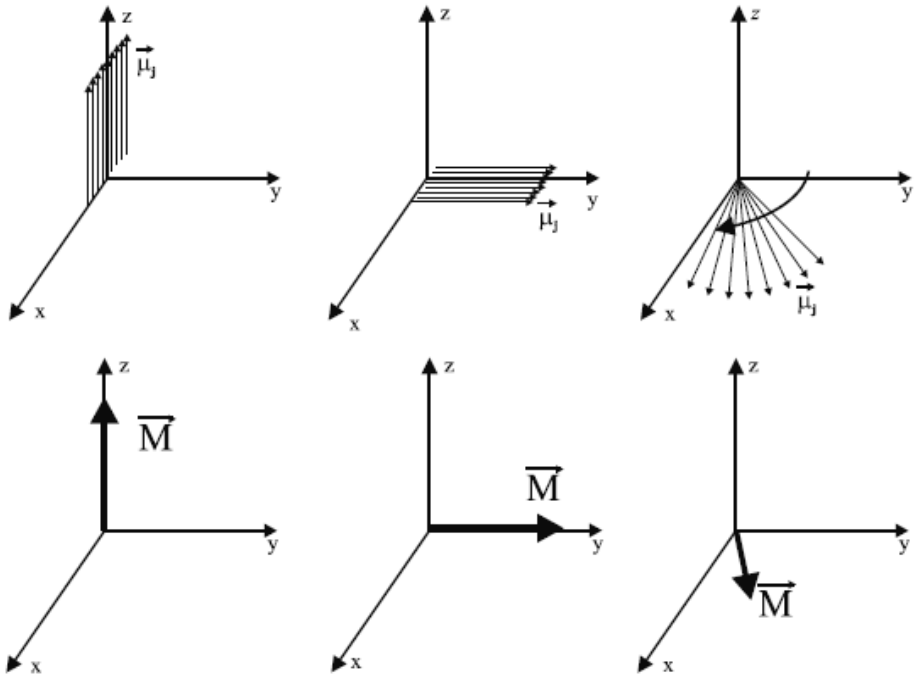

Figure 2.4: Loss of phase coherence of the spins due to random magnetic field fluctuations. The result is a decrease of the transverse magnetization component. Figure adapted from Haacke et al. [1999].

Table 2.2: List of longitudinal and transverse relaxation times of several tissues in the human body at 1.5 T. Table adapted from Haacke et al. [1999].

Tissue	T_1 [ms]	T_2 [ms]
gray matter (GM)	950	100
white matter (WM)	600	80
muscle	900	50
cerebrospinal fluid (CSF)	4500	2200
fat	250	60
arterial blood	1200	200
venous blood	1200	100

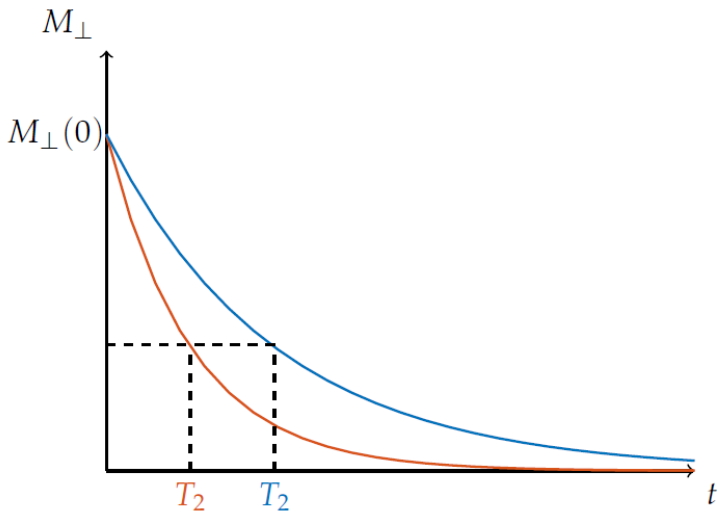

Figure 2.5: Relaxation of the transverse component of the magnetization. Figure adapted from Hubertus [2019].

total transverse relaxation time T_2* consists of both the irreversible relaxation time T_2 and the reversible relaxation time T_2′

$$\frac{1}{T_2{}^*} = \frac{1}{T_2} + \frac{1}{T_2{}'} \quad . \tag{2.40}$$

Instead of using the relaxation times, it is often more convenient to use the relaxation rates

$$R_2{}^* = R_2 + R_2{}' \quad . \tag{2.41}$$

2.1.6 *Bloch Equations*

The differential equations describing the interaction of the magnetization with the external magnetic field and the relaxation effects can be combined. This vector equation is called Bloch equation

$$\frac{\mathrm{d}\vec{M}}{\mathrm{d}t} = \gamma\vec{M} \times \vec{B} + \frac{1}{T_1}(M_0 - M_z)\hat{z} - \frac{1}{T_2}\vec{M}_{xy} \tag{2.42}$$

with its components

$$\frac{\mathrm{d}M_x}{\mathrm{d}t} = \gamma(\vec{M} \times \vec{B})_x - \frac{M_x}{T_2} \tag{2.43}$$

$$\frac{\mathrm{d}M_y}{\mathrm{d}t} = \gamma(\vec{M} \times \vec{B})_y - \frac{M_y}{T_2} \tag{2.44}$$

$$\frac{\mathrm{d}M_z}{\mathrm{d}t} = \gamma(\vec{M} \times \vec{B})_z - \frac{M_0 - M_z}{T_1} \quad . \tag{2.45}$$

By assuming a constant external magnetic field in z-direction, it follows

$$\frac{\mathrm{d}M_x}{\mathrm{d}t} = \omega_0 M_y - \frac{M_x}{T_2} \tag{2.46}$$

$$\frac{\mathrm{d}M_y}{\mathrm{d}t} = \omega_0 M_x - \frac{M_y}{T_2} \tag{2.47}$$

$$\frac{\mathrm{d}M_z}{\mathrm{d}t} = \frac{M_0 - M_z}{T_1} \tag{2.48}$$

using the Larmor frequency $\omega_0 = \gamma B_0$. The last equation is the same as Equation 2.36 and its solution is given by Equation 2.37. The x- and y-components can be combined in the complex formulation

$$M_+(t) = M_x(t) + iM_y(t) \tag{2.49}$$

leading to the differential equation

$$\frac{\mathrm{d}M_+}{\mathrm{d}t} = -(i\omega_0 + \frac{1}{T_2}) \cdot M_+ \tag{2.50}$$

which can be solved by

$$M_+(t) = M_+(0) \cdot e^{-i(\omega_0 t + \varphi_0) - t/T_2} \quad . \tag{2.51}$$

This gives a representation of the magnitude $|M_+(t)|$ and the phase $\varphi(t)$ of the NMR signal

$$|M_+(t)| = |M_+(0)| \cdot e^{-t/T_2} \tag{2.52}$$

$$\varphi(t) = \omega_0 t + \varphi_0 \quad . \tag{2.53}$$

2.1.7 *Signal Detection*

The detection of the NMR signal is based on the induction of a voltage in a coil due to a change of magnetic flux Φ. In the equilibrium state of the magnetization $\vec{M}$ parallel to $\vec{B}_0$, the magnetic flux is constant. In order to detect a signal, the magnetization needs to be tilted towards the xy-plane. The precession causes the magnetic flux to change over time. If a coil is placed perpendicular to the z-axis, according to Faraday's law a voltage will be induced

$$U_{\text{ind}} = -\frac{\mathrm{d}}{\mathrm{d}t} \int_S \vec{B} \cdot \mathrm{d}\vec{S} = -\frac{\mathrm{d}\Phi}{\mathrm{d}t} \quad . \tag{2.54}$$

The surface of the coil is denoted by S. It can be shown using Stokes' theorem that

$$\Phi(t) = \int_V \mathrm{d}^3\vec{r}\, \vec{M}(\vec{r}, t) \cdot \vec{B}^-(\vec{r}) \tag{2.55}$$

with the integral over the coil surface S being replaced by an integral over the sample volume V. $\vec{B}^-$ denotes the receive field of the coil. According to the law of reciprocity, this receive field corresponds to the magnetic flux density

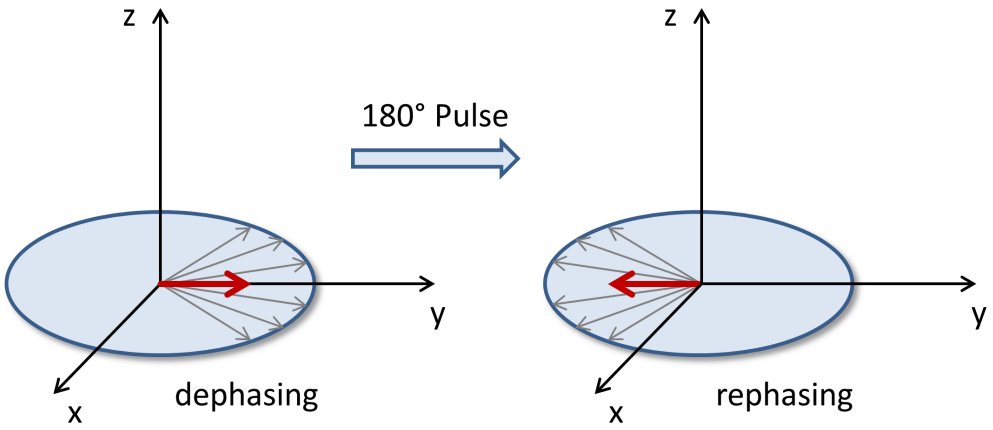

Figure 2.6: The 180° refocusing pulse inverts the phases of the individual spins, which leads to the formation of a spin echo.

created by a unit current in that coil. It follows that the signal S measured in an NMR experiment is given by

$$S(t) = S_0 \cdot \int_V \rho(\vec{r}) \mathrm{d}\vec{r} \cdot e^{-i\gamma B_0 t} \cdot e^{-t/T_2} \tag{2.56}$$

with the proportionality factor S_0 and the spin density ρ.

2.1.8 *Spin Echo*

The signal, which is measured in the coil after excitation without further manipulation, follows an exponential function with the decay constant T_2*. This is called the Free Induction Decay (FID). If the reversible component T_2' is now to be restored, a so-called Spin Echo (SE) must be generated. The magnitude at the SE follows the irreversible T_2 decay. In order to generate the SE at a particular Echo Time (TE), an additional pulse at TE/2 with a flip angle of $\alpha = 180°$ is used, which refocuses the spins. The process is depicted in Figure 2.6.

2.2 MAGNETIC RESONANCE IMAGING

If a tomographic image is to be formed from the NMR signal, the signal must be linked to its place of origin. In 2003, Lauterbur and Mansfield were awarded the Nobel Prize for the development of methods for the spatial encoding of the NMR signal using magnetic field gradients. The ability to reconstruct tomographic images allowed the immense importance of MRI for medical imaging to develop. The basics of spatial encoding of the MR signal are described in the following section.

2.2.1 *Spatial Encoding*

Spatial encoding is based on the superposition of the B_0 field with a locally variable magnetic field

$$\vec{G} = \left(\frac{\partial B_0}{\partial x}, \frac{\partial B_0}{\partial y}, \frac{\partial B_0}{\partial z}\right) \quad . \tag{2.57}$$

This gradient field leads to a spatial dependency of the Larmor frequency

$$\omega(\vec{r}) = \gamma(B_0 + \vec{r} \cdot \vec{G}) \quad . \tag{2.58}$$

This way, the location of the signal is encoded in its frequency and can be extracted by the Fourier transform. In order to reconstruct spatial information in three dimensions, three spatial encoding steps are necessary. These steps are called slice selection, frequency encoding and phase encoding.

SLICE SELECTION One slice of the imaging volume is selected by applying a gradient during the excitation pulse. This gradient is usually applied in z-direction and, accordingly, the resonance frequency is linearly dependent on z. Due to the finite bandwidth $\Delta\omega$ of the RF pulse, the range of frequencies within the pulse excite a slice with a certain thickness. Bandwidth and slice thickness are linked via the equation

$$\Delta z = \frac{\Delta\omega}{\gamma G_z} \quad . \tag{2.59}$$

This relationship is visualized in Figure 2.7. The shape of the excited slice is given by Fourier transform of the frequency distribution within the excitation pulse. In order to obtain a rectangular slice, a sinc pulse must be used. However, due to a finite pulse duration, the sinc pulse is truncated leading to an imperfect slice profile.

The usage of a slice selection gradient leads to a spin dephasing along the z-axis. To compensate for this, a rephasing gradient is commonly used. Assuming that the excitation occurs immediately at the center of pulse and gradient, half of the gradient moment needs to be reversed. Hence, a rephasing gradient is applied with the inverse direction and half the duration.

FREQUENCY ENCODING Within the excited slice, another spatial dimension can be isolated by applying a gradient in x-direction during signal readout. This so-called frequency encoding gradient results in a different precession frequency for each position along the x-axis

$$\omega(x) = \gamma(B_0 + x \cdot G_x) \quad . \tag{2.60}$$

The measured signal is now a superposition of different frequencies. The Fourier transform yields the magnitude of these individual frequencies, which is directly linked to the origin of the signal along the x-axis. The concept of frequency encoding is schematically depicted in Figure 2.8.

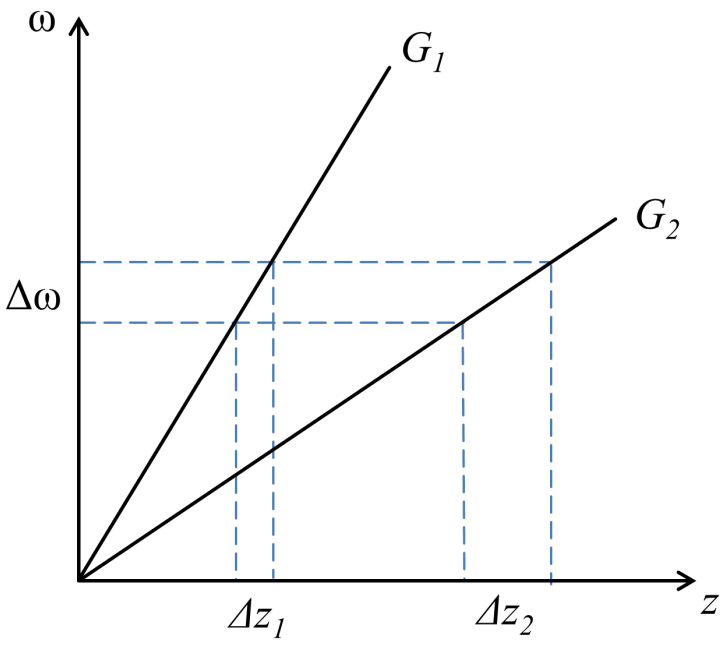

Figure 2.7: The thickness of the excited slice Δz is determined by the RF bandwidth $\Delta\omega$ and the slice selection gradient G_z. A steeper gradient corresponds to a thinner slice.

PHASE ENCODING The third spatial dimension can be encoded by an additional gradient along the y-axis between excitation and readout. This phase encoding gradient G_y changes the precession frequency along the y-axis for a certain time τ. After the gradient is switched off, all spins along this axis precess with the same frequency again. However, their phase has changed depending on the y-location. The acquired signal now consists of a set of the same frequency but different phase offsets

$$\Delta\varphi = \Delta\omega\tau = \gamma G_y \tau \quad . \tag{2.61}$$

This process is repeated N times with G_y varying between $-G_{y,\max}$ and $G_{y,\max}$. This yields a set of N linear equations, which can be solved for the magnitude at the y-position.

The spatial encoding process described so far is called 2D imaging. In case of 3D imaging, slice selection is replaced by an additional phase encoding step.

2.2.2 *k-Space*

It is often useful to view the resulting signal in Fourier space. This space is called k-space in MRI. The application of a gradient imprints a certain phase pattern onto the spins. To each phase pattern, there is an associated wave number k, which is defined as

$$\vec{k} = \frac{\gamma}{2\pi} \int_0^t \vec{G}(t')\mathrm{d}t' \quad . \tag{2.62}$$

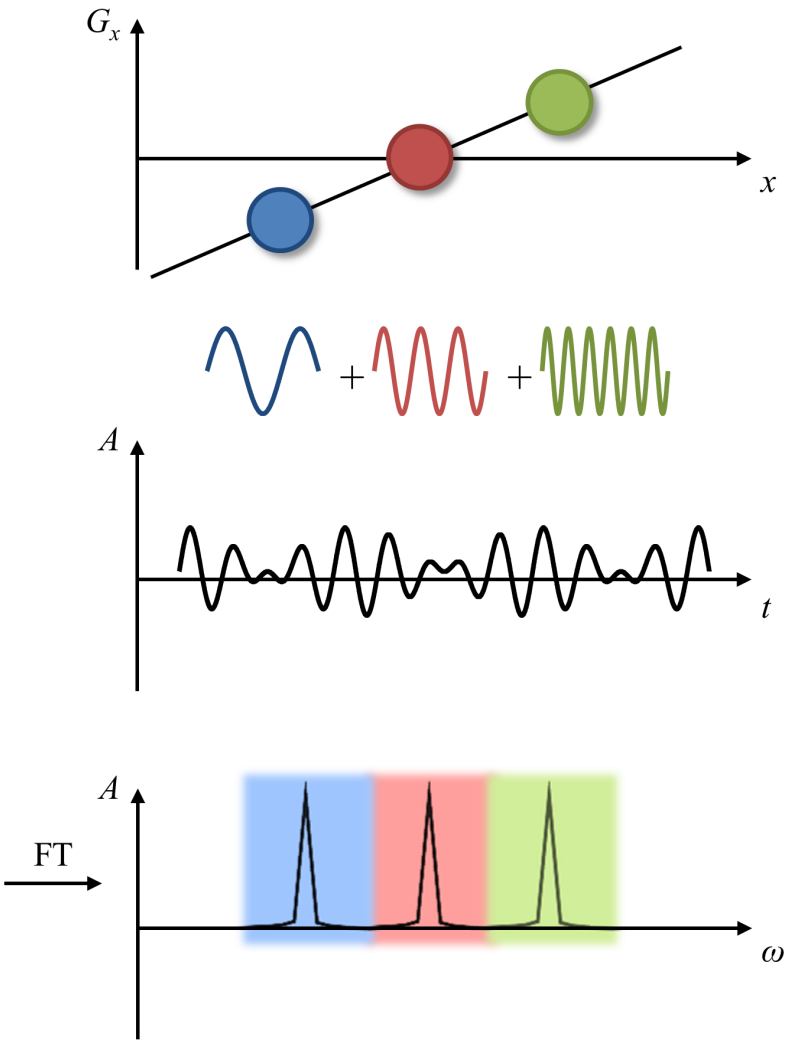

Figure 2.8: Frequency encoding: The magnetic field gradient leads to different precession frequencies along the x-axis. Correspondingly, the acquired signal is a composition of different frequencies. The amplitude A of the individual frequencies can be extracted by the Fourier transform. The origin of the signal is given by the relationship between frequency and position generated by the gradient.

Using this definition and by neglecting relaxation terms, the equation for the measured signal in Equation 2.56 can be rewritten as

$$S(\vec{k}) = S_0 \cdot \int \rho(\vec{r}) \cdot e^{-2\pi i \vec{k}\cdot\vec{r}} \mathrm{d}\vec{r} \tag{2.63}$$

$$= S_0 \cdot (\mathcal{F}\rho)(\vec{r}) \tag{2.64}$$

with the Fourier transform $\mathcal{F}$. This shows that the spatial frequencies can be sampled directly with MRI by imprinting different phase patterns with varying gradient moments. The MR image is then reconstructed by the inverse Fourier transform of the sampled k-space.

Commonly, the k-space is sampled with a Cartesian trajectory in discrete steps of Δk_x and Δk_y. For frequency encoding, the gradient G_x is switched on for the time t_x, during which N_x data points are recorded with the time interval $\Delta t_x = t_x / N_x$. In each of the N_y phase encoding steps, the gradient is increased by ΔG_y and applied for a fixed time t_y. This results in the k-space increments

$$\Delta k_x = \frac{\gamma}{2\pi} G_x \Delta t_x \tag{2.65}$$

$$\Delta k_y = \frac{\gamma}{2\pi} \Delta G_y t_y \quad . \tag{2.66}$$

The image volume is determined by the k-space increments and is called Field of View (FOV)

$$\mathrm{FOV}_x = \frac{1}{\Delta k_x} \tag{2.67}$$

$$\mathrm{FOV}_y = \frac{1}{\Delta k_y} \quad . \tag{2.68}$$

It needs to be chosen in a way it covers the whole object. Otherwise, areas outside the FOV will wrap into the image and cause artifacts. The image resolution is determined by the FOV divided by the number of pixels

$$\Delta x = \frac{\mathrm{FOV}_x}{N_x} = \frac{1}{\gamma G_x \Delta t_x N_x} \tag{2.69}$$

$$\Delta y = \frac{\mathrm{FOV}_y}{N_y} = \frac{1}{\gamma \Delta G_y t_y N_y} \quad . \tag{2.70}$$

According to the Nyquist theorem, the sampling frequency must be at least twice the highest frequency that is to be sampled. Therefore, the following sampling criteria can be derived

$$\Delta t_x \leq \frac{1}{\gamma G_x N_x \Delta x} \tag{2.71}$$

$$\Delta G_y \leq \frac{1}{\gamma t_y N_y \Delta y} \quad . \tag{2.72}$$

2.2.3 *Sequences*

The set of applied RF pulses and gradients that describe the MR measurement is called sequence. It determines the k-space trajectory and can be adjusted

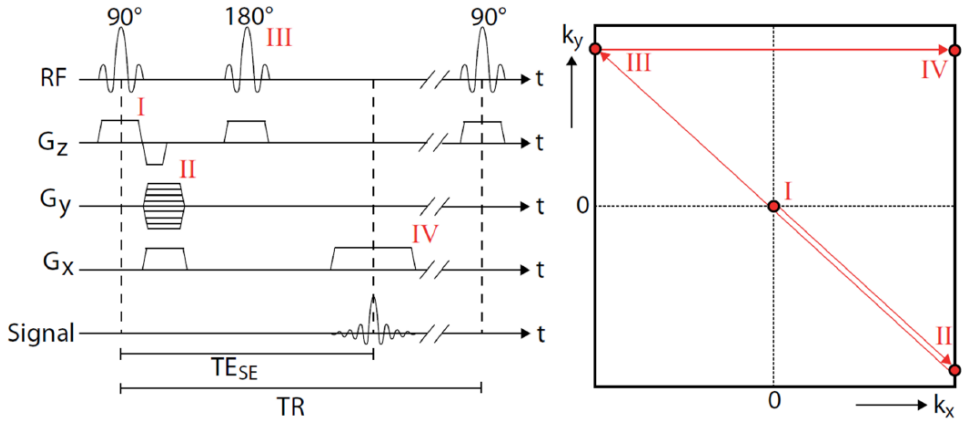

Figure 2.9: Sequence diagram of the spin echo sequence (left) and the corresponding k-space trajectory (right). The 180° refocusing pulse mirrors the k-space coordinate at the origin. It reverses the spin dephasing and leads to the formation of a spin echo at TE. Figure adapted from Mie [2011].

according to the desired image contrast. Here, two basic sequences called Spin Echo (SE) and Gradient Echo (GRE) are described. The later used Gradient Echo Sampled Spin Echo (GESSE) sequence is a combination of these two. Additionally, the Echo Planar Imaging (EPI) sequence is described since the later used Arterial Spin Labeling (ASL) utilizes an EPI readout.

SPIN ECHO SEQUENCE The spin echo sequence uses a slice-selective 90° excitation pulse, which tips the magnetization into the transverse plane. Initially, all spins are in phase. However, as described in Section 2.1.8, the spins lose their phase coherence due to different precession frequencies. The total magnetization in the transverse plane decreases with T_2*. After TE/2, a 180° refocusing pulse is applied, which reverses the individual spin phases. The phase coherence is restored except for the part that is lost due to irreversible T_2 relaxation. A spin echo is formed at TE with the signal amplitude dependent on T_2. In order to acquire the entire k-space, the sequence is repeated after the Repetition Time (TR) with the next excitation pulse. The sequence diagram of the spin echo sequence is depicted in Figure 2.9.

GRADIENT ECHO SEQUENCE The sequence diagram of the gradient echo sequence is depicted in Figure 2.10. No refocusing pulse is applied. However, another form of echo is generated by dephasing the spins in x-direction and subsequently refocusing them by a gradient with the opposite direction. Once the entire gradient moment is reversed, all spins are in phase again and a so-called gradient echo is formed. In k-space, this is depicted as a vector to the left edge during dephasing and a vector to the right edge during rephasing. As for spin echo sequences, this process is repeated several times in order to sample the whole k-space.

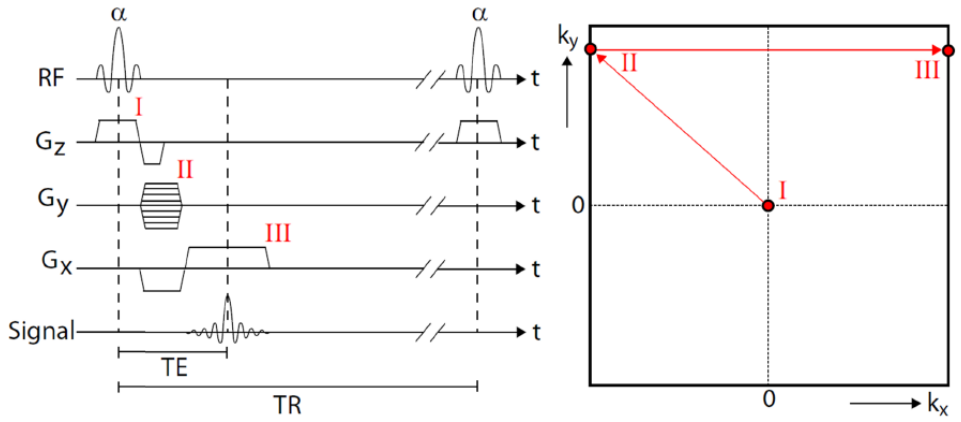

Figure 2.10: Sequence diagram of the gradient echo sequence (left) and the corresponding *k*-space trajectory (right). Figure adapted from Mie [2011].

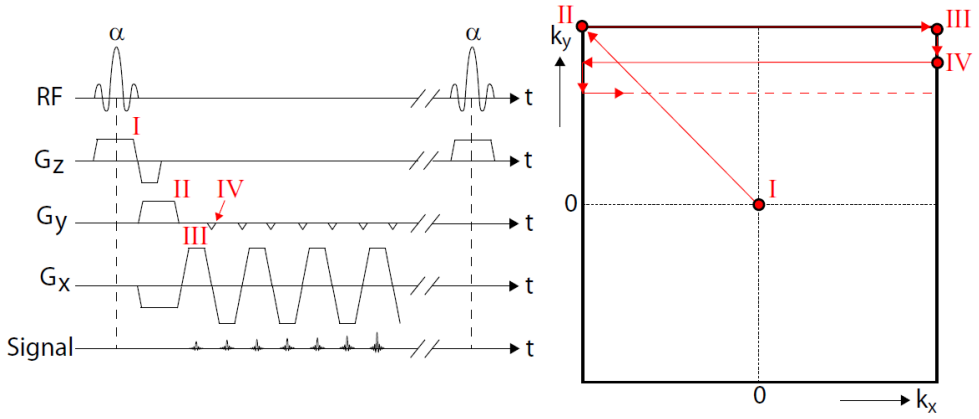

Figure 2.11: Sequence diagram of the Echo Planar Imaging sequence (left) and the corresponding *k*-space trajectory (right). Figure adapted from Mie [2011].

ECHO PLANAR IMAGING EPI is a very fast sequence that is capable of sampling the whole *k*-space within one TR. This is done by directly switching to the next phase encoding step – as soon as one frequency encoding line is completed – without further excitation pulses. The corresponding sequence diagram is shown in Figure 2.11.

2.2.4 *Image Contrast and Quality*

The contrast of an MR image highly depends on the sequence parameters. TE and TR can be adjusted in order to achieve the desired contrast. Typical contrasts are called T_1-, T_2- or Proton Density (PD)-weighted. A short TE leads to an image acquisition shortly after the excitation pulse. The signal differences among tissues with differing T_2 are small. Thus, the T_2 contrast is suppressed. With longer TE, the T_2 contrast gets more pronounced. On the other hand, a long TR leads to an almost complete recovery of *z*-magnetization

for all T_1. Only small differences among the tissues with different T_1 are visible. However, with shorter T_1 these differences in longitudinal relaxation increasingly influence the excited signal. It follows that a short TE and short TR yield a T_1-weighted contrast and long TE and long TR yield a T_2-weighted contrast. If both effects are suppressed by choosing a short TE and long TR, it results in a PD-weighted contrast.

The image quality is highly influenced by the amount of noise compared to the signal intensity. The Signal to Noise Ratio (SNR) is defined as the mean of the signal within the measured object divided by the Standard Deviation (SD) of the signal outside the object where only noise is present. It can be increased by repeating the measurement and averaging the results or by reducing the resolution. Therefore, the SNR depends on the number of acquisitions N_{acq} and the voxel size V_{voxel}

$$\text{SNR} \sim \sqrt{N_{\text{acq}}} \cdot V_{\text{voxel}} \quad . \tag{2.73}$$

In a GRE sequence, the Ernst angle α_{E} describes the flip angle that yields the highest signal for a given tissue

$$\alpha_{\text{E}} = \arccos(e^{-\frac{\text{TR}}{T_1}}) \quad . \tag{2.74}$$

However, due to the inversion pulse in spin echo sequences, a different relationship for the optimal flip angle θ has to be used:

$$\theta = 180^\circ - \alpha_{\text{E}} \quad . \tag{2.75}$$

2.2.5 *Arterial Spin Labeling*

ASL refers to an MRI-based method for perfusion imaging that does not require an exogenous contrast agent. Other methods, such as Dynamic Contrast Enhanced (DCE) imaging, are based on the injection of gadolinium to create the desired contrast. In ASL, first a control image of the Region of Interest (ROI) is acquired. Then the magnetization of the protons in a region proximal to the ROI is inverted by an RF pulse. This causes the protons within this area to be magnetically labeled. Due to the blood flow, the labeled protons of water molecules move into the ROI within a certain time called Post-Labeling Delay (PLD). Now a second image of the ROI is taken. The signal of this tagged image is subtracted from the control image and a perfusion-weighted image is obtained. A schematical visualization is shown in Figure 2.12.

2.3 BRAIN TISSUE OXYGENATION

The physiological way of energy generation within cells is by metabolizing glucose and oxygen, which releases energy and results in CO_2 and water as byproducts. Oxygen and nutrients are transported to the tissue within the blood in arteries and deoxygenated blood as well as metabolic waste products are removed via the veins. In order for substances to be exchanged between

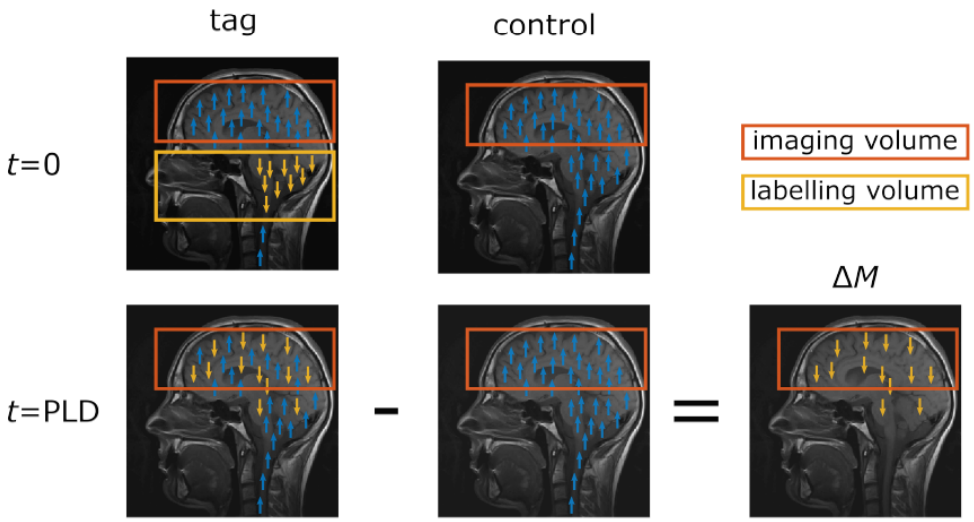

Figure 2.12: In Arterial Spin Labeling (ASL), a magnetically tagged image and a control image without magnetical preparation are taken. The perfusion-weighted image is obtained by subtracting the tagged and control image. Figure adapted from Hubertus [2019]

blood and tissue, arteries and veins are connected by a fine network of vessels, the so-called capillary bed. A schematic representation of a blood vessel network is shown in Figure 2.13.

The brain has a high and constant demand for energy. Under normal circumstances, the brain metabolism is kept in a narrow range by a vascular process called autoregulation.

2.3.1 *Properties of Blood*

Blood consists of a liquid called plasma and blood cells, namely erythrocytes, leukocytes and thrombocytes. Their share of the total volume of the blood is

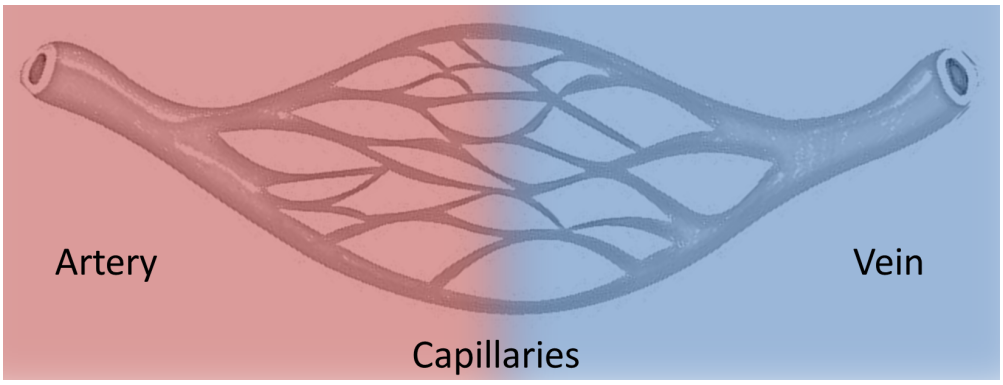

Figure 2.13: Blood vessel network: From artery via capillaries to vein. Oxygen is extracted within the capillary bed, which increases the ratio of deoxyhemoglobin.

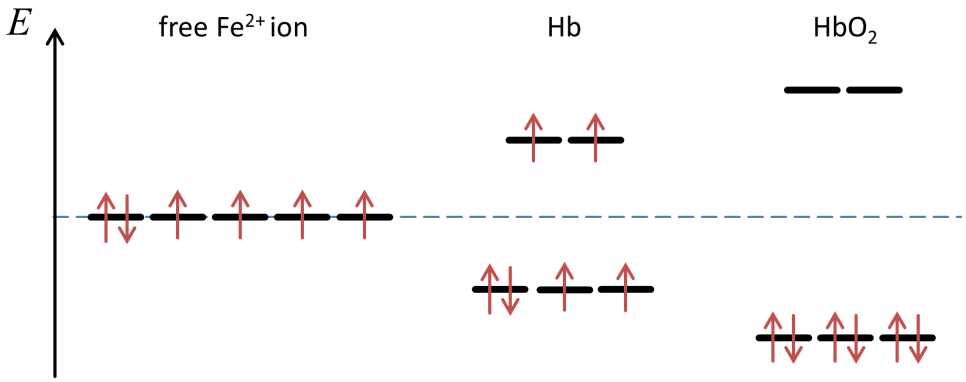

Figure 2.14: Energy states of the 3d orbitals of the iron ion. In the free ion, the energies are degenerated. In the form of deoxygenated hemoglobin, the energies are split into two levels. However, the preferred electron configuration stays the same. The unpaired electrons yield a permanent magnetic dipole and, hence, paramagnetic properties. In the oxyhemoglobin configuration, the larger energy gap leads to a pairing of all electrons. Therefore, the diamagnetic properties are now dominant.

called Hematocrit (Hct). For men, it is in a range of 41-50% and for women 37-46%. Leukocytes have an important function for the immune system and thrombocytes help with blood clotting. The erythrocytes form by far the largest group of cellular blood components and are responsible for the transport of oxygen. They contain Hemoglobin (Hb), which itself consists of four heme groups with one Fe^{2+} ion each. One O_2 molecule can bind to one Fe^{2+} ion. The oxygen bound hemoglobin is called oxyhemoglobin (HbO_2). In the absence of oxygen it is referred to as deoxyhemoglobin (Hb). The change of energy levels associated with the binding of oxygen is depicted in Figure 2.14. In the unbound state, the Fe^{2+} ion has six electrons in the degenerated 3d orbitals. In the form of Hb, the energy states of iron split into a lower and upper level. The electrons are still unpaired and, thus, deoxyhemoglobin is paramagnetic. However, in the form of HbO_2, the energy gap gets large enough for all the electrons to pair on the lower energy level. This results in the diamagnetic properties of oxyhemoglobin. The difference in magnetic susceptibility between Hb and HbO_2 forms the basis for all MRI-based measurements of the oxygenation level. The influence of the oxygenation level on the MRI signal is called Blood Oxygen Level Dependent (BOLD) effect.

2.3.2 *Blood Oxygenation*

The oxygenation level of the blood Y is defined as the ratio between the oxygenated hemoglobin concentration and the total hemoglobin concentration

$$Y = \frac{[HbO_2]}{[HbO_2] + [Hb]} \quad . \tag{2.76}$$

As a measure of relative oxygen extraction in tissue, the OEF is defined as

$$\mathrm{OEF} = \frac{Y_{\mathrm{arterial}} - Y_{\mathrm{venous}}}{Y_{\mathrm{arterial}}} \quad . \tag{2.77}$$

It is commonly assumed that the arterial oxygenation saturation is close to 1. Hence, the OEF can be written as

$$\mathrm{OEF} = 1 - Y_{\mathrm{venous}} \quad . \tag{2.78}$$

Under normal conditions, the OEF is homogeneous and about 40% in the entire brain at a resting state [Gusnard and Raichle, 2001]. As a combination of the relative oxygen consumption and the blood delivery, the absolute consumption called CMRO2 is

$$\mathrm{CMRO2} \sim \mathrm{OEF} \cdot \mathrm{CBF} \quad . \tag{2.79}$$

Under normal conditions, the CMRO2 is about $120 - 180\,\mu\mathrm{mol}/100\,\mathrm{g}/\mathrm{min}$ in Gray Matter (GM) and $40 - 80\,\mu\mathrm{mol}/100\,\mathrm{g}/\mathrm{min}$ in White Matter (WM) [Leenders et al., 1990; Ito et al., 2004]. CBF is typically about $20\,\mathrm{ml}/100\,\mathrm{g}$ of brain tissue/min in WM and $60\,\mathrm{ml}/100\,\mathrm{g}$ of brain tissue/min in GM [Günther et al., 2005]. This sums up to about 750 ml/min through a healthy adult's brain.

2.3.3 *Blood Oxygenation Level Dependent Effect*

The BOLD contrast describes the effect of the blood deoxyhemoglobin level on the MR signal. It arises from the difference in magnetic susceptibility between deoxyhemoglobin and oxyhemoglobin. Oxyhemoglobin is diamagnetic and since its susceptibility is very close to tissue, its impact on the MR signal is negligible. Deoxyhemoglobin, on the other hand, is paramagnetic and, therefore, affects the MR signal due to the substantial susceptibility difference to the surrounding tissue. The signal is not only affected within the blood vessel itself but also a region of up to 5 times the radius around the vessel is influenced by magnetic field perturbations [Christen et al., 2013]. A visualization of the magnetic field around a paramagnetic cylinder is shown in Figure 2.15.

The susceptibility difference of blood vessel and surrounding tissue can be expressed in terms of Hct, OEF and the susceptibility difference between completely deoxygenated and completely oxygenated red blood cells $\Delta\chi_{\mathrm{do}}$

$$\Delta\chi = \mathrm{Hct} \cdot \mathrm{OEF} \cdot \Delta\chi_{\mathrm{do}} \quad . \tag{2.80}$$

$\Delta\chi_{\mathrm{do}}$ is usually assumed to be 2.26 ppm [Weisskoff and Kiihne, 1992]. The susceptibility difference $\Delta\chi$ is linked to a frequency shift and therefore contributes to the MR signal dephasing, which contributes to the transverse relaxation visible in $T_2{}^*$ weighted images. The MR signal can be described as

$$S(t) = S_0 \cdot \exp\left(-\Gamma(t)\right) \tag{2.81}$$

with $\Gamma(t)$ being the signal attenuation function. Commonly, the simple relationship of $\Gamma(t) = R_2{}^* \cdot t$ is used. However, in order to quantify the effect, a more accurate approach has to be introduced. This is further described in Section 3.5.

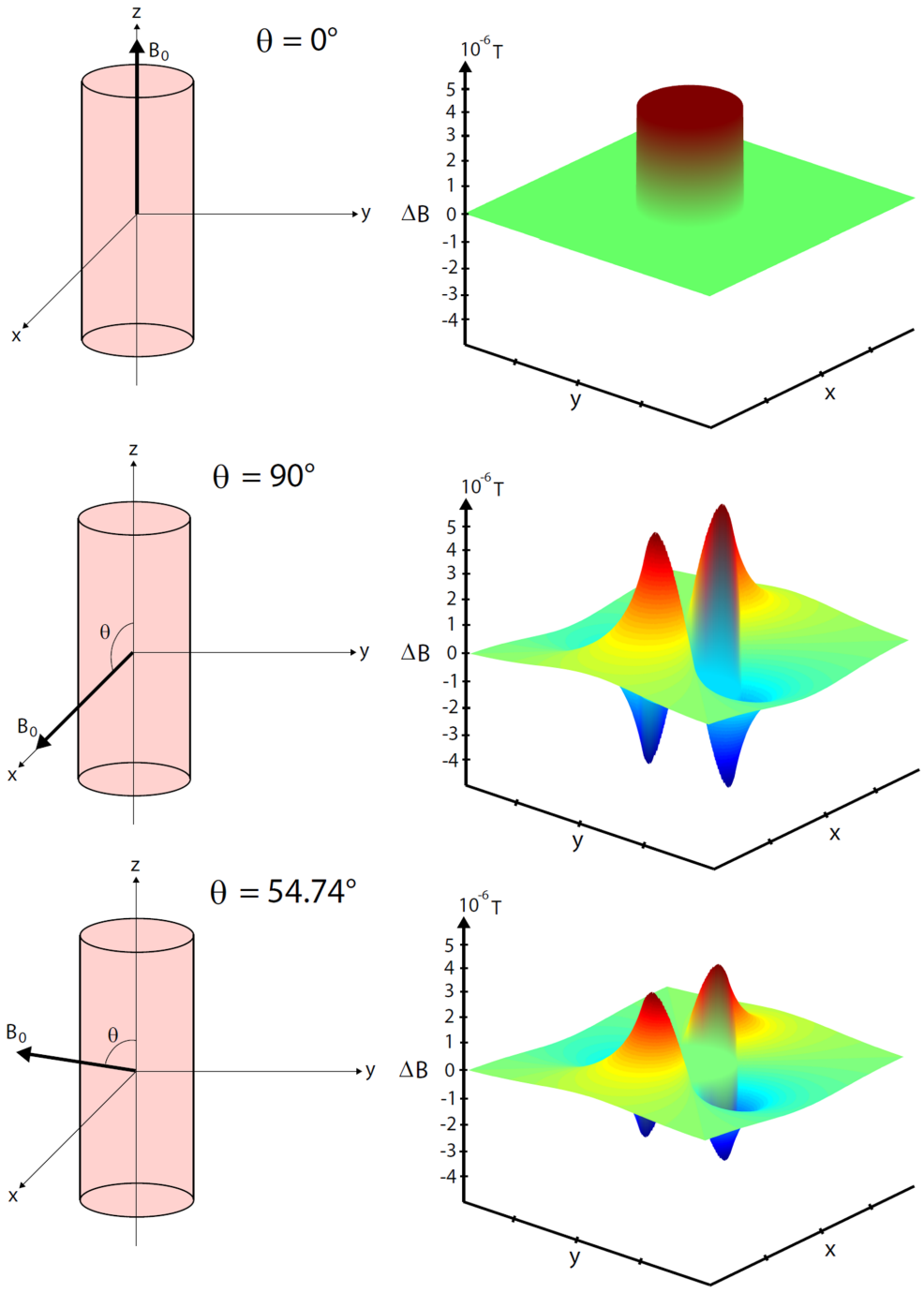

Figure 2.15: A paramagnetic cylinder generates magnetic field perturbances in the surrounding tissue. The magnetic field is dependent on the orientation of the cylinder with respect to the external magnetic field. On top, the cylinder is parallel to B_0. In the middle it is perpendicular. At the bottom, the perturbance inside the cylinder vanishes at the magic angle. Figure adapted from Mie [2011].

2.3.4 *Cigarette Smoking*

Smoking remains a leading cause of death worldwide, resulting in 8 million preventable deaths globally in 2017 [Stanaway et al., 2018]. Use of tobacco products has been linked to an increased risk of vascular stenosis, heart attack, chronic obstructive pulmonary disease, and various cancers. This greatly impacts quality of life and places an additional strain on health care systems that are already struggling to keep pace with an aging population in growing need of treatment for chronic diseases [Thun et al., 1995]. Current smoking cessation treatments have shown only moderate success and relapse rates following initial treatment success remain high [Baker et al., 2016]. As such, research investigating the neural mechanisms underlying the development and maintenance of tobacco use disorder, as well as factors that predispose individuals to relapse, is crucial to improving treatment and overall health outcomes in the future.

For many years now, there has been overwhelming evidence that nicotine constitutes the main addictive component of cigarettes [Centers for Disease Control & Prevention, 2010]. Despite this fact, there is no consensus concerning the acute and chronic effects of smoking-related nicotine administration on brain metabolism. ^{15}O PET studies have found the global CBF to decrease [Yamamoto et al., 2003], increase [Skinhoj et al., 1973; Vafaee et al., 2015] and remain unchanged [Shinohara et al., 2006] after smoking. In addition to these global, i. e. whole brain, changes in brain metabolism, focal regional changes in CBF have been found for the visual cortex, thalamus and cerebellum in several studies [Domino et al., 2000, 2004; Rose et al., 2003; Zubieta et al., 2005]; however, a general agreement has not been reached here, either.

2.3.5 *Brain Tumors*

The most common type of brain tumor is the highly aggressive glioblastoma (WHO grade IV). They have a high mortality rate with the median survival time of only about 12 to 15 months [Wen and Kesari, 2008]. The treatment usually consists of a surgical resection and subsequent radio- and chemotherapy. For the optimal treatment planning, image acquisition with MRI is essential. In morphological MRI acquisitions, glioblastoma typically show as a growing tumor region displacing the normal tissue and a surrounding edema. Using a contrast agent, a hyperintense area around the tumor shows the accumulation of contrast agent indicating a broken blood-brain-barrier.

Tumors can create dedicated blood supply by an increased vascularization (angiogenesis) and develop the ability to survive with less oxygen due to the Warburg Effect. According to the Warburg Effect, the glucose metabolism is changed in some cancer cells. The cells follow a different metabolic path that does not use oxygen despite oxygen being present. Normal cells only use this anaerobic glycolysis under a lack of oxygen. This type of energy pathway is inefficient leading to an increased glucose consumption. Therefore, despite

the increased energy and glucose consumption, the OEF in tumor tissue can be decreased.

3 MATERIALS AND METHODS

In this chapter, the materials and methods used in this thesis are presented. The hardware and sequences used for data acquisition and the methods used for data processing and data evaluation are described. Furthermore, the design of the in vivo studies is covered including healthy volunteers, smokers and tumor patients.

3.1 MR SCANNER

All data of the volunteers and patients measurements were acquired on a clinical 3 T MAGNETOM Trio scanner (Siemens Healthcare GmbH, Erlangen, Germany) at the University Hospital Mannheim (Figure 3.1). The smoker study was performed at an identical scanner at the Zentralinstitut für Seelische Gesundheit (ZI) in Mannheim. The scanner uses superconducting coils cooled by liquid helium for creating the static main magnetic field. The homogeneity of the main magnetic field is improved by active shimming using the shim coils and passive shimming using ferromagnetic materials placed at specific locations along the bore. The scanner has a length of 213 cm and a bore diameter of 60 cm. The gradient system allows a maximum gradient amplitude of 40 mT/m and a maximum slew rate of 200 mT/m/ms. For all scans a 32-channel head-coil was used (Siemens Healthcare GmbH, Erlangen, Germany).

3.2 SEQUENCES

Several sequences are used for the reconstruction of different parameters and different approaches. The GESSE sequence is used for the standard parameter fit (LS), the regularized fit and the ANN approach of the qBOLD reconstruction, which yields S_0, R_2, OEF and DBV. The mGRE and mSE sequences are used for an alternative and independent approach MP and are acquired as a comparison to the GESSE-based approaches. The ASL sequence is used for the estimation of the CBF.

3.2.1 *Gradient Echo Sampled Spin Echo (GESSE)*

The sequence consists of a spin echo as described for the standard spin echo sequence in Section 2.2.3. In addition to the readout at the TE, the signal is sampled with multiple gradient echoes before and after the spin echo. This way, several images are acquired with varying T_2* weighting and the effects of T_2 and T_2* can be separated. The sequence diagram of the GESSE sequence is depicted in Figure 3.2.

Figure 3.1: 3 T MAGNETOM Trio scanner (Siemens Healthcare GmbH, Erlangen, Germany) at University Hospital Mannheim.

For a clinically acceptable acquisition time of 10 min and a sufficient volume coverage, the sequence parameters were chosen to be: TR = 2770 ms, TE_1 = 29 ms, ΔTE = 2 ms, 32 echoes, spin echo at #10, resolution = 2 x 2 x 2 mm^3 with 33% slice gap, 25 slices, 3 averages, matrix size = 128 x 96, flip angle = 90°, acquisition time = 10:00 min.

3.2.2 *multi Gradient Echo (mGRE)*

After the initial excitation, multiple gradient echoes with varying TE are performed within one TR. This way, the T_2* decay can be sampled. The sequence parameters were: TR = 2650 ms, TE_1 = 4.5 ms, ΔTE = 5.5 ms, 12 echoes, resolution = 1.7 x 1.7 x 1.5 mm^3 with 20% slice gap, 66 slices, matrix size = 128 x 96, flip angle = 85°, acquisition time = 5:18 min.

3.2.3 *multi Spin Echo (mSE)*

In this sequence, a standard SE is performed but with several TEs in order to sample the T_2 decay. The sequence parameters were: TR = 2650 ms, TE_1 = 13.1 ms, ΔTE = 13.1 ms, 12 echoes, resolution = 2 x 2 x 2 mm^3 with 20% slice gap, 45 slices, matrix size = 128 x 96, flip angle = 90°, acquisition time = 7:19 min.

3.2.4 *pseudo-Continuous Arterial Spin Labeling (pCASL)*

Different kinds of ASL sequences differ in their type of labeling. Continuous ASL uses a continuous RF pulse, which – together with a magnetic field gradient – leads to a flow-driven adiabatic inversion. In contrast, pulsed ASL uses

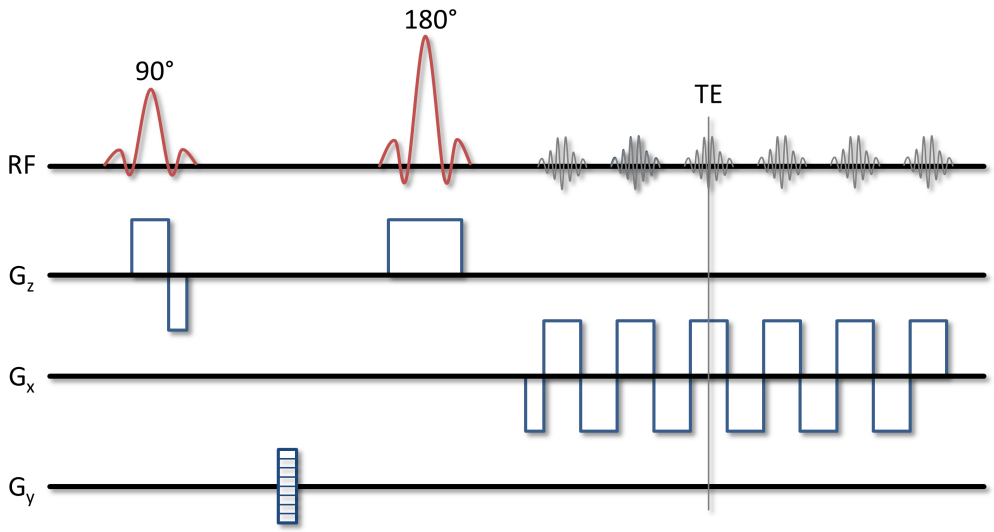

Figure 3.2: Sequence diagram of Gradient Echo Sampled Spin Echo (GESSE). At t = TE, a spin echo is generated. Around the spin echo, several gradient echos are used to sample the signal evolution. RF pulses are depicted in red, gradients in blue.

a short RF pulse for inversion, which leads to higher labeling efficiency but also to greater variation in the arrival time of the labeled blood. The pCASL sequence used here combines both methods by applying several shorter RF pulses within one labeling slab.

The sequence parameters were: TR = 5000 ms, TE = 16 ms, resolution = 3 x 3 x 3 mm^3 with 20% slice gap, 28 slices, matrix size = 80 x 80, flip angle = 90°, 48 averages, PLD = 1500 ms, Labeling Duration (LD) = 1500 ms, acquisition time = 8:05 min and the labeling plane was placed perpendicular to the internal carotid artery roughly 80 mm below the anterior- and posterior-commissure line [Alsop et al., 2015].

3.2.5 *Magnetization Prepared Rapid Gradient Echo (MPRAGE)*

The sequence parameters were: TR = 2300 ms, TE = 3 ms, TI = 900 ms, flip angle α = 9°, resolution = 1 x 1 x 1 mm^3, 192 slices, matrix size = 256 x 256, acquisition time = 5:20 min.

3.3 IMAGE PROCESSING

The acquired MR images in DICOM format were imported into MATLAB R2017a (MathWorks, Natick, MA, USA). For further reconstruction and comparability, the images were segmented into specific brain regions and registered to one another. These steps are described in detail in the following.

SEGMENTATION The MPRAGE data sets were meant to serve as a morphological reference for the other sequences. Depending on the type of study,

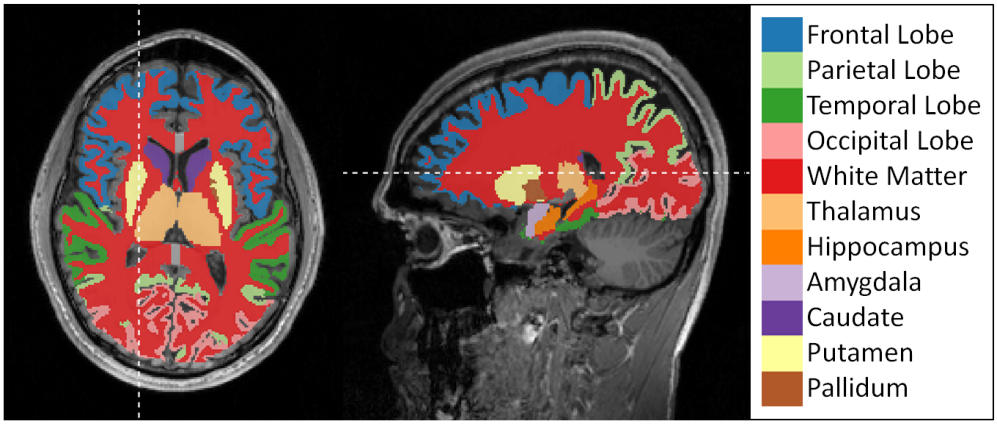

Figure 3.3: Representative transversal (left) and sagittal (right) slice of the cortical and subcortical segmentation based on the T_1 weighted image underneath. The ROIs are color-coded. The dashed lines indicate the position with respect to the other orientation.

the data were either segmented into GM and WM using SPM12 (Wellcome Trust Centre for Neuroimaging, London, UK) or segmented in more detail into subcortical regions using Freesurfer [Fischl, 2012]. For the subcortical segmentation, the data were first registered to the MNI305 [Evans et al., 1993] standard brain as a reference and then segmented into cortical gray matter, frontal lobe, parietal lobe, temporal lobe, occipital lobe, white matter, thalamus, hippocampus, amygdala, caudate, putamen and pallidum as depicted in Figure 3.3. The cortical gray matter region was created by combining frontal lobe, parietal lobe, temporal lobe and occipital lobe.

REGISTRATION The images from all other sequences were registered to the segmented MPRAGE data, which makes the segmented brain regions available for all data sets. The registration was performed using SPM12 (Wellcome Trust Centre for Neuroimaging, London, UK).

MASKING A brain mask was applied to the image data in order to exclude Cerebrospinal Fluid (CSF) and the skull from further analysis.

3.4 PERFUSION

CBF in ml/100 g brain tissue/min was estimated from the pCASL data according to the white paper from Alsop et al. [2015] as

$$\mathrm{CBF} = \frac{6000 \cdot \lambda \cdot (M_c - M_l) \cdot \exp\left(\mathrm{PLD}/T_{1,\mathrm{blood}}\right)}{2\alpha \cdot T_{1,\mathrm{blood}} \cdot M_0 \cdot \left(1 - \exp\left(-\mathrm{LD}/T_{1,\mathrm{blood}}\right)\right)} \tag{3.1}$$

with the blood-brain partition coefficient $\lambda = 0.9\,\mathrm{ml/g}$ [Herscovitch and Raichle, 1985], the control image M_c, label image M_l, proton density weighted image M_0, the longitudinal relaxation time of arterial blood $T_{1,\mathrm{blood}} = 1650\,\mathrm{ms}$ at 3 T [Lu et al., 2004] and the labeling efficiency $\alpha = 0.86$ [Aslan et al., 2011].

3.5 QUANTITATIVE BLOOD OXYGEN LEVEL DEPENDENT METHOD

In 1994, a theoretical model was proposed by Yablonskiy and Haacke [1994] to describe the BOLD effect quantitatively. It approximates blood vessels in brain parenchyma as infinitely long, randomly distributed paramagnetic cylinders. The induced signal loss is assumed to be much faster than the signal loss due to diffusive effects, which is termed static dephasing regime. This is valid for all vessels except for capillaries, where a diffusion correction has to be introduced. Since the deviation is expected to be small for field strengths of 3 T and above [He and Yablonskiy, 2007], diffusion effects are neglected in this work. Furthermore, the model assumes a small DBV, so that the signal fraction from the intravascular region can be neglected.

The signal decay can be described by the following equation:

$$S(t) = S_0 \cdot \exp\left(-\mathrm{DBV} \cdot f(\delta\omega \cdot t) - R_2 \cdot t\right) \tag{3.2}$$

where f is a characteristic function that is specific for the vessel geometry. It depends on the frequency shift

$$\delta\omega = \frac{1}{3} \cdot \gamma \cdot B_0 \cdot [\mathrm{Hct} \cdot \Delta\chi_0 \cdot (1 - Y)] \quad . \tag{3.3}$$

The signal decay can be approximated in two separate regimes. The long term regime is assumed for $|\delta\omega \cdot t| \geq 1.5$. Here, the signal follows the linear exponential function

$$S(t) = S_0 \cdot \exp(-\mathrm{DBV} \cdot (\delta\omega \cdot t - 1) - R_2 \cdot t) \quad . \tag{3.4}$$

The short term regime is assumed for $|\delta\omega \cdot t| < 1.5$ [Yablonskiy, 1998]. Here, the signal follows the quadratic exponential function

$$S(t) = S_0 \cdot \exp(-0.3 \cdot \mathrm{DBV} \cdot (\delta\omega \cdot t)^2 - R_2 \cdot t) \quad . \tag{3.5}$$

The different behavior in the two regimes allows for the separation of the qBOLD parameters if both regimes are sampled. For this reason, the GESSE sequence was developed since it enhances the possible sampling range for the short term regime in contrast to a conventional sampling of the FID in a mGRE sequence [Yablonskiy and Haacke, 1997]. The signal is measured around a spin echo, which suppresses static macroscopic inhomogeneities. Additionally, microscopic R_2 effects can be separated by using the rephasing and dephasing part of the signal. For the signal around a spin echo, Equation 3.2 is modified to

$$S(t) = S_{\mathrm{SE}} \cdot \exp\left(-\mathrm{DBV} \cdot f(\delta\omega \cdot \tau) - R_2 \cdot \tau\right) \tag{3.6}$$

with $\tau = t - t_{\mathrm{SE}}$. The characteristic function is described by the following generalized hypergeometric function [Sukstanskii and Yablonskiy, 2001]

$$f(\delta\omega \cdot t) = {}_1F_2\left(\left\{-\frac{1}{2}\right\}; \left\{\frac{3}{4}, \frac{5}{4}\right\}; -\frac{9}{16}(\delta\omega \cdot t)^2\right) - 1 \quad . \tag{3.7}$$

The dependency of the qBOLD model on the parameters R_2, OEF and DBV is visualized in Figure 3.4.

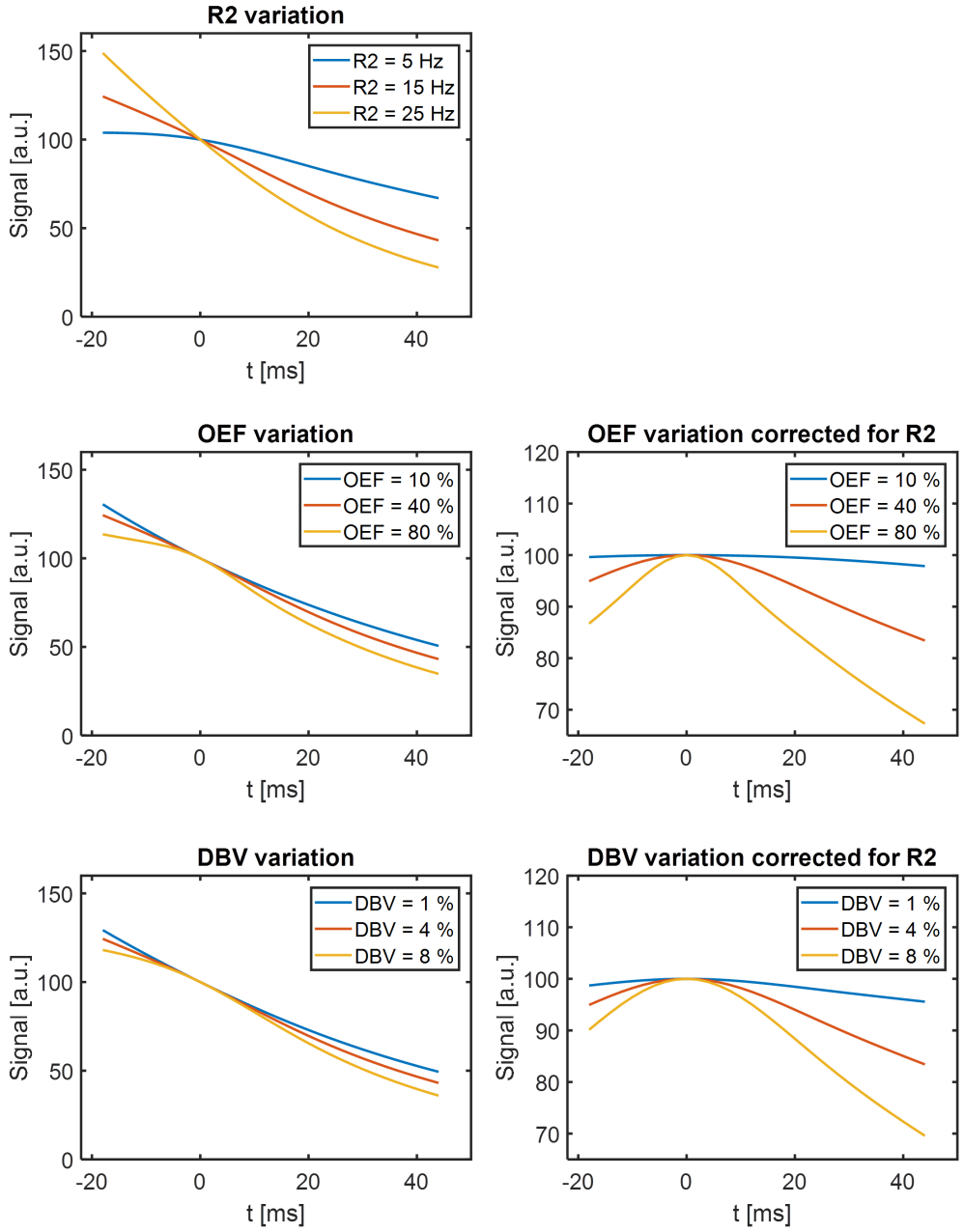

Figure 3.4: Dependency of the qBOLD model on the parameters R_2, OEF and DBV (top to bottom). The other parameters are kept constant, respectively, at $R_2 = 12\,\text{Hz}$, OEF $= 40\%$ and DBV $= 4\%$. On the right hand side, the signal was corrected for R_2 to make the influence of OEF and DBV more prominent.

3.6 STANDARD QBOLD RECONSTRUCTION METHODS

3.6.1 *Least Squares*

In the LS approach, the qBOLD model (e. g. Equation 3.6) is fitted to the GESSE data using a standard LS fit.

3.6.2 *Multiparameter*

In the MP approach, the information about the reversible and irreversible signal decay is acquired independently using two separate sequences. For this, R_2^* and R_2 values including a noise offset N_0 were fitted to the mGRE and mSE magnitude data respectively according to

$$S(\mathrm{TE}) = S_0 \cdot e^{-R \cdot \mathrm{TE}} + N_0 \quad . \tag{3.8}$$

CBF was estimated as described in Section 3.4 and DBV in ml/100 g given by [An and Lin, 2002b; Ciris et al., 2014]

$$\mathrm{DBV} = 0.77 \cdot 2.1 \cdot \mathrm{CBF}^{0.32} \quad . \tag{3.9}$$

OEF can than be estimated using

$$\mathrm{OEF} = \frac{3}{4\pi\gamma B_0} \cdot \frac{R_2{}^* - R_2}{\mathrm{DBV}} \cdot \frac{1}{\Delta\chi_{\mathrm{do}} \cdot \mathrm{Hct}} \tag{3.10}$$

and CMRO2 using

$$\mathrm{CMRO2} = \mathrm{CBF} \cdot \mathrm{OEF} \cdot [\mathrm{H}]_\mathrm{a} \tag{3.11}$$

with $[\mathrm{H}]_\mathrm{a} = 7.377\,\mu\mathrm{mol/ml}$ [Cho et al., 2018], assuming an arterial oxygen saturation of 98% and Hct = 0.357. The multiparameter workflow is depicted in Figure 3.5.

3.7 NOVEL QBOLD RECONSTRUCTION METHODS

In this section, two methods are described that have the goal to achieve a more robust parameter reconstruction compared to the standard techniques. First, the regularization approach is covered, in which the LS fit is extended by prior information. Second, the ANN approach is described, in which an ANN is trained on simulated qBOLD data.

3.7.1 *Regularization*

Regularization generally describes the process of including additional information to an optimization problem. Additional terms are added to the minimization cost function to solve ill-posed problems or avoid overfitting. Overfitting, for example, overstates noise in the data at the expense of the desired

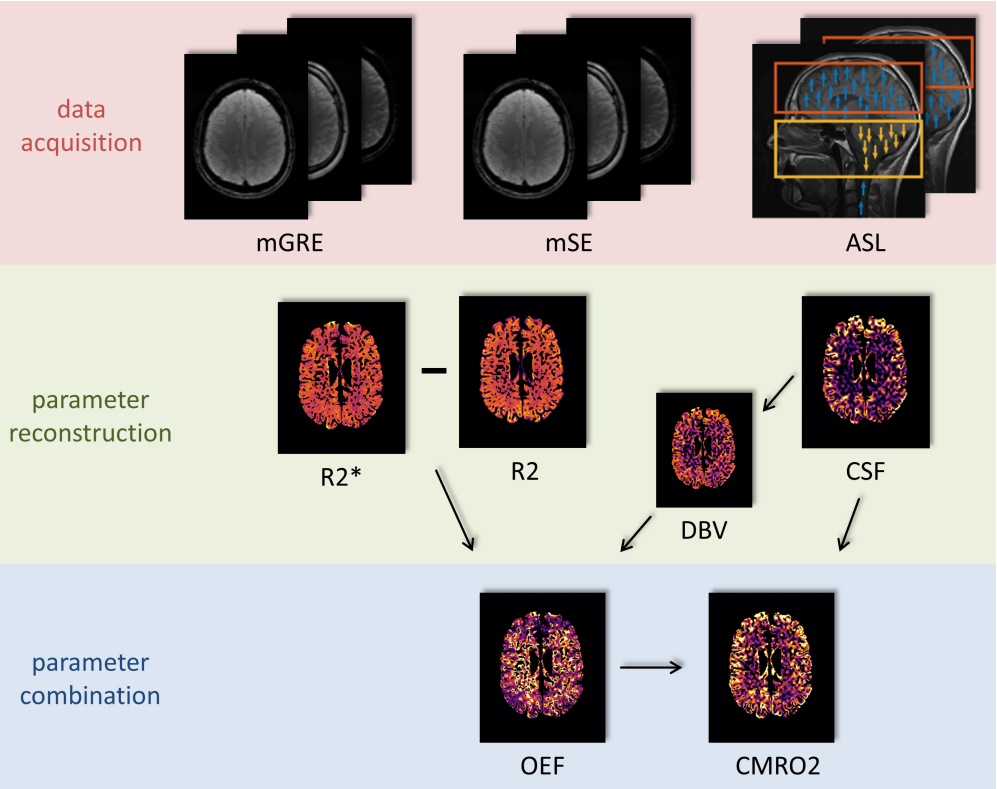

Figure 3.5: Workflow of the CBF, OEF and $CMRO_2$ reconstruction from multiparameter data. In the data acquisition step, the three sequences mGRE, mSE and ASL are measured. The relaxation parameters R_2 and R_2* are fitted as well as the physiological parameters DBV and CSF reconstructed. In the last step, the parameters are combined to the final OEF and $CMRO_2$ maps.

characteristics. In particular, regularization introduces a penalty term in addition to the least-squares term, which usually adjusts the complexity of the model to the data and yields more meaningful results. Here, the penalty term is used to incorporate prior information of the unknown parameters and thereby constrain the fit to converge to values closer to the priors by penalizing unrealistic deviations. The following cost function is defined

$$\begin{aligned}\underset{S_0,R_2,\mathrm{OEF},\mathrm{DBV}}{\arg\min} \Bigg\{ &\sum_{n=1}^{N} \Big[\ln y_n - \ln(S_n(t-\mathrm{TE}))\Big]^2 \\ &+ w_1(\mathrm{OEF}-\mathrm{OEF}_{\mathrm{prior}})^2 + w_2(\mathrm{DBV}-\mathrm{DBV}_{\mathrm{prior}})^2 \Bigg\}\end{aligned} \tag{3.12}$$

with the acquired data points y_n and the qBOLD signal function S_n. The cost function penalizes deviations from a prior DBV and OEF value, respectively. $\mathrm{OEF}_{\mathrm{prior}}$ and $\mathrm{DBV}_{\mathrm{prior}}$ were set to 40% and 2%, respectively. The weighting factors w_1 and w_2 are chosen to be proportional to the noise level of the signal. This was estimated by the Sum of Squares Error (SSE) of a voxel-wise LS fit. Furthermore, the factors were inversely proportional to the respective prior to account for the different magnitudes of the parameters. In order to adjust the overall weighting of the regularization compared to the data term, a combined weighting factor was introduced and optimized to yield a good trade-off between prior influence and data-fidelity:

$$w_1 = w \cdot \frac{S_{\mathrm{SE}}}{\mathrm{OEF}_{\mathrm{prior}}} \tag{3.13}$$

$$w_2 = w \cdot \frac{S_{\mathrm{SE}}}{\mathrm{DBV}_{\mathrm{prior}}} \tag{3.14}$$

with w being a globally adjustable weighting factor to control the influence of the regularization. The workflow of the regularization approach is depicted in Figure 3.6.

SIMULATION STUDY In order to analyze the accuracy and precision of the individual methods, simulated data was used, for which the ground truth is known. As anatomical map, the Zubal head phantom [Zubal et al., 1994] was used as shown in Figure 3.7. This is a 3D data set that is meant to represent the anatomical structure of the human brain. The parameters were set to: $S_0 = 500$, $R_2 = 11.5\,\mathrm{Hz}$ in GM and $13\,\mathrm{Hz}$ in WM, DBV = 4% in GM and 2% in WM, and OEF = 40% in both GM and WM.

These ground truth values were used together with the qBOLD model given in Equation 3.6 to simulate the GESSE signal for all 32 echoes. Gaussian noise was added to the magnitude according to an SNR of 100.

On this data, the reconstruction method was tested and accuracy and precision were analyzed by calculating the relative deviation from the ground truth and the standard deviation, respectively. The global weighting factor w is varied between [0.02 .. 500] to examine the influence of the regularization

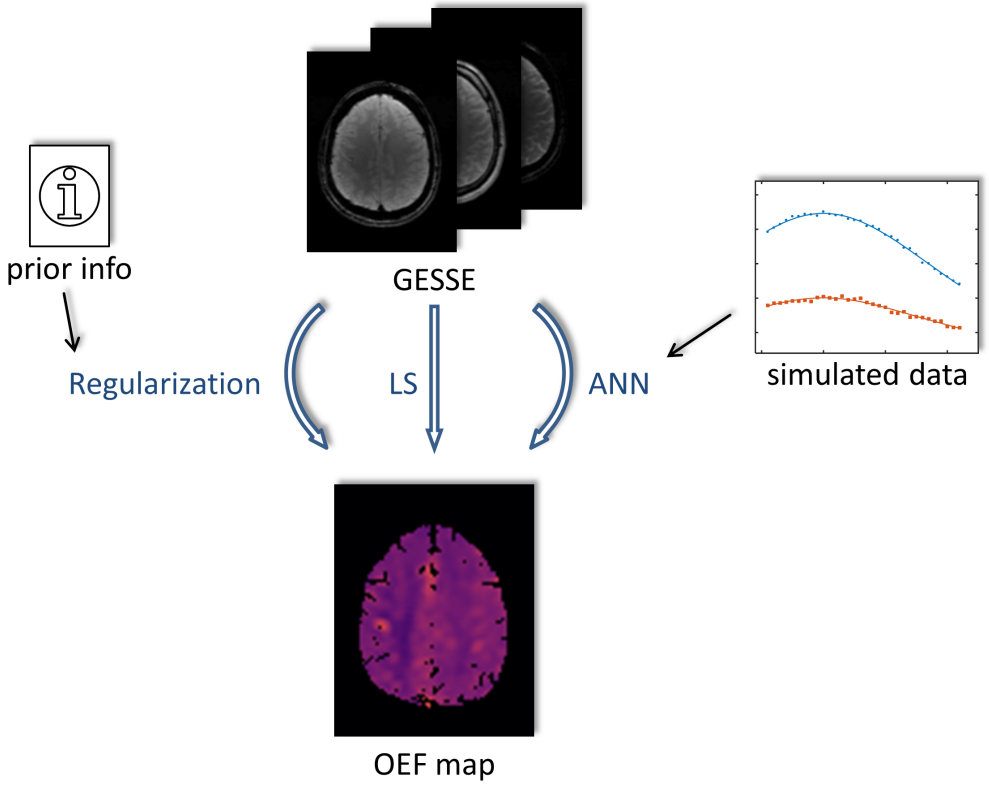

Figure 3.6: Workflow of the qBOLD parameter reconstruction from GESSE data using the LS fit, the regularization and the ANN approach. For the regularization method, prior information of the parameters is added to the fit by a regularization term. For the ANN method, qBOLD data has to be simulated corresponding to a physiological parameter range, on which the ANN is trained.

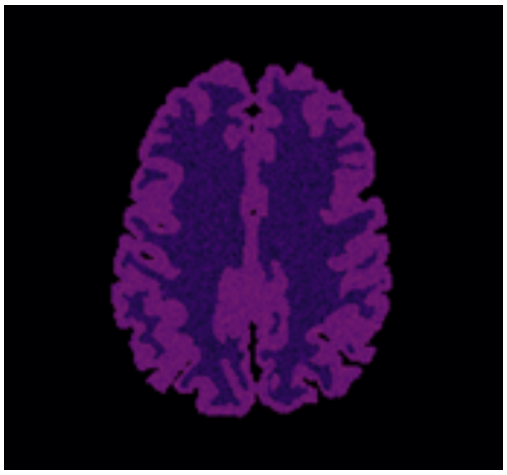

Figure 3.7: One exemplary slice of the head phantom that is used to simulate the brain data [Zubal et al., 1994]. Different parameter sets were assigned to the regions GM and WM. Here, GM is shown in brighter and WM in darker colors.

on the fitting parameters. The aim is to identify the best trade-off between data fidelity with respect to the originally measured data and the prior information. Higher influence of the data yields heterogeneous parameter maps dominated by the measurement noise. Whereas a higher influence of the prior yields (overly) smoothed parameter maps and a poor data fidelity.

In order to find the weighting factor with the best trade-off between suppressed noise and introduced bias, an L-curve analysis is performed [Hansen and O'Leary, 1993]. Here, the deviation of the reconstructed parameter from the prior (regularization term) is plotted against the deviation of the fitted model from the original data (data term). The optimal weighting factor w can be found by identifying the point of highest curvature.

HOTSPOT ANALYSIS So far, healthy tissue was considered either in vivo or in the simulation phantom representing physiologically distributed OEF and DBV values. In case of a pathology, this assumption might not hold and OEF or DBV might significantly deviate from the physiological expected conditions. For this, an additional OEF map was created to include pathologic conditions. A 128 x 128 pixels OEF map was created with the upper half set to a baseline value of 40%. An increased OEF of 80% was assigned to the lower half of the map representing a hotspot of high oxygen demand. Again, the weighting factor is varied and the influence on the reconstructed parameter is examined.

3.7.2 *Artificial Neural Network*

An ANN describes a network of connected nodes in analogy to the neurons in a biological nervous system. Typically, the network consists of several nodes that are organized in separate layers. The raw data that is to be processed is fed into the input layer. The output layer represents the parameters that are to be extracted from the data. Both layers are connected by one or more hidden layers. Nodes pass on information to subsequent nodes depending on the weights of their input and an activation function. The process of adjusting the characteristics of the nodes within the hidden layer in order to optimize the parameter reconstruction is called training. For training, simulated GESSE data was created according to Equation 3.6 mimicking the clinical sequence parameters. This was done in analogy to Domsch et al. [2018].

The ANN consists of an input layer of 32 nodes, a hidden layer of 10 nodes, and an output layer of 4 nodes. The input layer receives the signal at each TE. The output layer represents the 4 parameters of interest, namely S_0, R_2, OEF and DBV. A schematic visualization of the network architecture is depicted in Figure 3.8.

TRAINING SET VARIATION For the optimization of the training set, four different factors were examined: First, the parameter distribution of the training data, i. e. uniform, one Gaussian for the whole brain and two separate Gaussian distributions for GM and WM. Second, the size of the training set, i. e. the number of simulated voxels. Third, the hidden layer size, i. e. the number

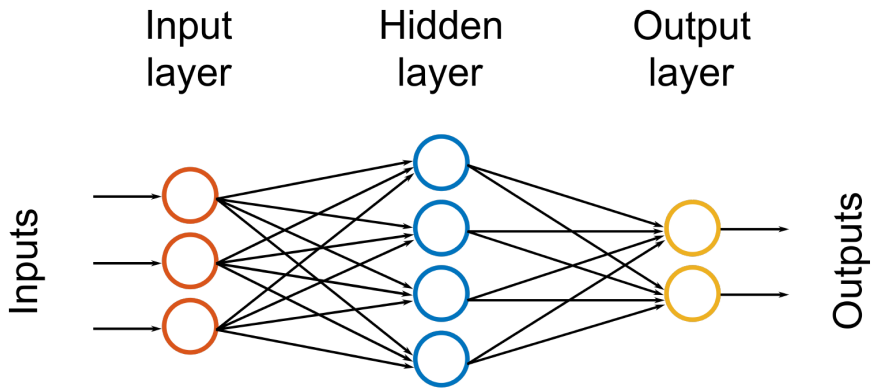

Figure 3.8: An exemplary representation of the ANN architecture is shown. The network consists of the input layer (orange), hidden layer (blue) and output layer (yellow). Each node within one layer is connected with all nodes in the neighboring layers. Figure adapted from Hubertus [2019].

of nodes within the hidden layer. Fourth, the SNR of the training set data. The uniform distribution was randomly chosen from the range of $R_2 = [1...30]$ Hz, OEF= $[1...100]$% and DBV = $[0.1...10]$%. The first Gaussian distribution was defined as $R_2 = 12 \pm 4$ Hz, OEF= 40 ± 10% and DBV = 3 ± 1%. The second Gaussian distribution was defined as $R_2 = 11.5 \pm 4$ Hz, OEF= 40 ± 10% and DBV = 4 ± 1% for GM and $R_2 = 13 \pm 4$ Hz, OEF= 40 ± 10% and DBV = 2 ± 1% for WM. Gaussian noise corresponding to an SNR of 100 was added. The size of the data set was 10^5. The training data were normalized to $S_0 = 1$ in order to reduce the degrees of freedom which enables more data points to be used for the training of the critical parameters.

For the variation of the hidden layer size, the number was changed in the range of $[5, 10, 15, ..., 30]$. The second Gaussian distribution was used and all other parameters stayed the same. For the variation of the training set size, the number of voxels was varied in the range between 10^2 and 10^6. The training SNR was varied from 25 to 200.

GROUND TRUTH VARIATION Two cases were examined: First, the SNR of the input data was varied in the range of $[30, 40, 50, ..., 300]$ with constant parameters $R_2 = 12$ Hz, OEF = 40% and DBV = 3% as ground truth. For each SNR value a set of 1000 voxels was created. The results of these voxels were averaged to obtain mean and standard deviation for each parameter and SNR value.

Second, the ground truth was varied in the range of $R_2 = [5, 7, 9, ..., 25]$ Hz, OEF = $[20, 22, 24, ..., 60]$% and DBV = $[2.0, 2.2, 2.4, ..., 6.0]$% with all possible combinations and a constant SNR of 100.

3.7.3 *Comparison*

7 healthy volunteers (4 male, 3 female, 28 ± 3 years old) were examined with the GESSE sequence and the results of the three methods LS, regularization

and ANN were compared. Regions of GM and WM were compared and tested for significant differences.

3.8 IN VIVO STUDIES

3.8.1 *Oxygenation and Perfusion in Smokers*

MEASUREMENT For this study, MRI data was acquired with both the GESSE sequence as well as the MP sequences. The evaluation was performed for the ANN method and the MP method.

20 healthy dependent smokers (13 male, 7 female, 29 ± 9 years old) were recruited for this study, which was approved by the local ethics committee. All participants were asked to refrain from smoking at least 8 hours prior to the measurement and their smoking status was determined with a carbon monoxide breath test. 2D GESSE, 2D mGRE, 2D mSE, 2D-EPI pCASL and T_1-weighted MPRAGE sequences were acquired. The sequence parameters are given in Section 3.2. After scanning, the subjects took a break of 30 minutes and smoked one cigarette before all measurements were repeated once more. The study workflow is schematically shown in Figure 3.9.

10 healthy never-smokers (6 male, 4 female, 21 ± 4 years old) were also recruited for the study. Never-smokers were defined as individuals with a lifetime consumption of cigarettes < 20. They underwent the same procedure except for the smoking break and second session of MRI measurements.

STATISTICS Paired t-tests between the pre- and post-smoking state were performed for OEF, CBF and $CMRO_2$ in all segmented ROIs to determine possible acute effects of smoking. In addition, smokers in the pre- and post-smoking state were compared with never-smokers for the same parameters in all segmented ROIs to determine possible chronic effects. The level of statistical significance was set at $\alpha = 0.01$ for all analyses due to the large number of tested regions. For the statistical analysis, MATLAB R2017a was used.

3.8.2 *Oxygenation in Tumor Patients*

MEASUREMENT 3 patients with brain tumors were included in this study. Information about the patients is given in Table 3.1. All patients were scanned at University Hospital Mannheim at a 3 T Siemens Trio scanner with the GESSE sequence. The study was approved by the local ethics committee of the Medizinische Fakultät Mannheim. The individual patients were scanned over a longer timespan. During this timespan, the sequence parameters were further developed. This results in two different parameter sets that were used for these patients. The parameter sets are given in Table 3.2. In addition, a T_1 weighted MPRAGE sequence with contrast agent was acquired as a morphological reference.

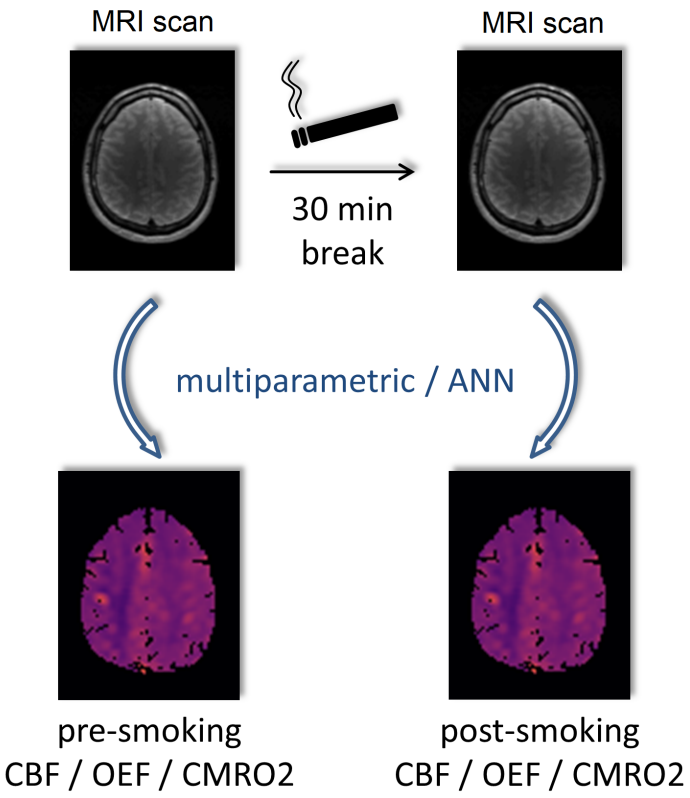

Figure 3.9: Workflow of the smoker study. In case of the never-smokers, only one measurement block was performed. In case of the smokers, the first block was followed by a smoking break for one cigarette and a second identical measurement block. Due to the fact that this study was embedded in a set of other studies (i. e. fMRI, MP and GESSE), additional sequences were conducted in the measurement blocks leading to measurement time of one hour.

Table 3.1: Information about the tumor patients including age, sex and diagnosis. Patient 1 and 2 were scanned with the sequence parameter set 1 and patient 3 with the parameter set 2 (see Table 3.2).

Patient #	Age [yrs]	sex	diagnosis
1	73	m	glioblastoma (post-operative) + metastases
2	63	m	oral cancer + metastases
3	60	f	glioblastoma (post-radiotherapy)

Table 3.2: Parameter sets of the GESSE sequence for the measurement of tumor patients.

Parameter set #	1	2
TR [ms]	778	2779
TE_1 [ms]	29	29
ΔTE [ms]	2	2
matrix size	128 x 96	128 x 96
resolution [mm^3]	2 x 2 x 2	2 x 2 x 2
# slices	7	25
# averages	10	3
acquisition time [min:sec]	10:00	10:00
flip angle [°]	23	90

STATISTICS In order to find significant differences in the comparison of healthy and tumor ROIs, Student's t-tests are performed. For this statistical analysis, MATLAB R2017a was used. The level of statistical significance was set at $\alpha = 0.05$ for all analyses.

4 RESULTS

In this chapter, the results of this thesis are shown. Based on the standard methods LS and MP, the status quo is presented. Then, the novel reconstruction methods are evaluated using simulated data and in vivo data of healthy volunteers. Last, these methods are applied to smokers and tumor patients. In the smokers, comparisons are drawn between never-smokers and smokers as well as smokers between the pre- vs. post-smoking state. In the tumor patients, the qBOLD parameters in the tumor region are compared to the contralateral side of the brain.

4.1 STANDARD RECONSTRUCTION METHODS

An exemplary visualization of the GESSE images is shown together with a T_1 weighted image as reference in Figure 4.1. An exemplary signal curve is shown for a representative voxel in GM and in WM in Figure 4.2. Additionally, the fit residuals are shown. The LS reconstruction yields maps of the four qBOLD parameters S_0, R_2, OEF and DBV as depicted exemplarily for one healthy volunteer in Figure 4.3. The S_0 map shows the same contrast as the GESSE image at the SE. A region of higher intensity is visible in the frontal part of the brain due to the receive coil's sensitivity profile. The R_2 map shows a mean and SD of (14.6 ± 1.1) Hz in WM and (13.2 ± 1.5) Hz in GM, respectively. In contrast to S_0 and R_2, the maps of OEF and DBV are dominated by reconstruction artifacts leading to regions of exceedingly high or low values.

Representative parameter maps of the MP method are shown in Figure 4.4 together with a T_2 weighted image as reference. In Table 4.1, the mean and SD are listed for all parameters.

Table 4.1: Mean and standard deviation of the multi-parametric qBOLD parameters for a representative healthy volunteer in gray and white matter regions.

	GM	WM
R_2* [Hz]	18.7 ± 4.3	20.6 ± 2.5
R_2 [Hz]	10.4 ± 2.4	12.4 ± 1.8
R_2' [Hz]	8.4 ± 4.7	8.2 ± 2.7
CBF [ml/100 g/min]	45.5 ± 21.9	17.7 ± 12.6
DBV [ml/100 g]	5.2 ± 1.3	3.2 ± 1.5
OEF [%]	57.8 ± 63.8	129.0 ± 168.1
CMRO2 [µmol/100 g/min]	163.2 ± 118.2	94.9 ± 66.4

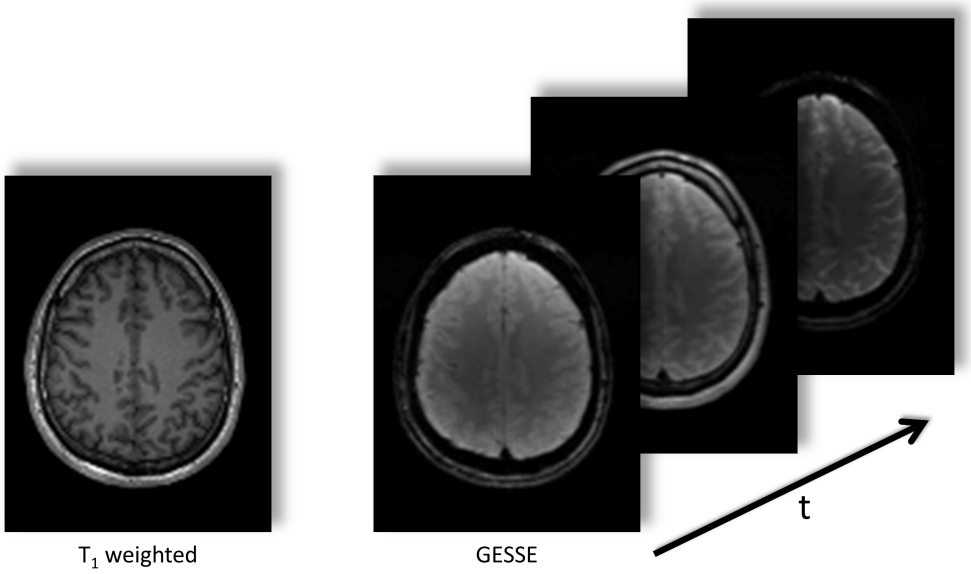

Figure 4.1: On the left, a T_1 weighted image is shown as a reference. On the right, 3 out of 32 images of the GESSE time series are shown schematically for different TEs.

4.2 NOVEL RECONSTRUCTION METHODS

4.2.1 *Regularization*

IN VIVO DEMONSTRATION The regularization method is first demonstrated in vivo on one healthy volunteer exemplarily. The OEF maps of the representative subject are shown in Figure 4.5. The weighting factor is set to $w = 0.05, 5$ and 500 (left, top to bottom). Additionally, the histograms of the OEF values corresponding to GM and WM are shown for the same weighting factors (right, top to bottom). It is apparent that the parameter distribution becomes more narrow for increasing weighting factor and approaches the prior value of the regularization. The mean and SD changes from $(42 \pm 22)\%$ to $(37 \pm 7)\%$ to $(39 \pm 2)\%$ in GM and from $(41 \pm 24)\%$ to $(37 \pm 6)\%$ to $(38 \pm 1)\%$ in WM for the three settings of w. The regions of exceedingly high OEF are more and more suppressed. However, also the image contrast decreases with increasing w.

In Figure 4.6, the analog depiction is shown for DBV. Qualitatively, the same behavior can be seen. Here, mean and SD change from $(3.1 \pm 2.6)\%$ to $(2.6 \pm 1.5)\%$ to $(2.5 \pm 0.6)\%$ in GM and from $(2.4 \pm 2.7)\%$ to $(1.6 \pm 1.1)\%$ to $(2.2 \pm 0.4)\%$ in WM.

SIMULATION The influence of the regularization weighting factor on the OEF maps is depicted in Figure 4.7. Again, the corresponding histograms are shown alongside. Similarly, Figure 4.8 shows the results for DBV.

The accuracy and precision of OEF and DBV in both the simulation phantom and in vivo data is shown in Figure 4.9. On the left, the phantom data and, on the right, the in vivo data is shown. In the top row, the mean OEF and

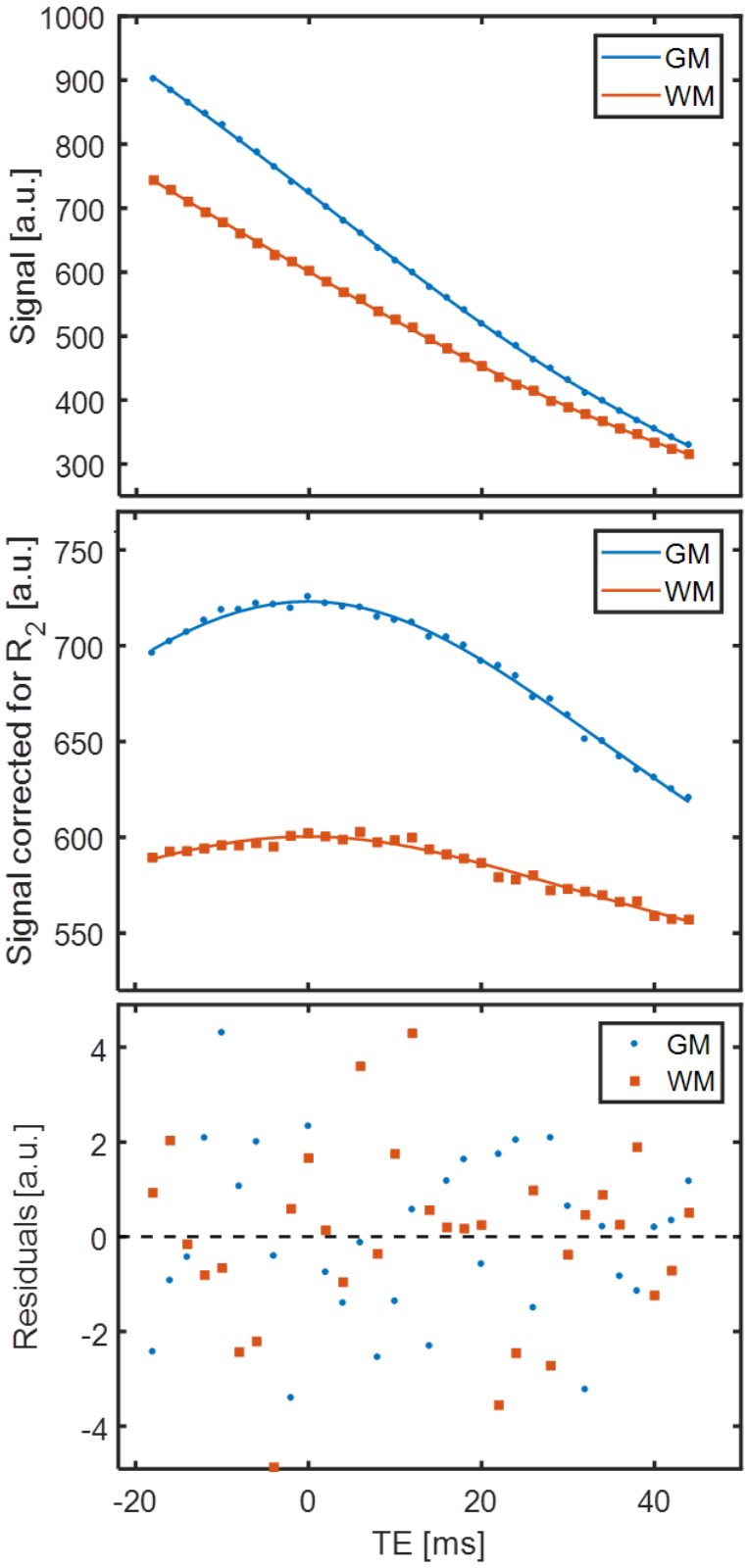

Figure 4.2: On top, the signal evolution of the GESSE sequence is shown for an exemplary voxel within GM (blue) and WM (orange) together with the fitted qBOLD model function. In the middle, the signal is corrected for R_2 relaxation. At the bottom, the residuals of the fitted curves to the acquired data points are shown. The time axis is referenced to the echo time of the spin echo.

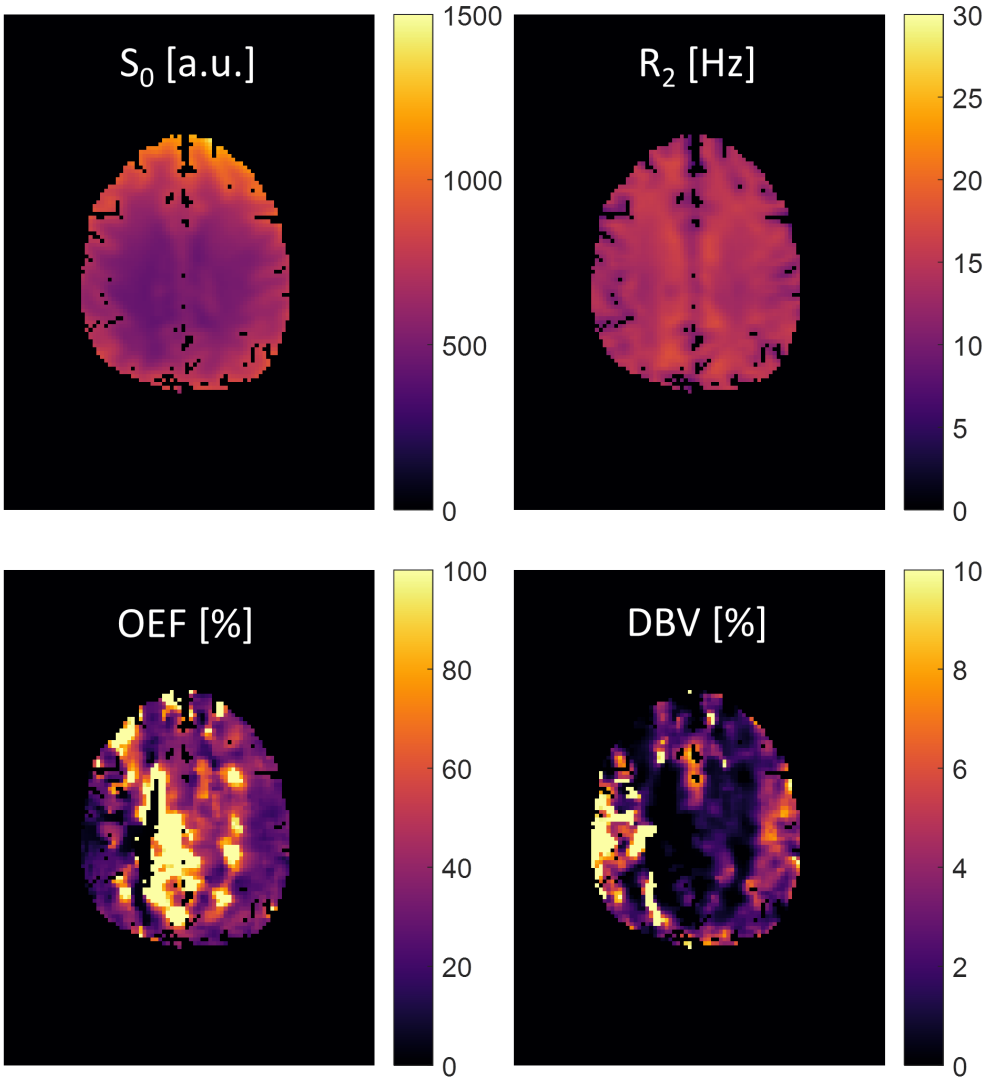

Figure 4.3: Maps of the qBOLD parameters S_0, R_2, OEF and DBV for one healthy volunteer reconstructed with the Least Squares (LS) method. The OEF and DBV maps show areas of unphysiologically high or low values.

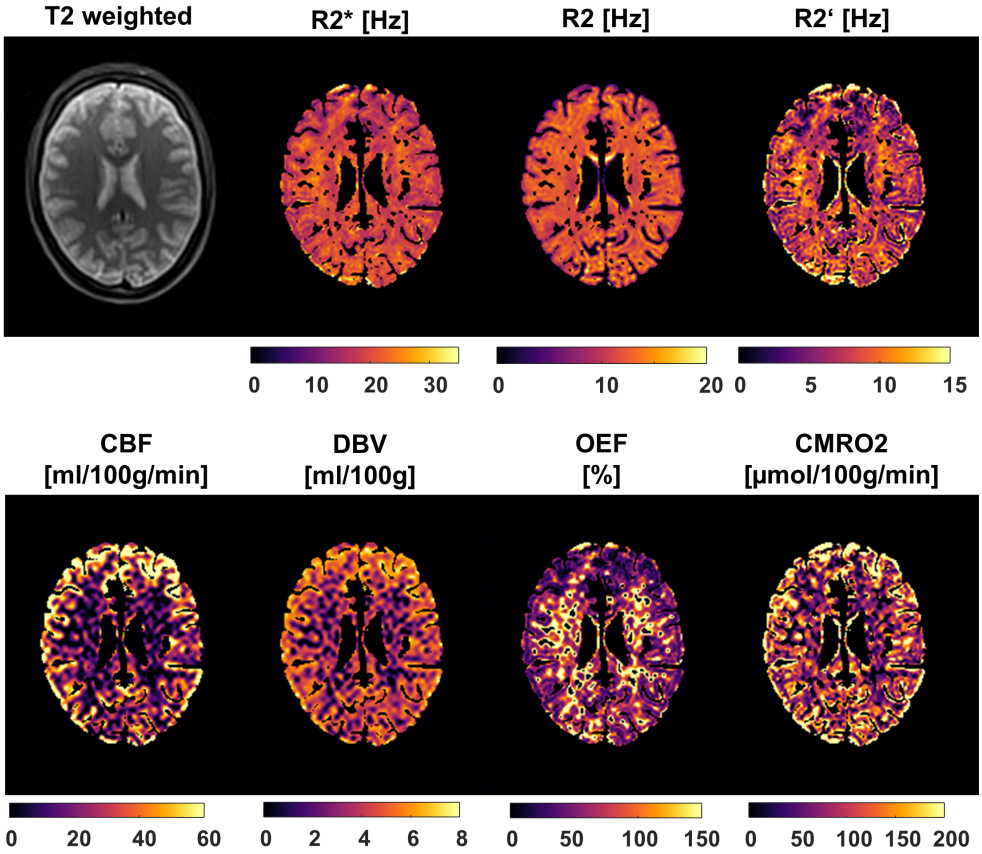

Figure 4.4: Parameter maps and T_2 weighted image of a representative slice of a healthy volunteer reconstructed with the multi-parametric method. The parameter maps depict R_2*, R_2, $R_2' = R_2$* - R_2, CBF, DBV, OEF and $CMRO_2$.

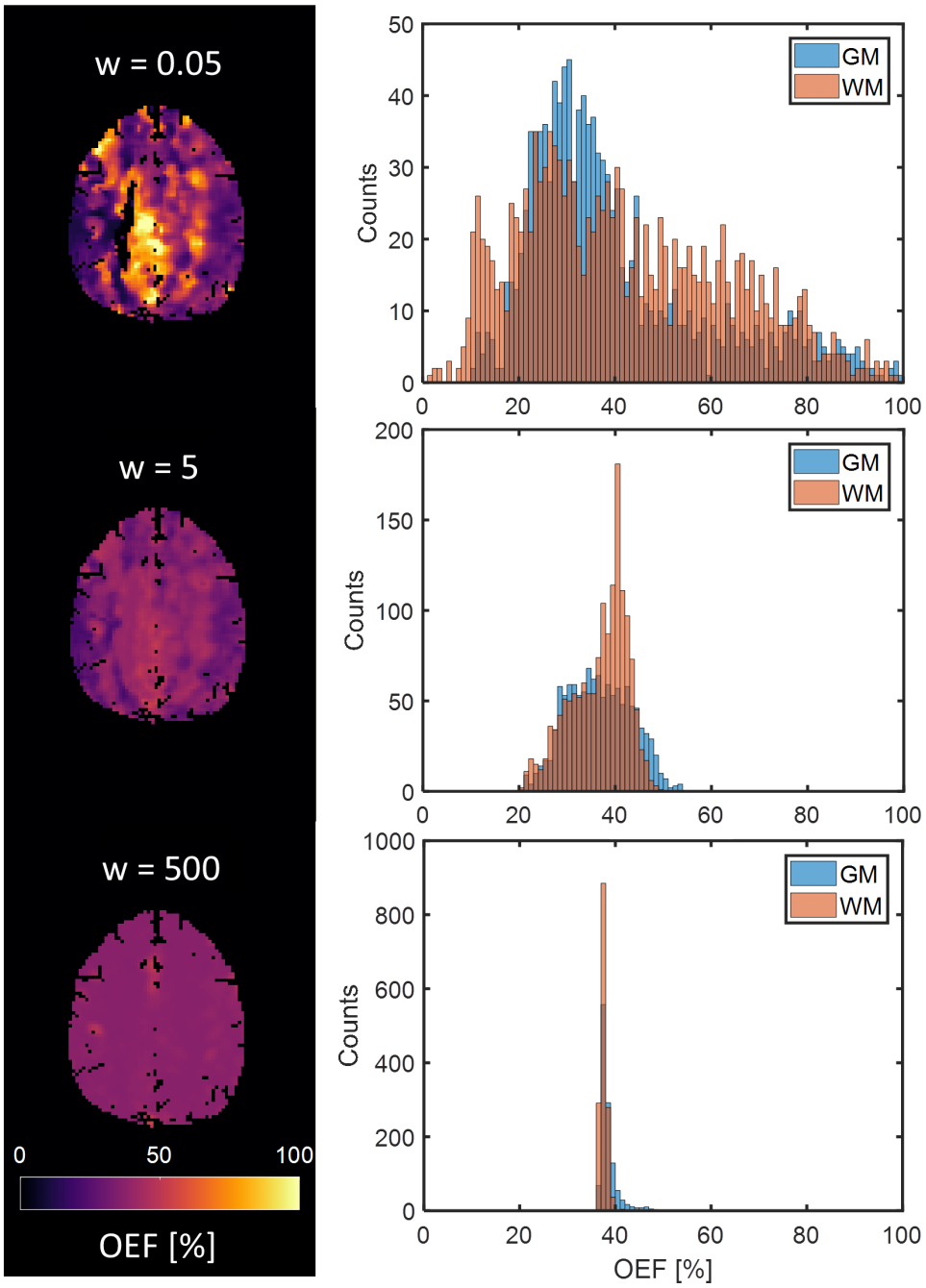

Figure 4.5: OEF maps of one healthy volunteer reconstructed with the regularization method showing the influence of the weighting factor w. The weighting factor changes from $w = 0.05, 5$ and 500 (left, top to bottom). On the right hand side, the respective histograms are shown for the same weighting factors subdivided into GM and WM voxels.

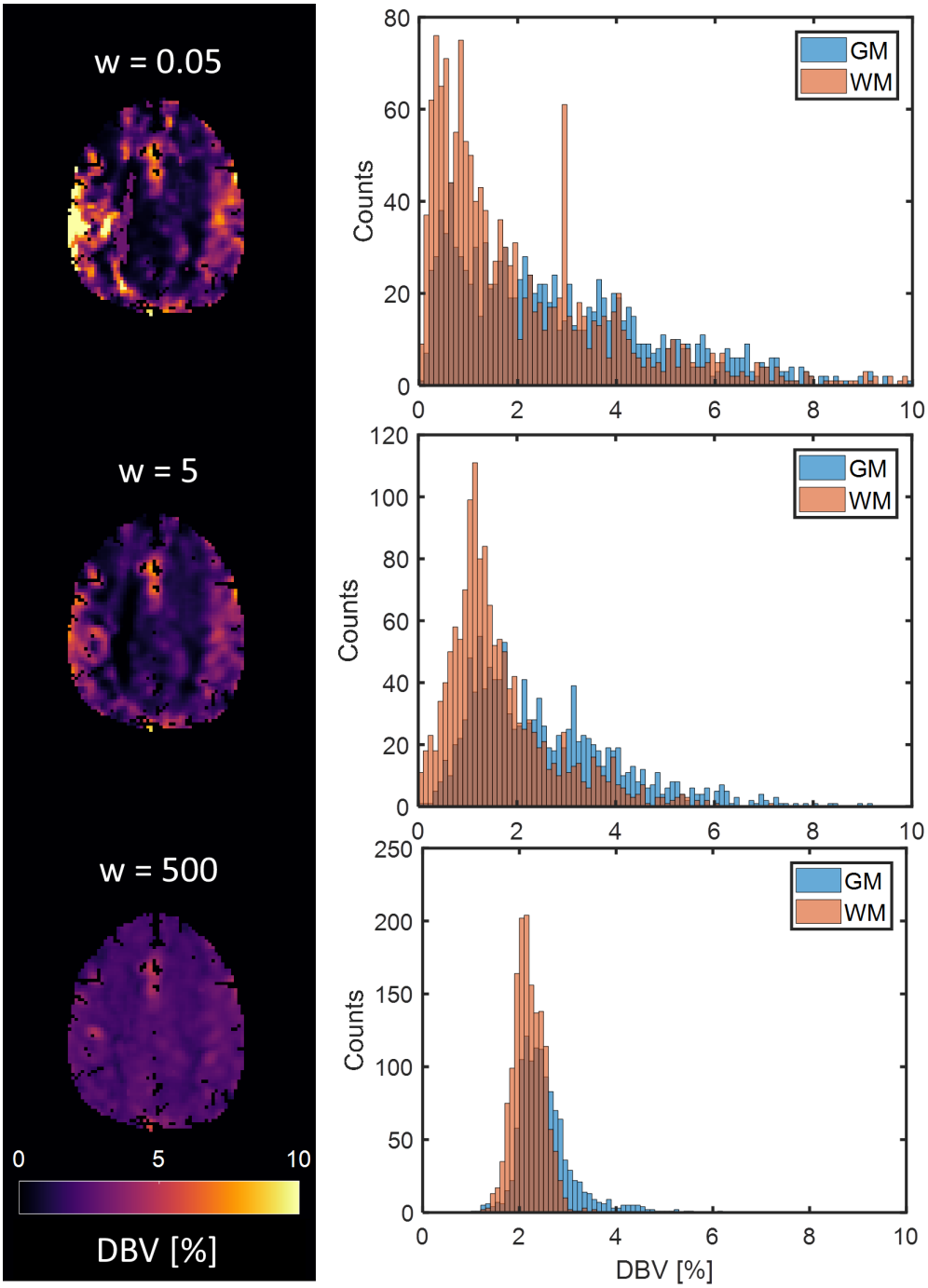

Figure 4.6: DBV maps of one healthy volunteer reconstructed with the regularization method showing the influence of the weighting factor w. The weighting factor changes from $w = 0.05, 5$ and 500 (left, top to bottom). On the right hand side, the respective histograms are shown for the same weighting factors subdivided into GM and WM voxels.

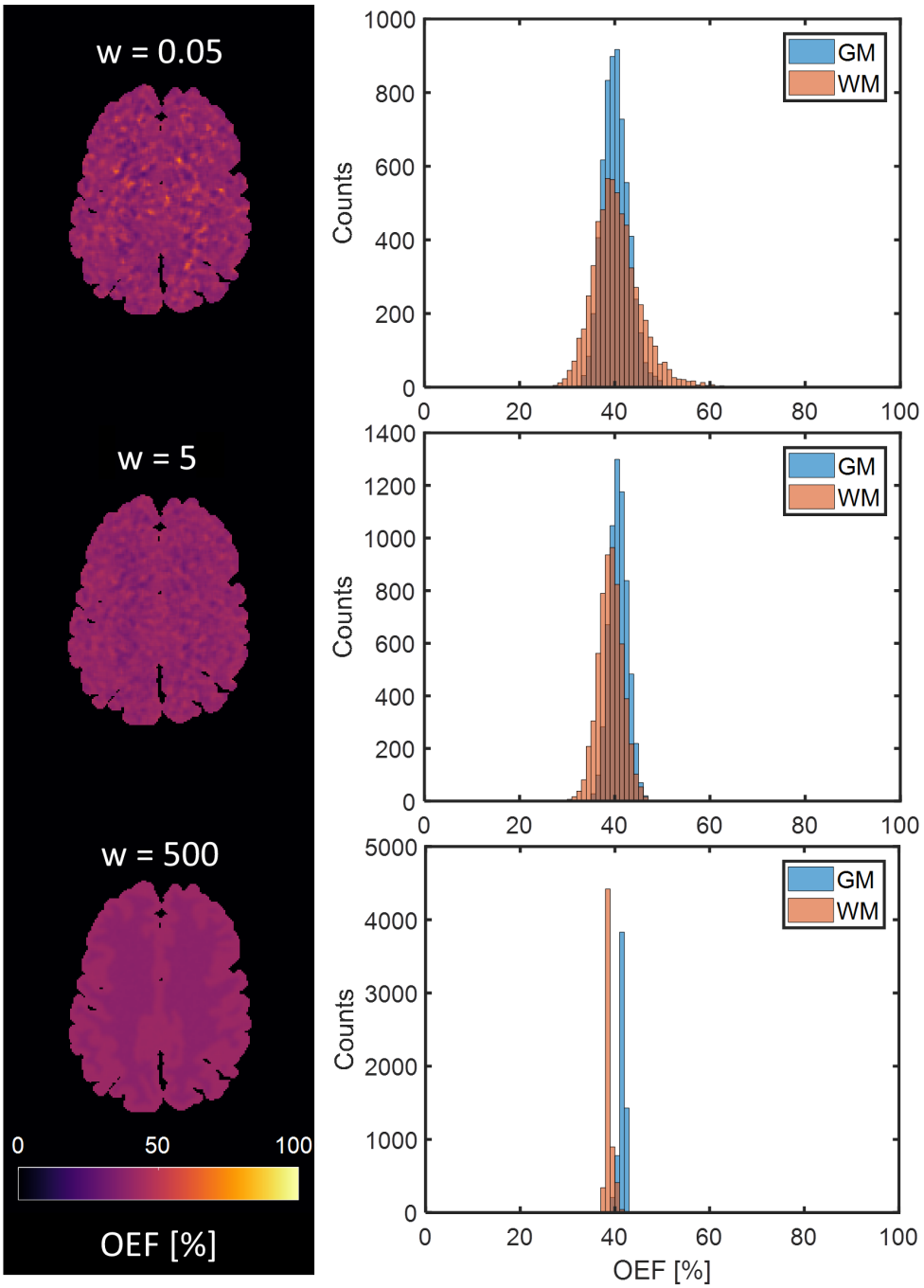

Figure 4.7: OEF maps of the simulation phantom reconstructed with the regularization method showing the influence of the weighting factor w. The weighting factor changes from $w = 0.05, 5$ and 500 (left, top to bottom). On the right hand side, the respective histograms are shown for the same weighting factors subdivided into GM and WM voxels.

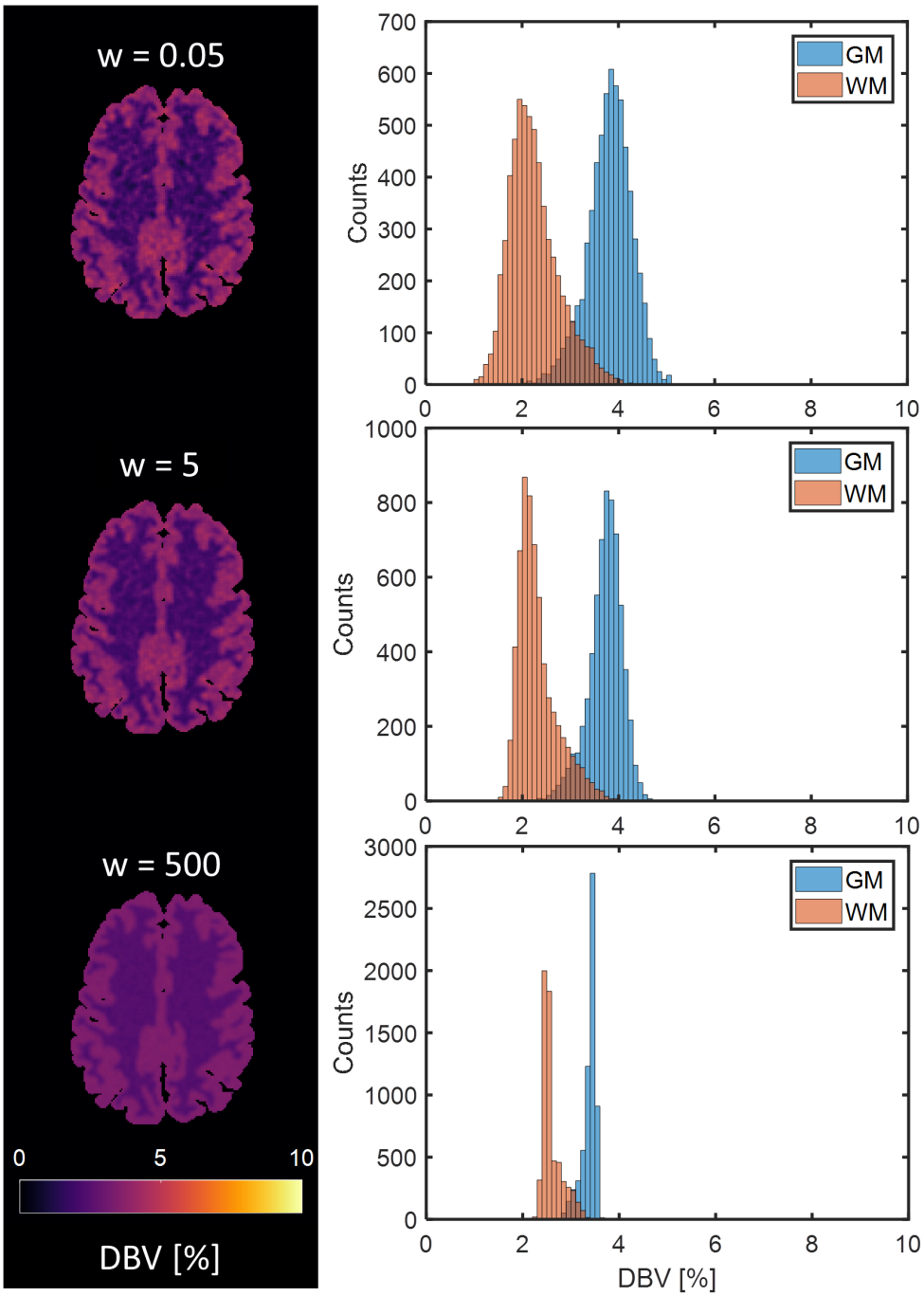

Figure 4.8: DBV maps of the simulation phantom reconstructed with the regularization method showing the influence of the weighting factor w. The weighting factor changes from $w = 0.05, 5$ and 500 (left, top to bottom). On the right hand side, the respective histograms are shown for the same weighting factors subdivided into GM and WM voxels.

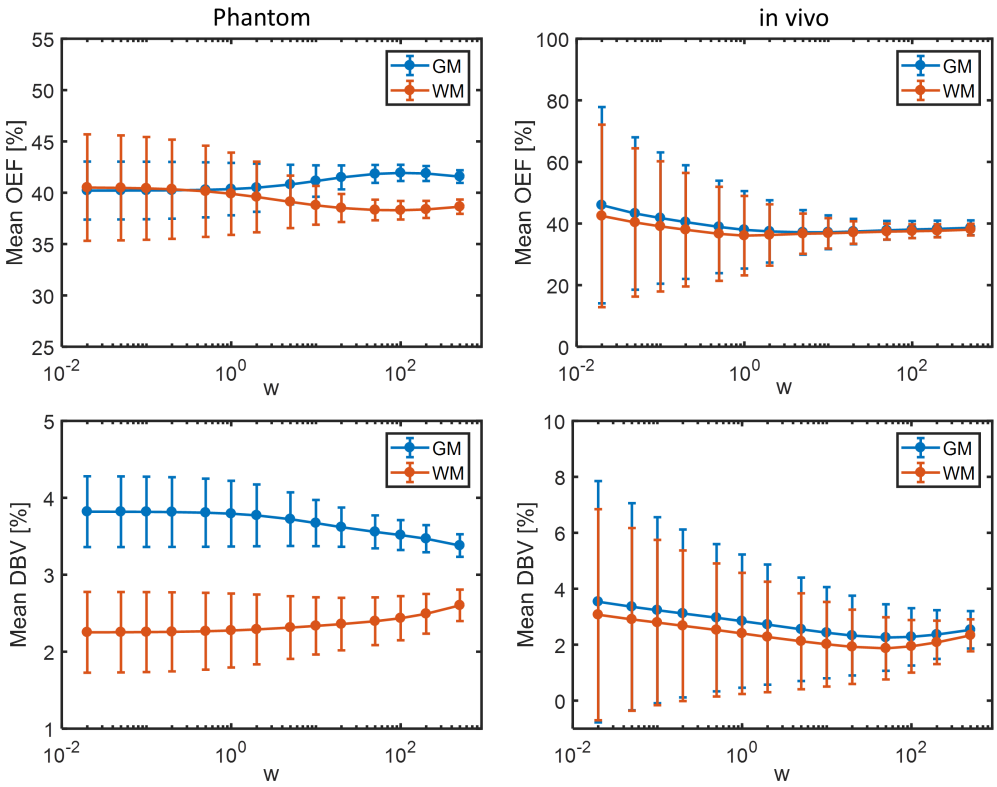

Figure 4.9: Mean OEF and DBV is plotted with the corresponding SD against the weighting factor w. On the left, the simulation phantom and, on the right, the in vivo data is shown. The ground truth of OEF is 40% for both GM and WM. The ground truth for DBV is 4% for GM and 2% for WM. Note the different scales of the y-axes due to the higher precision within the simulation phantom.

the respective SD as error bars are plotted against the weighting factor. In the phantom, the mean stays within a narrow range around the ground truth value of OEF $= 40\%$. With increasing w a bias of 5% from the ground truth is introduced for both GM and WM; however, in opposite directions. In vivo, the mean OEF approaches the ground truth with increasing w. The SD decreases continuously in all cases. It changes from 12% to less than 1% relative SD in the phantom and from 80% to 6% in vivo.

In the bottom row, the mean DBV is shown with the SD as error bars. In the simulation phantom, the mean of GM and WM approaches the prior value of 3% from opposite directions with increased weighting. This increases the relative bias from 5% to 16% in GM and from 13% to 30% in WM. In vivo, the difference of GM and WM is not as prominent. Both curves approach a DBV value of approximately 2.5%. The relative SD decreases from almost 100% to 26%.

The results of the L-curve analysis are depicted in Figure 4.10 for both the simulation phantom and the in vivo data. The regularization term is defined as the difference of the reconstructed parameter to the prior. The data term is defined as the residuals of the model curve to the data points. The point at

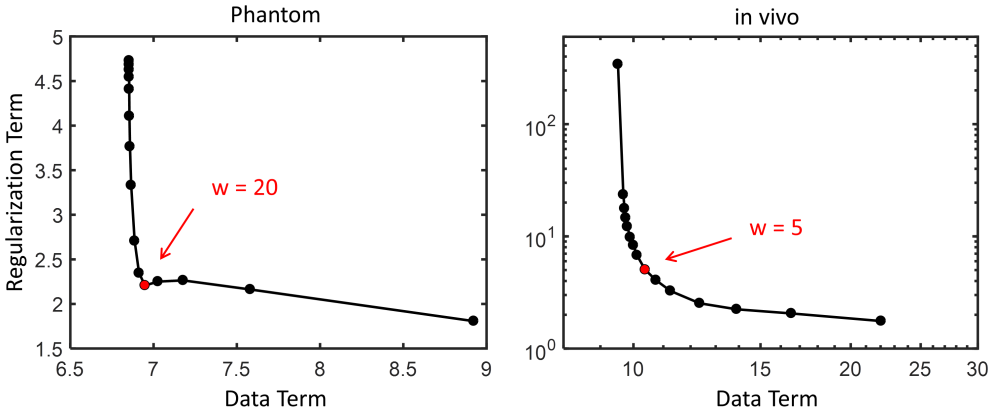

Figure 4.10: L-curve analysis for the regularization method. The deviation from the prior (regularization term) is plotted against the deviation from the data (data term). On the left hand side, the analysis is performed on the simulation phantom and on the right hand side on the in vivo data. The optimal weighting factor can be found by identifying the highest curvature (marked in red). Due to the large range of values, a log scale is used for the in vivo graph.

the highest curvature determines the optimal weighting factor. It is identified as $w = 20$ for the phantom data and as $w = 5$ in case of the in vivo data. Hence, for the following analysis of the in vivo studies, the regularization method was employed with a weighting factor of $w = 5$.

HOTSPOT ANALYSIS Another simulation is performed with a region of highly increased values of OEF $= 80\%$ labeled as 'hotspot' in order to model a pathology. This region is compared to a 'baseline' OEF level of 40% representing healthy tissue. In Figure 4.11, the OEF is plotted against the weighting factor w for the baseline and hotspot region, respectively.

The mean values and standard deviations of the baseline and hotspot region are reduced from $(54 \pm 42)\%$ to $(40 \pm 0.02)\%$ and $(93 \pm 50)\%$ to $(40 \pm 0.04)\%$, respectively, with increasing weighting factor. Since both regions converge towards the prior, an increasing bias is introduced with rising weighting factor especially in the hotspot region. As the variances of both regions concurrently decrease, a range of weighting factors from approximately 0.2 to 200 is observable, in which the mean values do not overlap within one standard deviation.

4.2.2 *Artificial Neural Network*

In this subsection, the results of the ANN method are presented. The method uses simulated GESSE data for training an ANN in order to learn to reconstruct the qBOLD parameters from the measured data.

FEASIBILITY First, the ANN is applied exemplarily to in vivo data of a healthy volunteer to demonstrate the feasibility of the method. In Figure 4.12,

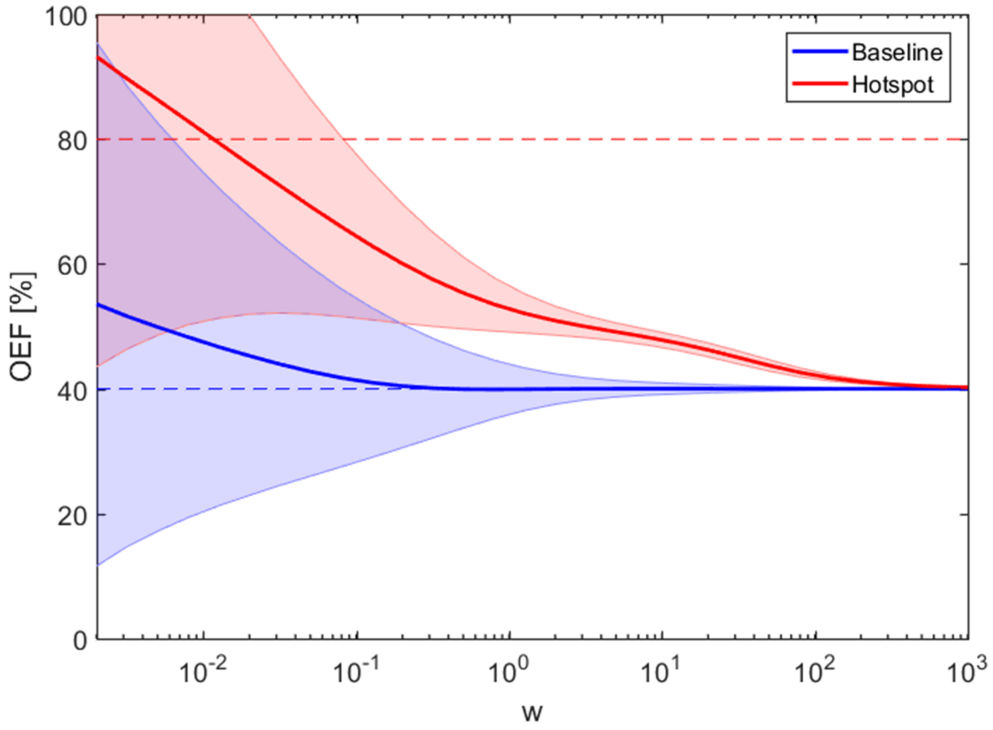

Figure 4.11: Mean values of the reconstructed OEF in the baseline (blue) and hotspot (red) region plotted against the weighting factor w. The corresponding standard deviations are depicted as shaded areas. The dashed lines correspond to the respective ground truth of 40% and 80%.

the resulting parameter maps of R_2, OEF and DBV are shown together with the corresponding histograms. R_2 is found to be (13.2 ± 1.4) Hz in GM and (14.6 ± 1.0) Hz in WM. OEF yields $(35.5 \pm 4.5)\%$ in GM and $(31.6 \pm 3.4)\%$ in WM and DBV is $(2.6 \pm 0.7)\%$ in GM and $(2.2 \pm 0.4)\%$ in WM.

SIMULATION As comparison, the reconstructed parameter maps are shown for simulated data in Figure 4.13. Here, R_2 is found to be (11.5 ± 0.2) Hz in GM and (13.0 ± 0.2) Hz in WM. OEF yields $(44.0 \pm 2.6)\%$ in GM and $(35.9 \pm 2.9)\%$ in WM and DBV is $(3.6 \pm 0.2)\%$ in GM and $(2.6 \pm 0.2)\%$ in WM.

The training data set and the ANN architecture have several adjustable parameters, which can have an influence on the reconstructed parameters. The varied parameters are SNR, number of voxels and parameter distribution of the training set, as wells as the number of nodes within the hidden ANN layer (hidden layer size). The mean relative error of the qBOLD parameters is plotted against the varied parameters in Figure 4.14.

It shows that the Gaussian distribution yields higher accuracy and precision for both GM and WM. The mean relative deviation from the ground truth over all parameters decreased from 10% to below 1% for GM and from 20% to below 10%. The mean standard deviation could be approximately halved for both GM and WM. Accuracy and precision do not change significantly with the numbers of nodes in the hidden layer. Increasing the number of voxels in the training set increases both accuracy and precision. The mean relative error could be reduced from 7% to 1% for GM and from 13% to 3% in WM by increasing the number of training voxels from 10^2 to 10^6. The mean standard deviation was reduced by approximately one-third for both GM and WM. For the SNR variation, the accuracy stays almost constant for GM and slightly decreases for WM. However, the relative SD increases from 2% to 12% in GM and from 3% to 20% in WM.

For the following analysis of the in vivo studies, the ANN method was employed with the Gaussian parameter distribution with separate ground truth values for GM and WM, a hidden layer size of 10, a training set size of 10^6 and an SNR of 100, which corresponds approximately to the in vivo SNR.

For a further evaluation of the accuracy of the ANN method, the ground truth data set is changed. First, the ground truth SNR is changed from 30 to 300. The results of the ANNs trained with three different training SNR values are shown in Figure 4.15. Second, the ground truth values of OEF and DBV are changed. In Figure 4.16, 2D plots are shown to examine the correlation between the two parameters. The color depicts the estimated parameter whereas the ground truth parameters vary on a two-dimensional grid. It shows that the reconstructed OEF and DBV values do not only depend on the the parameter itself but also correlate with one another.

4.2.3 *Comparison*

Here, the methods of LS reconstruction, regularization and ANN are compared in vivo on data of healthy volunteers. A group of 7 healthy volunteers was

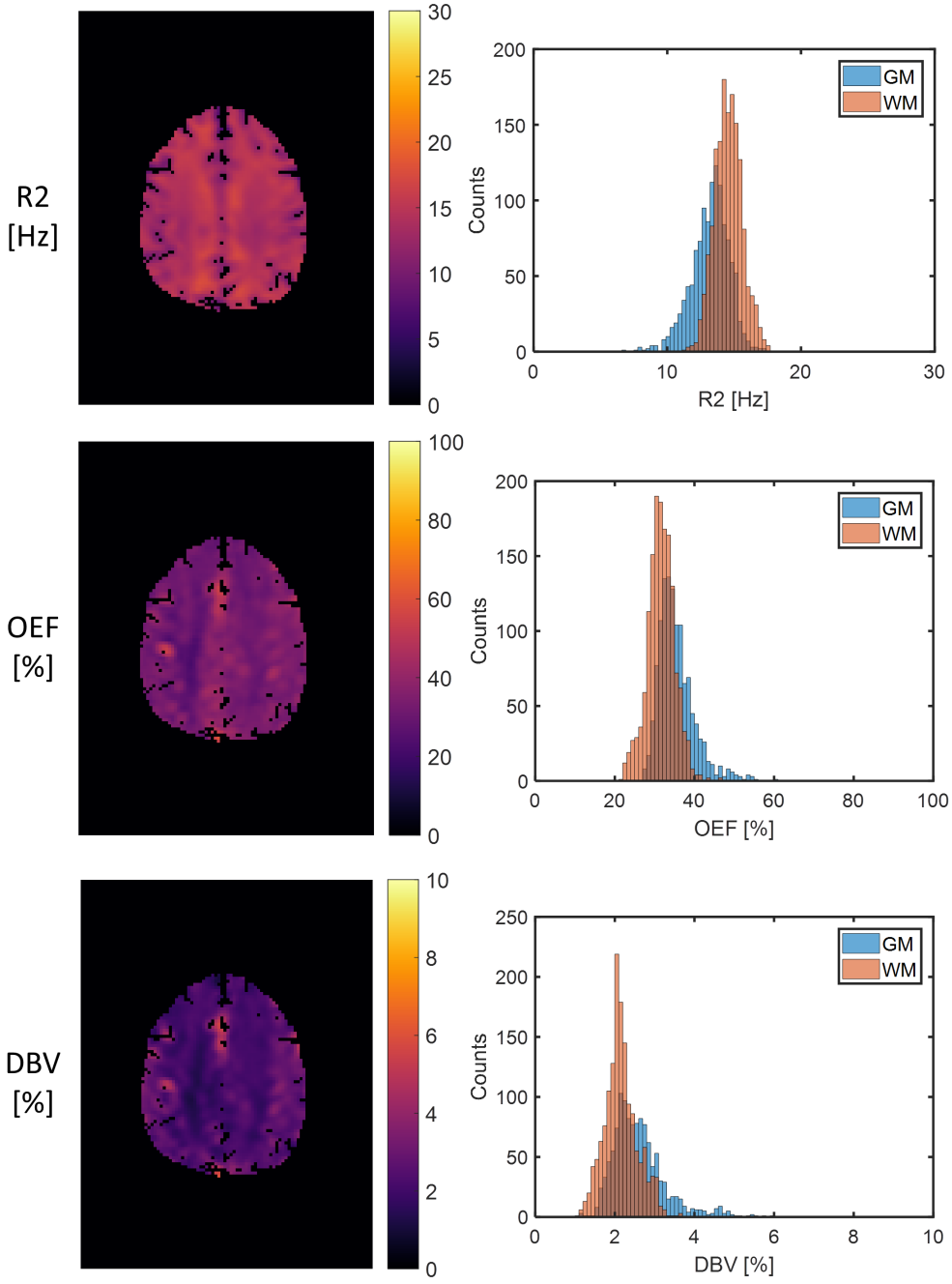

Figure 4.12: In vivo ANN reconstruction of the parameter maps R_2, OEF and DBV (left, top to bottom) and the corresponding histograms (right, top to bottom) are shown for a healthy volunteer. The voxels are divided into regions of gray and white matter.

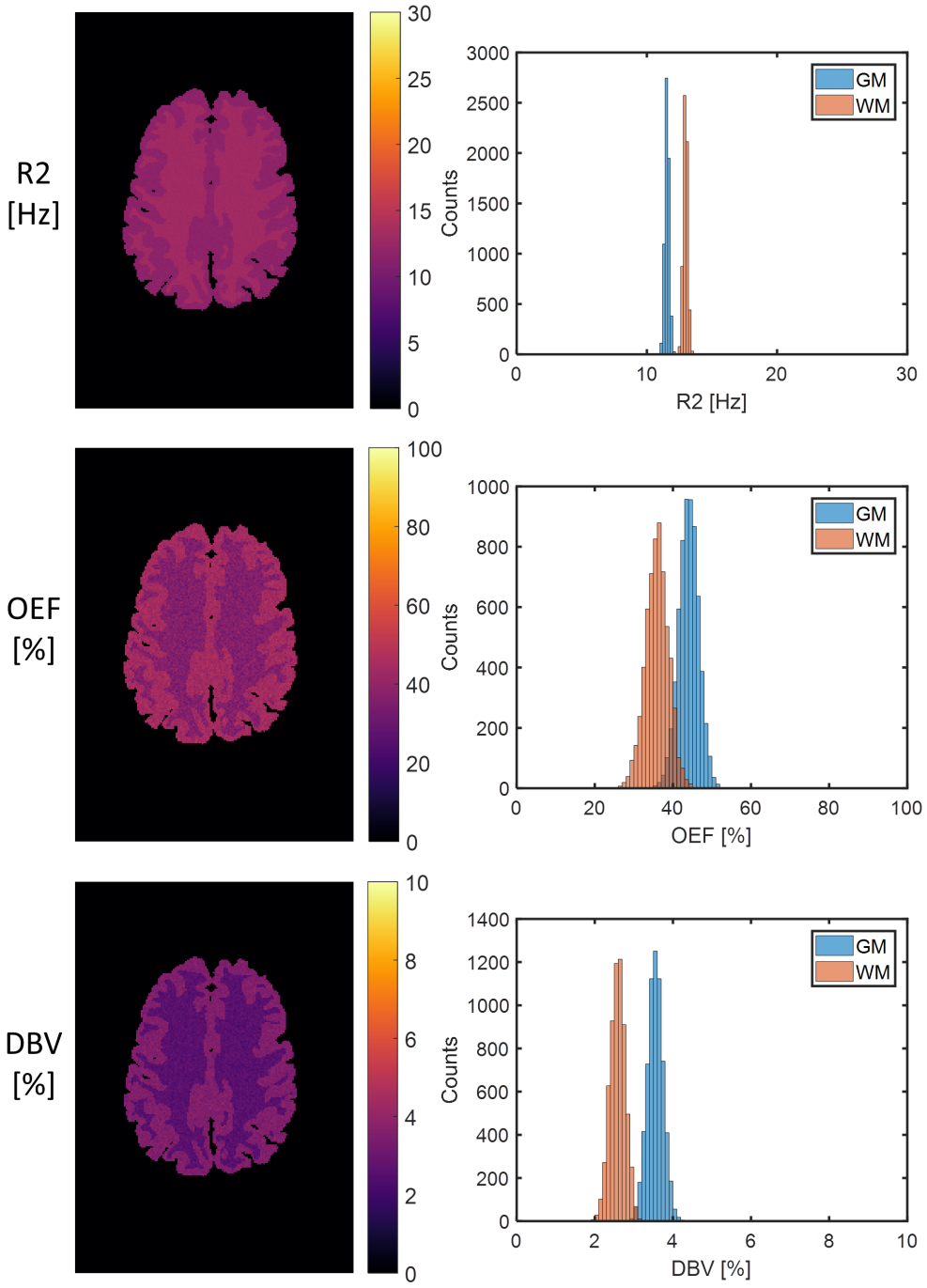

Figure 4.13: ANN reconstruction of the parameter maps R_2, OEF and DBV (left, top to bottom) and the corresponding histograms (right, top to bottom) are shown for simulated data. The voxels are divided into regions of GM and WM.

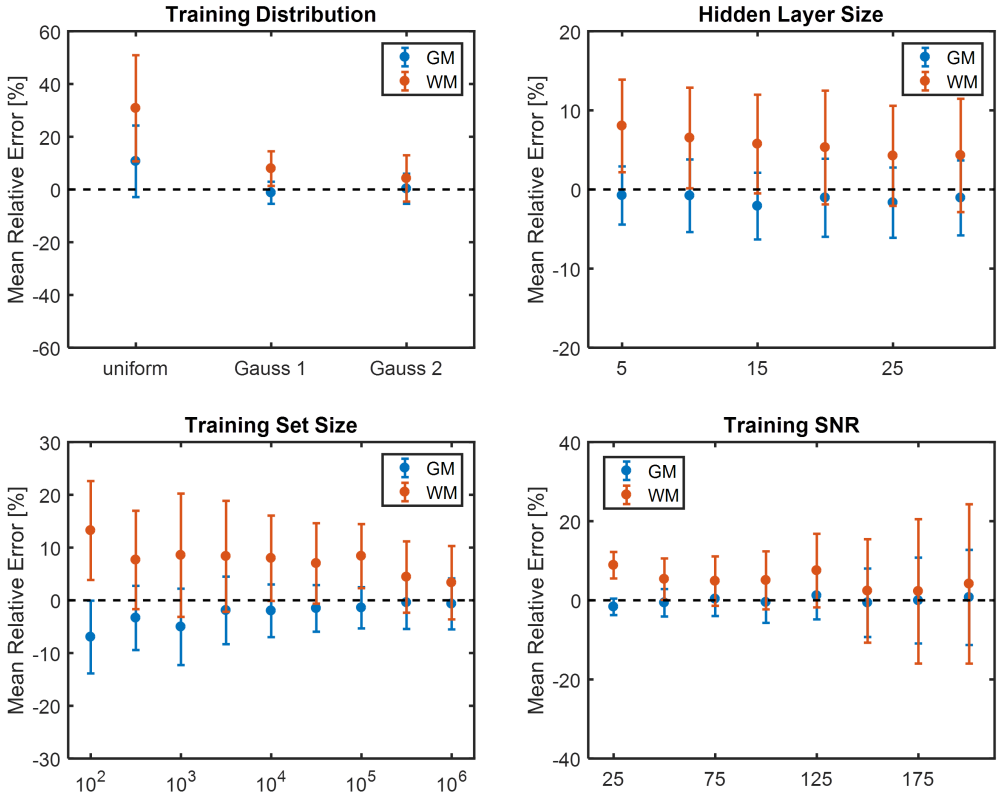

Figure 4.14: The mean relative error of the qBOLD parameters is plotted against the parameter distribution (top left), the number of nodes within the hidden layer (top right), the number of voxels of the training set (bottom left) and the SNR of the training set (bottom right). The SNR of the ground truth data was set to 100. Each graph shows the results for GM and WM, separately.

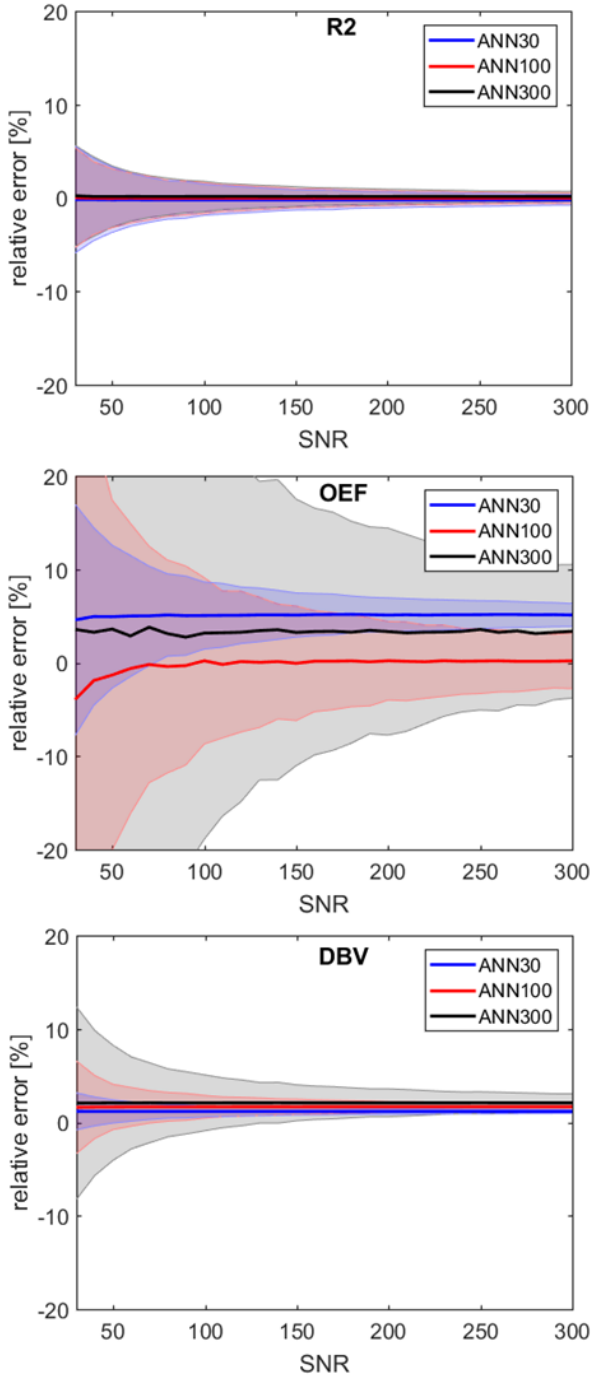

Figure 4.15: The relative error of the qBOLD parameters R_2, OEF and DBV (top to bottom) is plotted against the SNR of the ground truth. The shaded area corresponds to the standard deviation. The colors indicate ANNs trained with different SNR of 30, 100 and 300, respectively.

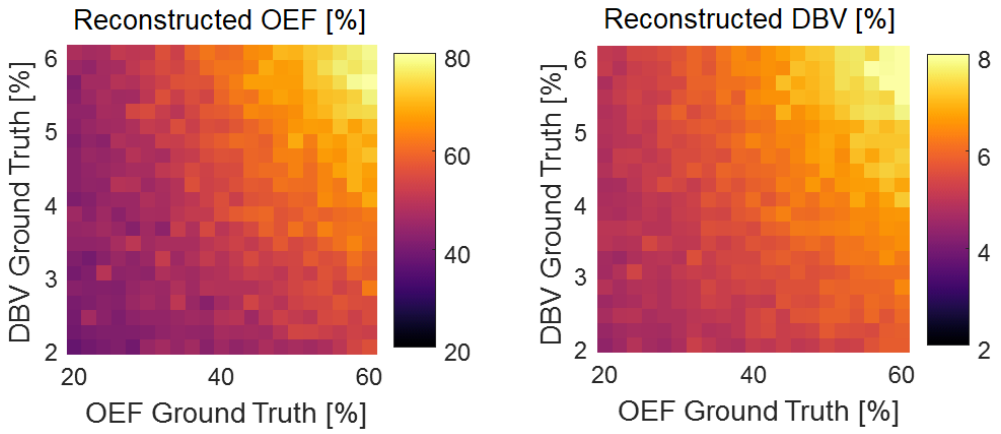

Figure 4.16: Ground truth variation: The ANN trained with an SNR of 100 was used to estimate the parameters (color-coded). OEF is shown on the left and DBV on the right. On the x- and y-axes the respective ground truth is varied.

Table 4.2: Mean and standard deviation of the qBOLD parameters for 7 healthy volunteers. It was distinguished between both the regularization and the ANN method and between gray and white matter regions.

	Regularization		ANN	
	GM	WM	GM	WM
R_2 [Hz]	13.1 ± 0.6	$14.4 \pm 0.7^{\dagger}$	13.1 ± 0.6	$14.4 \pm 0.8^{\dagger}$
OEF [%]	33.7 ± 2.0	34.2 ± 2.1	35.2 ± 1.3	$33.1 \pm 1.7^{\dagger}$
DBV [%]	3.1 ± 0.5	$2.5 \pm 0.7^{\dagger}$	2.9 ± 0.2	$2.6 \pm 0.3^{\dagger}$

† denotes a significant difference between GM and WM.

evaluated. In Figure 4.17, the R_2, OEF and DBV maps are shown for an exemplary subject reconstructed with the LS, regularization and ANN method. The corresponding histograms are depicted in Figure 4.18. In Figure 4.19, boxplots show the mean of GM and WM among all the subjects. The results are listed in Table 4.2.

4.3 IN VIVO STUDIES

First, the results of the smoker study are presented. Comparisons were drawn between smokers vs. never-smokers as well as smokers in the pre- vs. post-smoking state. Additionally, the results of the multi-parametric qBOLD method is compared with the GESSE-based ANN method. Second, the regularization method and the ANN method are both applied to brain tumor patients and the results within the tumor region are compared to the healthy contralateral side.

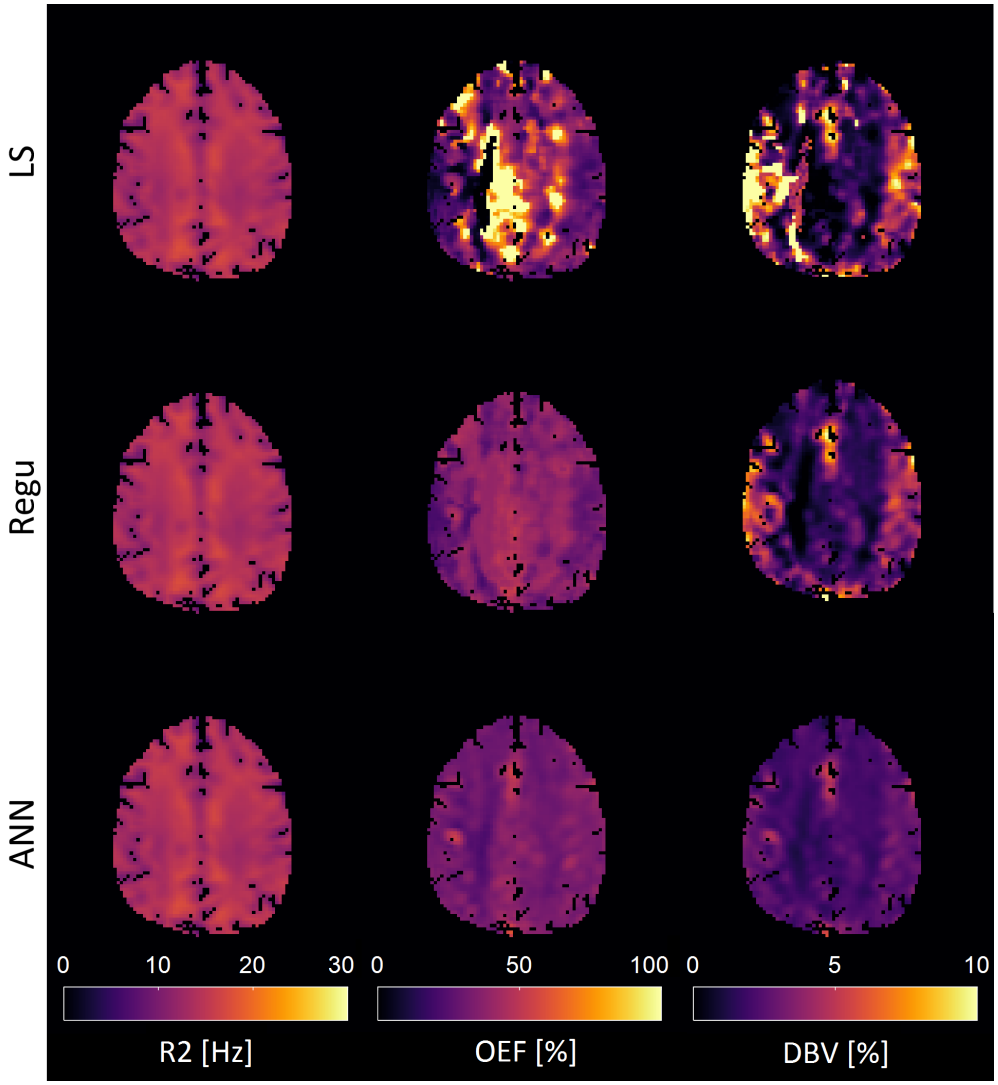

Figure 4.17: Parameter maps of R_2, OEF and DBV for an exemplary healthy volunteer reconstructed with each of the three methods LS, regularization and ANN (top to bottom).

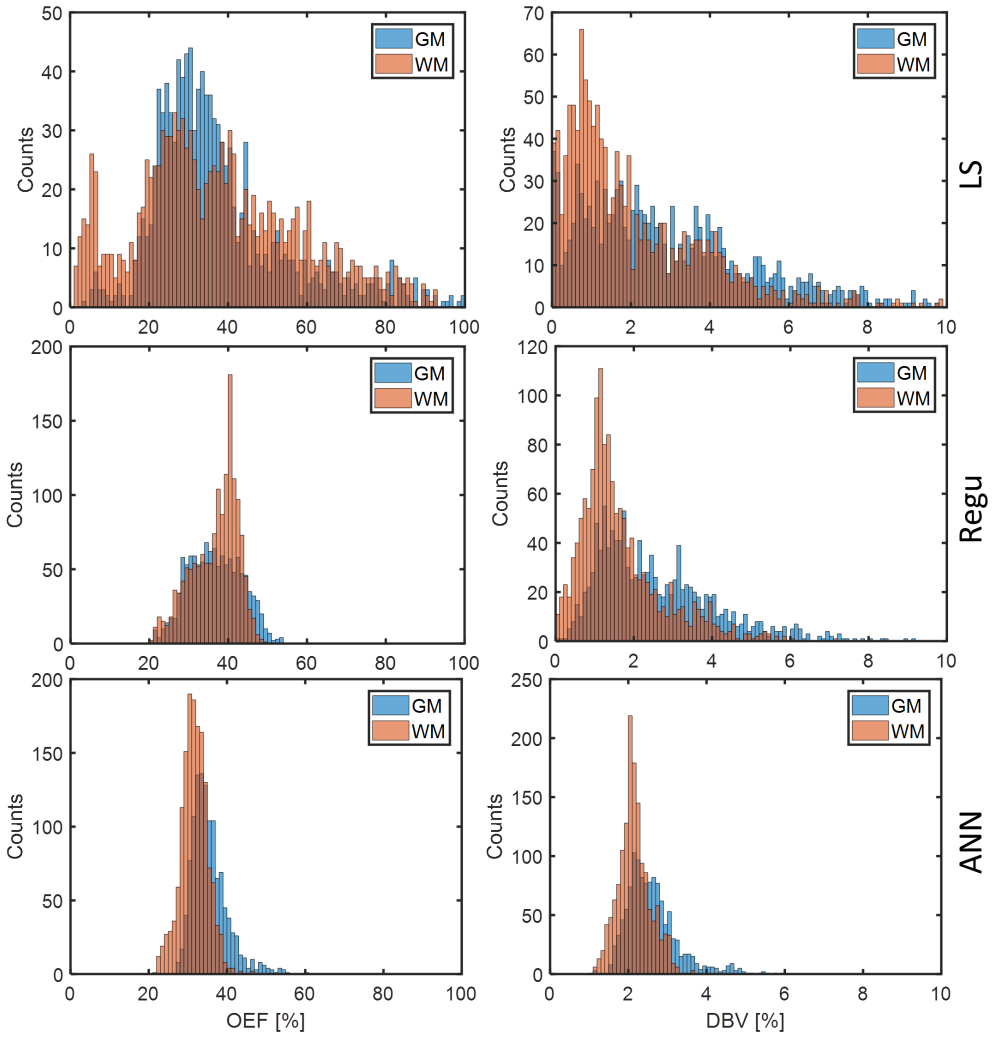

Figure 4.18: Histograms of the parameters OEF and DBV for an exemplary healthy volunteer reconstructed with the three methods LS, regularization and ANN. The parameter R_2 was omitted in this depiction because of the negligible difference between the methods.

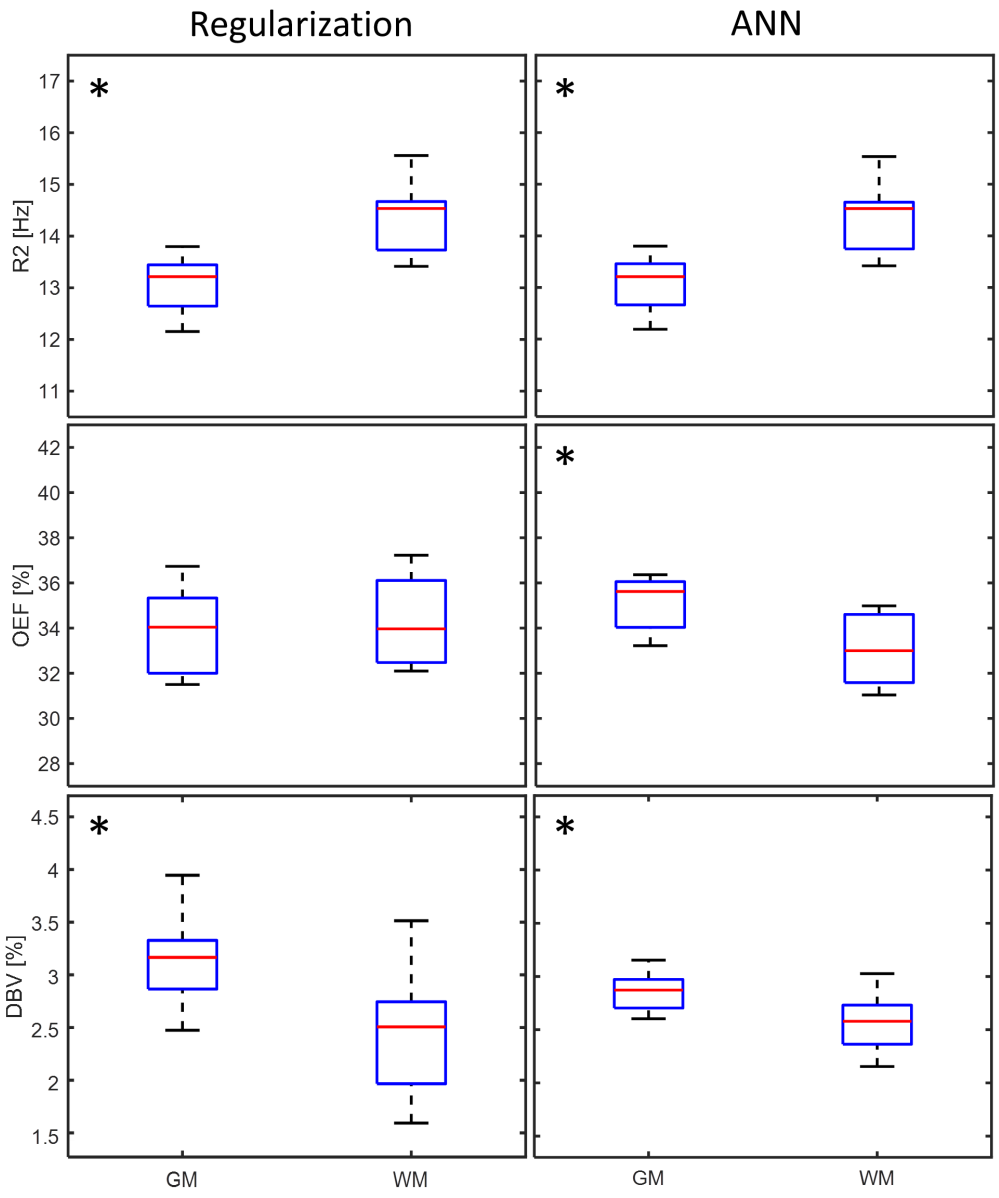

Figure 4.19: Boxplots showing the means in GM and WM of R_2, OEF and DBV for healthy volunteers ($N = 7$) reconstructed with the regularization and ANN method. Significant differences between GM and WM are marked with an asterisk. The box edges delineate the lower and upper quartile and the whiskers 1.5 times the interquartile range; the red line indicates the median.

Table 4.3: Mean and standard deviation of the individual means of smokers ($N = 16$) and never-smokers ($N = 10$) in the whole brain reconstructed with the multi-parametric method.

	pre-smoking	post-smoking	never-smoking
CBF [ml/100 g/min]	37 ± 7	38 ± 6	35 ± 3
OEF [%]	108 ± 14	104 ± 15	116 ± 7
CMRO2 [µmol/100 g/min]	211 ± 33	211 ± 29	212 ± 13
R_2 [Hz]	10.2 ± 0.3	10.2 ± 0.3	10.0 ± 0.2
R_2* [Hz]	21.4 ± 0.8	21.3 ± 0.7	21.4 ± 0.6
DBV [ml/100 g]	4.5 ± 0.4	4.6 ± 0.3	4.4 ± 0.2

No significant difference was found in the whole brain ROI.

4.3.1 *Oxygenation and Perfusion in Smokers*

For the smoker study, a multi-parametric and the GESSE-based ANN evaluation was performed. First, the parameter maps are presented for the multi-parametric method. Second, the results for both methods are compared using boxplots for smokers vs. never-smokers (chronic effects) and for smokers in the pre- vs. post-smoking state (acute effects).

PARAMETER MAPS Figure 4.20 shows representative parameter maps of one smoker reconstructed with the multi-parametric method. Depicted are the relaxation parameters R_2, R_2* and R_2' together with the physiological parameters CBF, DBV, OEF and CMRO2, as well as the corresponding T_2 weighted image as morphological reference. Contrast between gray and white matter can be observed in CBF, OEF and CMRO2. The OEF varies substantially and partly exceeds 100%. Due to apparent artifacts in the R_2* maps, four smokers were excluded from the statistical analysis, which reduces the number of smokers to $N = 16$.

The intersubject means and standard deviations of all parameters in the whole brain for the pre-, post- and never-smoking state are listed in Table 4.3 for the MP method and in Table 4.4 for the ANN method.

ACUTE EFFECTS The acute effects of smoking are depicted in Figure 4.21 as the difference between pre- and post-smoking state for the multi-parameter reconstruction. The results for the ANN reconstruction are shown in Figure 4.22. The ROI for the amygdala was omitted due to insufficient volume coverage of the GESSE sequence.

No significant difference was found comparing the pre- and the post-smoking state for none of the methods.

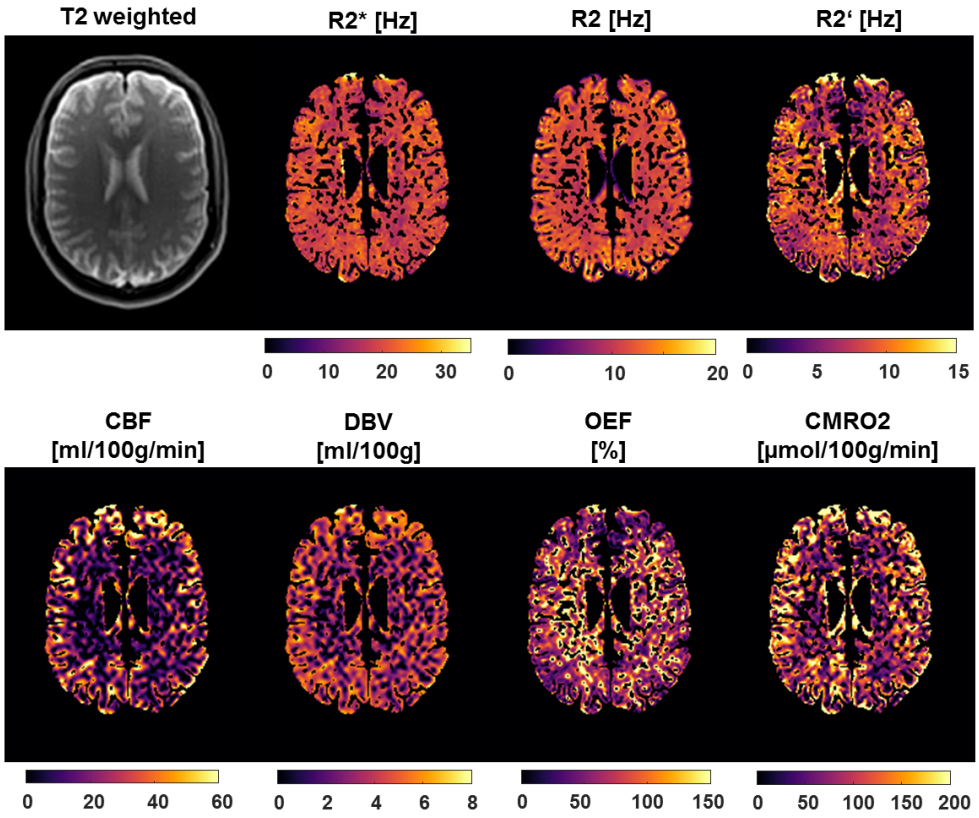

Figure 4.20: Parameter maps and T_2 weighted image of a representative slice (MNI coordinate: $z = 185$) of one smoker (pre-smoking) reconstructed with the multi-parametric method. The parameter maps depict the observed transverse relaxation rate R_2*, irreversible transverse relaxation rate R_2, reversible transverse relaxation rate $R_2' = R_2$* - R_2, CBF, DBV, OEF and CMRO2. A mask of the brain parenchyma without the cerebrospinal fluid was used.

Table 4.4: Mean and standard deviation of the individual means of smokers ($N = 16$) and never-smokers ($N = 10$) in the whole brain reconstructed with the ANN method.

	pre-smoking	post-smoking	never-smoking
CBF [ml/100 g/min]	37 ± 7	38 ± 6	35 ± 3
OEF [%]	35 ± 1	35 ± 1	35 ± 1
CMRO2 [µmol/100 g/min]	98 ± 19	98 ± 13	89 ± 9

No significant difference was found in the whole brain ROI.

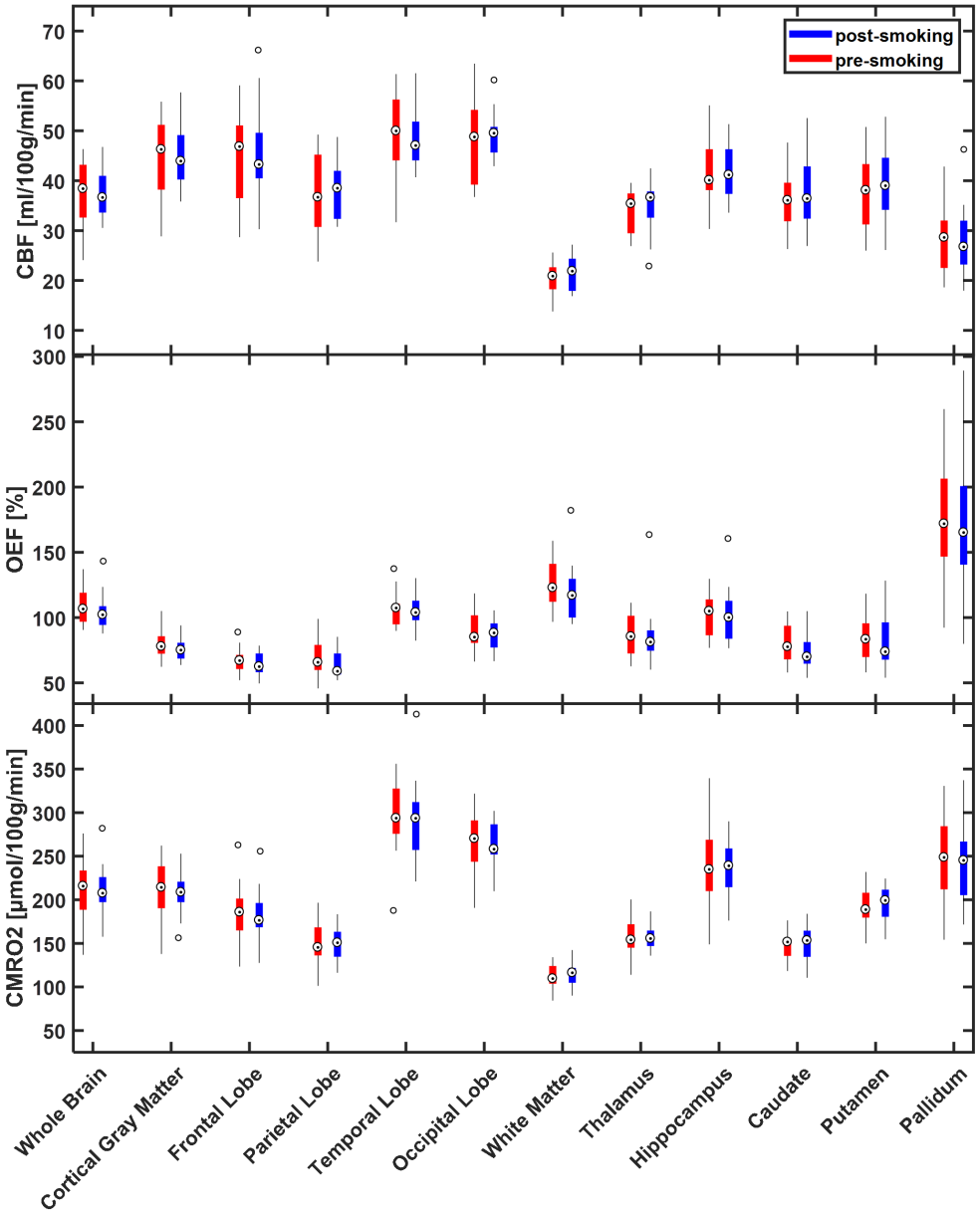

Figure 4.21: Boxplots showing the mean CBF, OEF and $CMRO_2$ in the pre- and post-smoking state for all smokers ($N = 16$) reconstructed with the multi-parameter method. The box edges delineate the lower and upper quartile and the whiskers 1.5 times the interquartile range; the circled dot indicates the median. No significant difference was found.

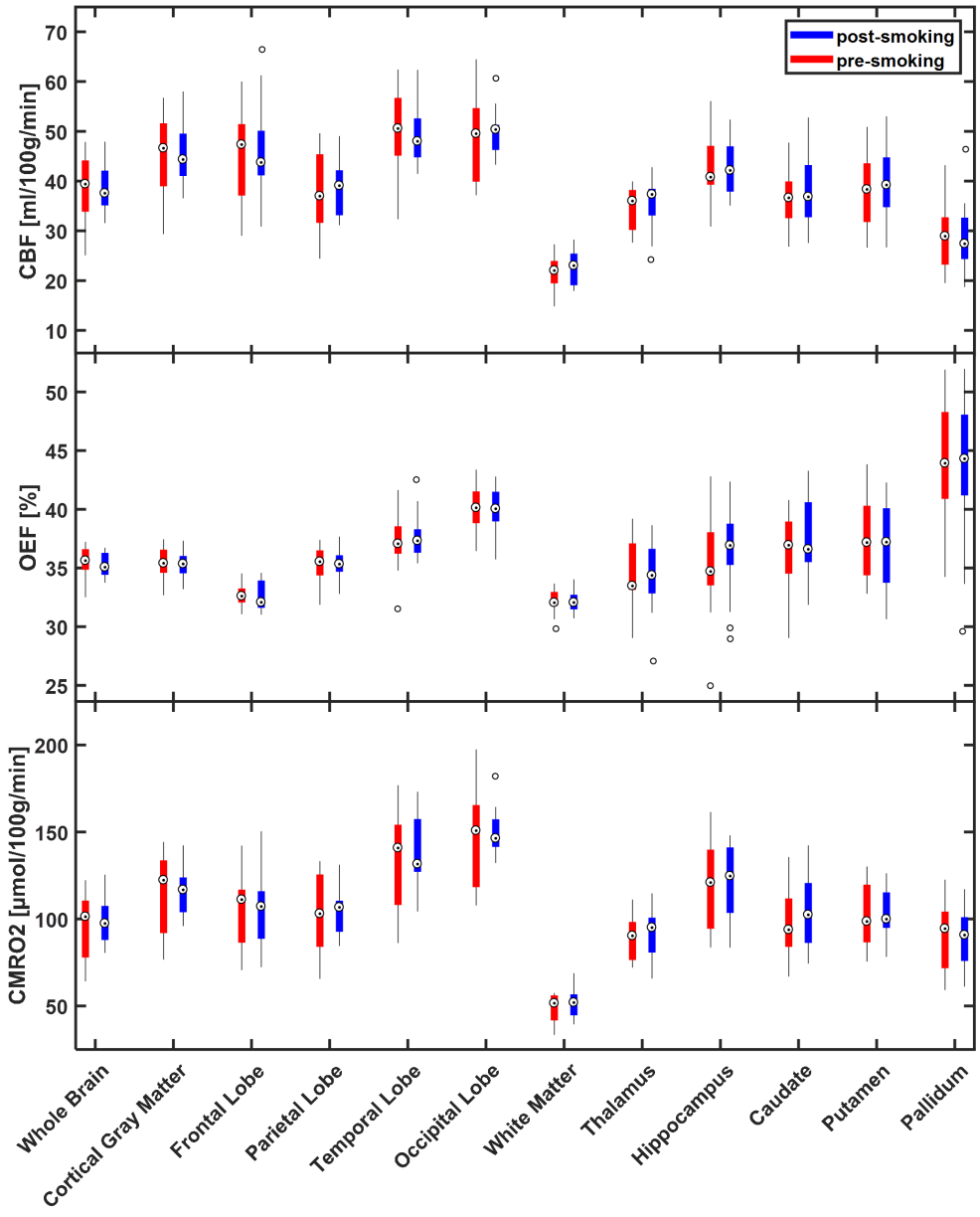

Figure 4.22: Boxplots showing the mean CBF, OEF and $CMRO_2$ in the pre- and post-smoking state for all smokers ($N = 16$) reconstructed with the ANN method. The box edges delineate the lower and upper quartile and the whiskers 1.5 times the interquartile range; the circled dot indicates the median. No significant difference was found.

CHRONIC EFFECTS The chronic effects of smoking are depicted in Figure 4.23 as the comparison of smokers in the pre- and post-smoking state vs. never-smokers. Figure 4.24 shows the corresponding boxplots of smokers (post-smoking) and never-smokers. Significant differences between smokers in the post-smoking state and never-smokers were found for $CMRO_2$ in the putamen for the MP method and for both CBF and $CMRO_2$ in the occipital lobe for the ANN method. In the comparison of smokers in the pre-smoking state with never-smokers, no significant difference was found for none of the methods.

4.3.2 *Oxygenation in Tumor Patients*

Here, the results of 3 patients with brain tumors are presented. The data was evaluated with both the regularization and the ANN method. In Figure 4.25, the parameter maps of R_2, OEF and DBV for the regularization method are shown together with a morphological T_1 weighted image with contrast agent as a reference. In Figure 4.26, the analog results are shown for the ANN method. In the T_1 weighted image, hyperintensities are visible in the regions of increased contrast agent accumulation. This was assumed to be the tumor region. In both figures, the tumor region is marked with a white ROI and mirrored to the healthy contralateral side as comparison (marked green).

The regularization and the ANN results visually show a high conformity. The tumor regions coincide with a region of decreased R_2, which also extends to the surrounding tissue in patient number 2 and 3. In contrast to the overall homogeneous OEF, the values are increased in the tumor ROI. However, strong deviations are visible within the tumor region. In patient number 1, the center of the region has a smaller region with low OEF; whereas, in patient number 3, the tumor region shows a smaller region of highly increased OEF. The DBV values tend to be increased compared to the contralateral side. In patient number 3, large areas of artifacts are visible yielding highly increased DBV.

The tumor ROIs are compared with the ones on the contralateral side using boxplots in Figure 4.27 for the regularization method and in Figure 4.28 for the ANN method. The means and standard deviations of the qBOLD parameters in the tumor and the contralateral ROI are given in Table 4.5 for both methods. Significant differences between tumor and contralateral ROI are found for all cases except for DBV in patient number 3 for the regularized reconstruction. In the ANN reconstruction, all cases show a significant difference.

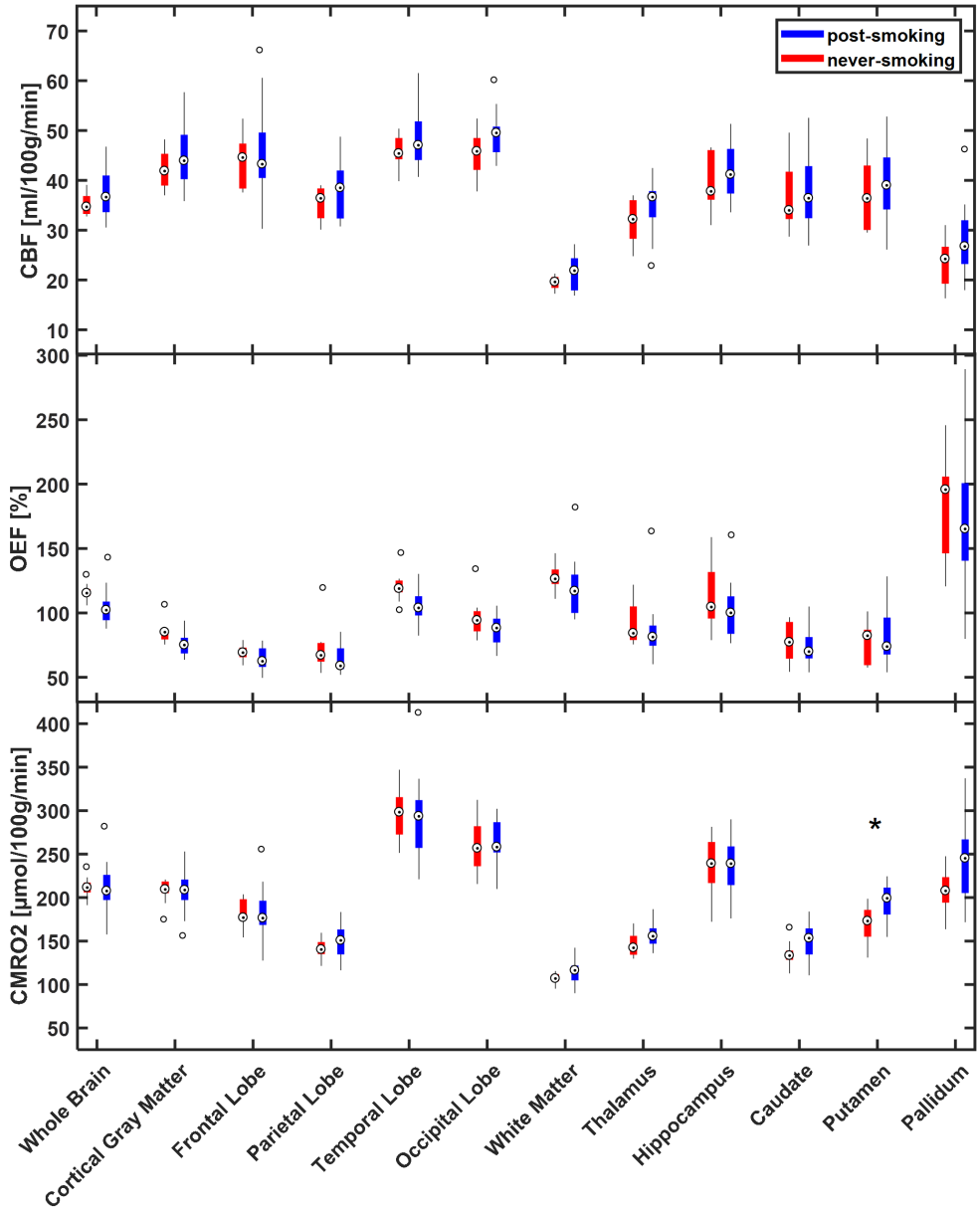

Figure 4.23: Boxplots showing mean CBF, OEF and $CMRO_2$ for post- (blue, $N = 16$) and never-smoking state (red, $N = 10$) reconstructed with the multi-parameter method. Significant differences between smoking states are denoted with asterisks (* $p < 0.01$). The box edges delineate the lower and upper quartile and the whiskers 1.5 times the interquartile range; the circled dot indicates the median. A significant difference was found in the $CMRO_2$ in the putamen.

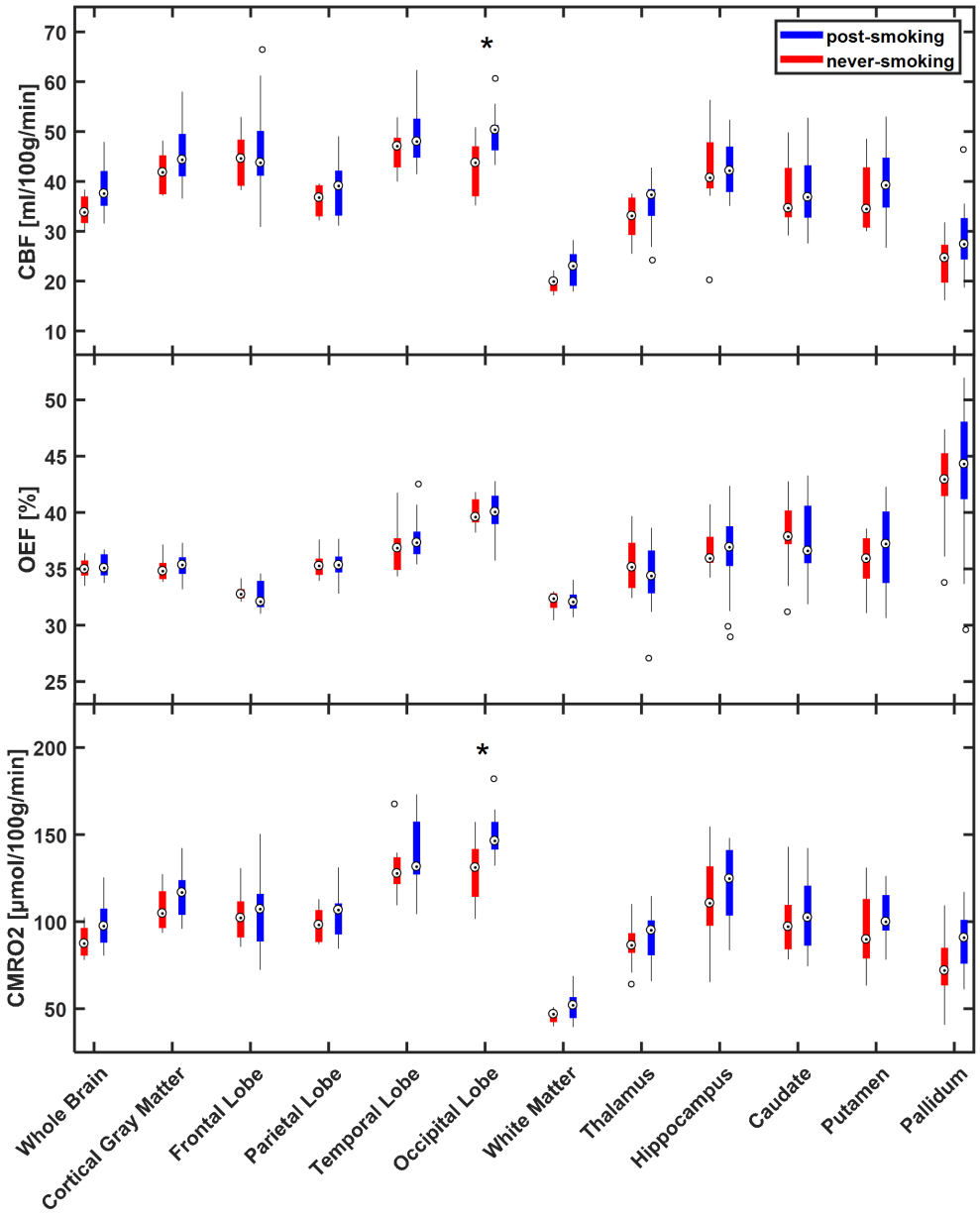

Figure 4.24: Boxplots showing mean CBF, OEF and $CMRO_2$ for post- (blue, $N = 16$) and never-smoking state (red, $N = 10$) reconstructed with the ANN method. Significant differences between smoking states are denoted with asterisks (* $p < 0.01$). The box edges delineate the lower and upper quartile and the whiskers 1.5 times the interquartile range; the circled dot indicates the median. A significant difference was found in both the CBF and $CMRO_2$ in the occipital lobe.

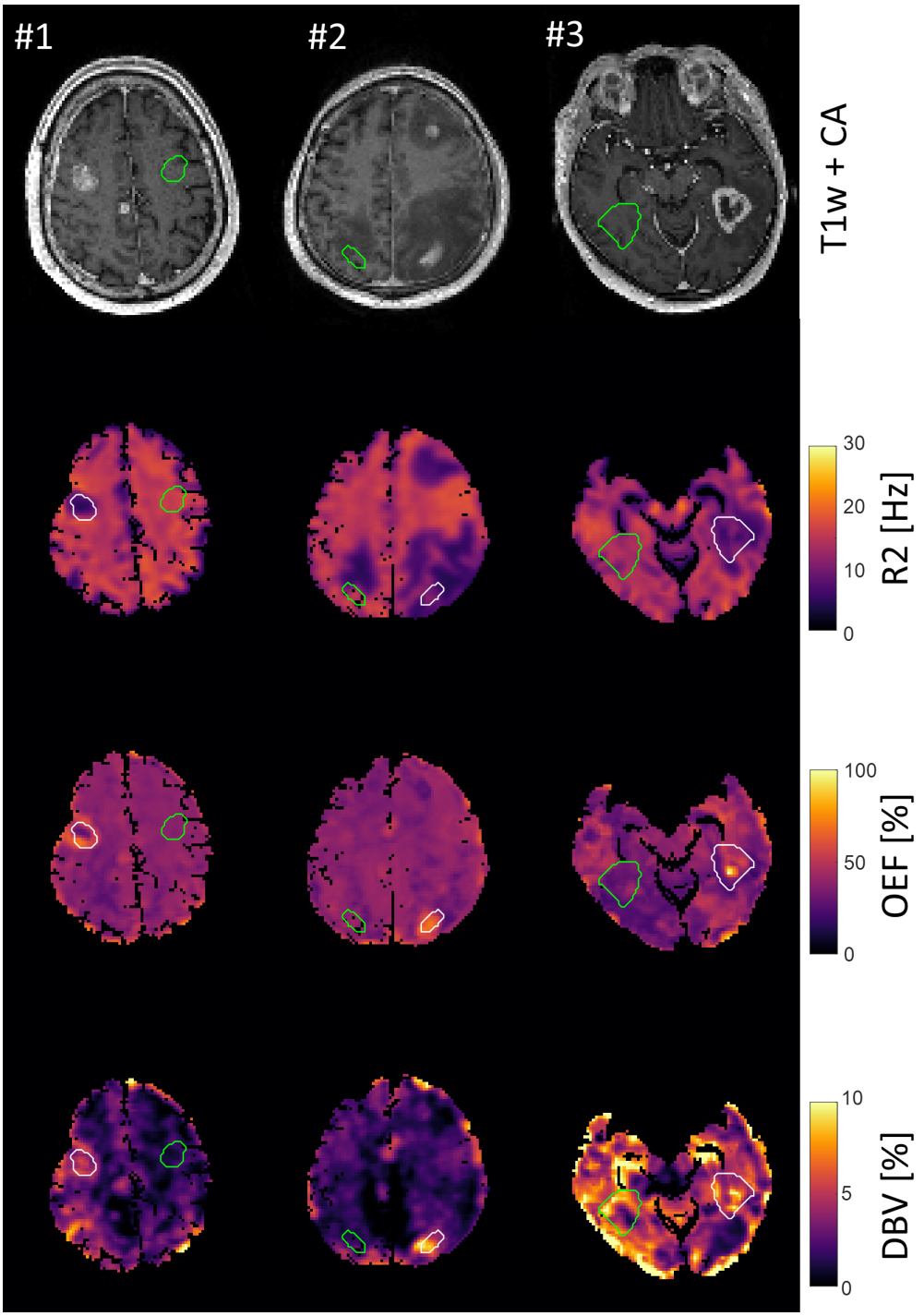

Figure 4.25: ANN reconstruction of three tumor patients. Depicted are the T_1 weighted images with contrast agent and the qBOLD parameters R_2, OEF and DBV (top to bottom). The tumor is marked by a white ROI. As comparison, this ROI was mirrored to the healthy contralateral side and marked green.

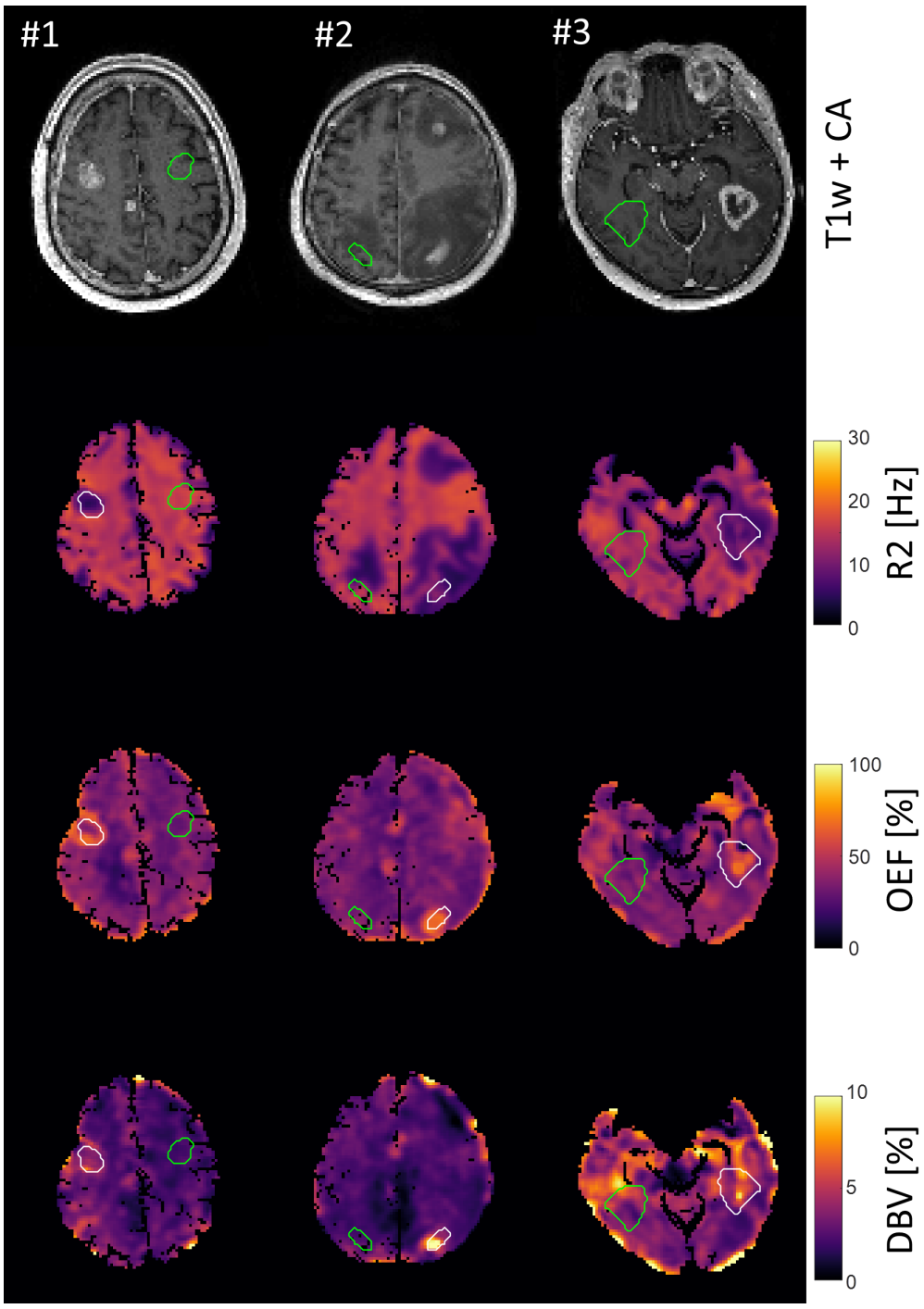

Figure 4.26: Regularized reconstruction of three tumor patients. Depicted are the T_1 weighted images with contrast agent and the qBOLD parameters R_2, OEF and DBV (top to bottom). The tumor is marked by a white ROI. As comparison, this ROI was mirrored to the healthy contralateral side and marked green.

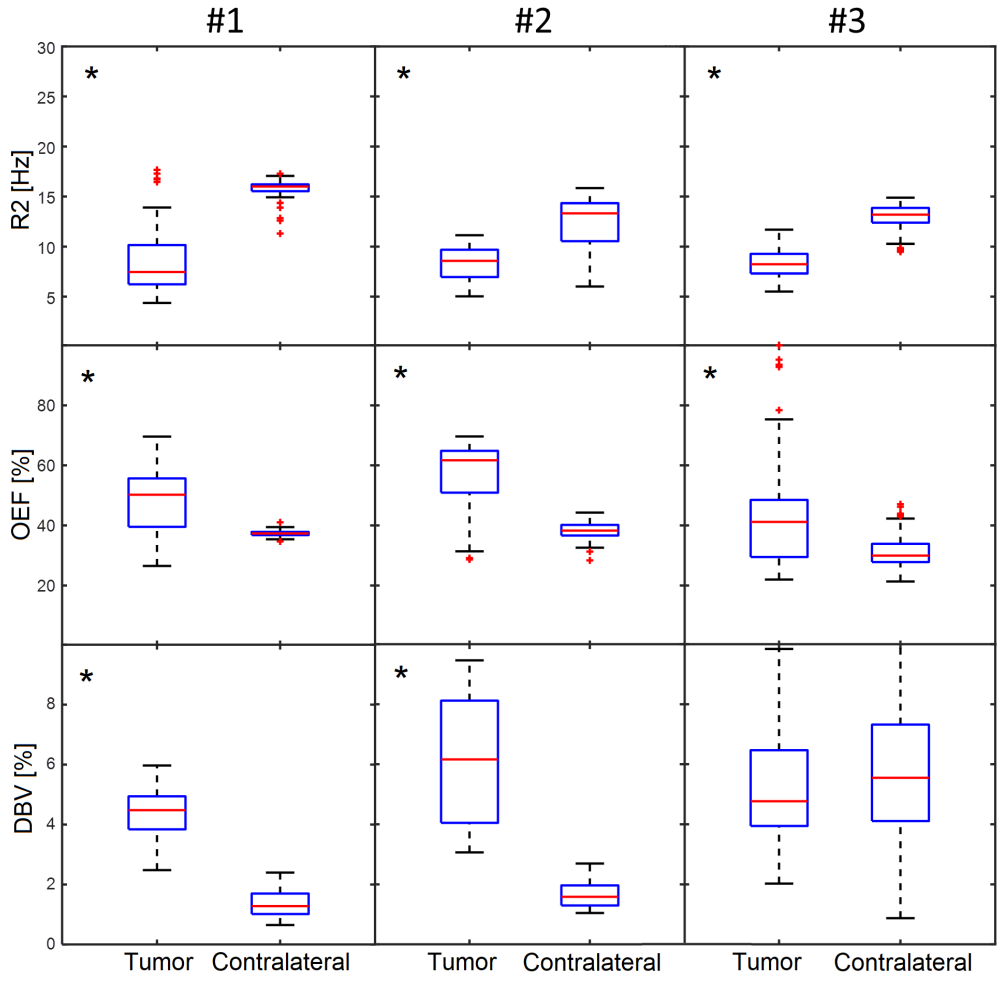

Figure 4.27: Boxplots showing the qBOLD parameters R_2, OEF and DBV (top to bottom) reconstructed with the regularization method within the tumor ROI and the contralateral side for three patients.

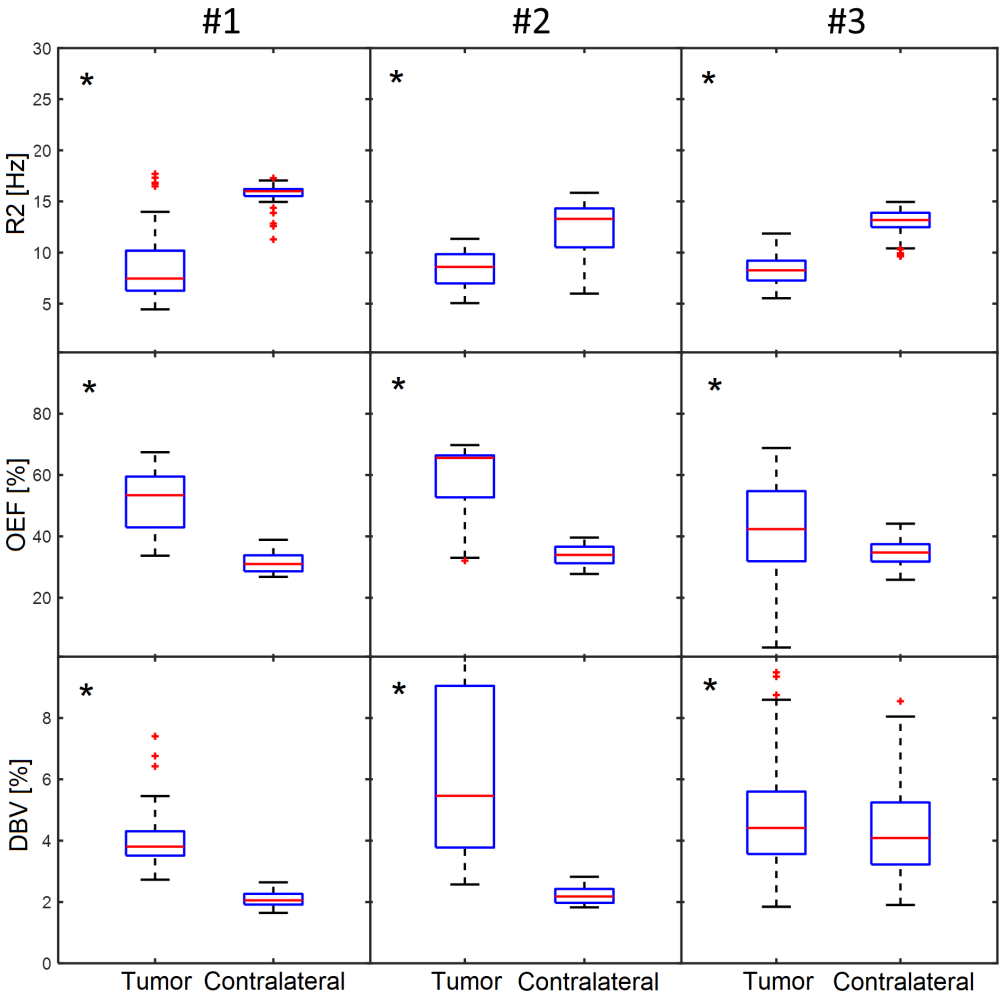

Figure 4.28: Boxplots showing the qBOLD parameters R_2, OEF and DBV (top to bottom) reconstructed with the ANN method within the tumor ROI and the contralateral side for three patients.

Table 4.5: Mean and standard deviation of the qBOLD parameters R_2, OEF and DBV of three tumor patients reconstructed with the regularization and the ANN method. Results are shown within the tumor region and the contralateral side.

		#1	#2	#3
Regularization				
R_2 [Hz]	Tumor	$8.6 \pm 3.4^{\dagger}$	$8.3 \pm 1.7^{\dagger}$	$8.3 \pm 1.4^{\dagger}$
	Contra	15.8 ± 1.0	12.3 ± 2.7	13.0 ± 1.3
OEF [%]	Tumor	$48.8 \pm 11.8^{\dagger}$	$56.7 \pm 12.1^{\dagger}$	$41.2 \pm 14.7^{\dagger}$
	Contra	37.4 ± 1.0	38.0 ± 3.1	31.1 ± 5.2
DBV [%]	Tumor	$4.4 \pm 0.8^{\dagger}$	$6.1 \pm 2.1^{\dagger}$	5.3 ± 1.8
	Contra	1.4 ± 0.5	1.7 ± 0.5	5.7 ± 2.3
ANN				
R_2 [Hz]	Tumor	$8.6 \pm 3.4^{\dagger}$	$8.4 \pm 1.8^{\dagger}$	$8.3 \pm 1.4^{\dagger}$
	Contra	15.8 ± 1.0	12.3 ± 2.7	13.0 ± 1.3
OEF [%]	Tumor	$51.7 \pm 9.8^{\dagger}$	$59.2 \pm 11.4^{\dagger}$	$42.7 \pm 14.5^{\dagger}$
	Contra	31.4 ± 3.3	33.9 ± 3.2	34.8 ± 4.2
DBV [%]	Tumor	$4.0 \pm 0.9^{\dagger}$	$6.2 \pm 2.8^{\dagger}$	$4.7 \pm 1.6^{\dagger}$
	Contra	2.1 ± 0.3	2.2 ± 0.3	4.2 ± 1.4

† denotes a significant difference between tumor and contralateral ROI.

5 DISCUSSION

In this thesis, different methods of mapping the brain oxygenation using the quantitative Blood Oxygen Level Dependent method were examined. Starting from the multiparametric and the Gradient Echo Sampled Spin Echo-based Least Squares method, prior information was added to the fit via a regularization term. Secondly, an Artificial Neural Network was trained with simulated GESSE data to reconstruct the Oxygen Extraction Fraction from measured data in a faster and potentially more robust way. These methods were applied in a smoker study to examine the influence of cigarette smoking on brain metabolism. It was discriminated between short and long term effects, i. e. differences between smokers and the control group of never-smokers and differences among smokers before and after smoking one cigarette. Finally, the methods were applied to a group of tumor patients to examine the oxygenation difference of tumor tissue compared to healthy tissue on the contralateral side.

PROTOCOL OPTIMIZATION First, the measurement protocol of the GESSE sequence needed to be optimized in order to fulfill the requirements of a clinical setting. The measurement time was limited to 10 minutes and the number of acquired slices needed to be sufficient to cover most of the brain. The TR of 2778 ms was set to be long compared to typical T_1 times of brain tissue in order to minimize T_1 weighting. This yielded the additional advantage that within the course of one TR several slices could be acquired before the next excitation took place. The slices were measured in an interleaved manner to reduce the crosstalk between neighboring slices. According to the Ernst angle adjusted for spin echo-based sequences, the optimal flip angle was found to be almost 90° for the chosen TR and typical T_1 of the brain. This allowed the acquisition of three averages within the scan time of 10 minutes yielding an additional SNR improvement.

5.1 STANDARD QBOLD RECONSTRUCTION

First, the status quo of the qBOLD method was analyzed. The inherent problems of LS and MP were examined and are discussed in the following. The results led to the development of the novel, more robust reconstruction techniques using the regularization and the ANN method.

5.1.1 *Least Squares Reconstruction*

The LS reconstruction of the GESSE-based qBOLD method was demonstrated on a representative healthy volunteer. The found R_2 values of (13.2 ± 1.5) Hz in

GM and (14.6 ± 1.1) Hz in WM are both in good agreement with the expected values of 11.5 Hz and 13.0 Hz in GM and WM, respectively [Whittall et al., 1997; Yablonskiy et al., 2013]. However, there is a bias of approximately 1.5 Hz for both regions. For a more accurate representation of the R_2 effects within the tissue, the multicompartment model needs to be utilized [He et al., 2008]. This takes into account the multiple components of the R_2 decay originating from individual structures, such as myelin in WM.

In contrast to the accurate reconstruction of R_2, the reconstructed values of OEF and DBV lie above the physiologically expected range. In case of the OEF, some voxels are above the physically reasonable value of 100%. The high sensitivity to noise in the acquired data dominates the fit and makes the parameters OEF and DBV diverge out of their reasonable range. It is apparent that regions of very high OEF coincide with regions of very low DBV. This indicates a strong interdependence of these two parameters in the reconstruction. Due to signal noise the effect on the qBOLD model cannot be attributed correctly to the respective parameter.

5.1.2 *Multiparameter Reconstruction*

In addition to the LS method, the MP approach was demonstrated in vivo on a healthy volunteer. The R_2 values of (10.4 ± 2.4) Hz in GM and (12.4 ± 1.8) Hz in WM are both slightly lower than expected; however, still in good agreement with the literature [Whittall et al., 1997; Yablonskiy et al., 2013]. The mean CBF reconstructed from the ASL data in WM is quite accurate compared to the expected value of 20 ml/100 g/min. In GM, CSF is lower than the expected 60 ml/100 g/min [Günther et al., 2005]. However, the relative standard deviation within the subject is quite high with almost 50% in GM. Both the bias and the strong variation propagate into the OEF and $CMRO_2$ maps calculated from R_2' and CBF. This is visible in regions of exceedingly high OEF above 100% as well as in overestimated regions in $CMRO_2$, which is expected to be $120 - 180$ µmol/100 g/min in GM and $40 - 80$ µmol/100 g/min in WM [Leenders et al., 1990; Ito et al., 2004].

The inability of both the LS and the MP approach to accurately estimate the oxygenation parameters demonstrates the need for more robust reconstruction methods.

5.2 NOVEL QBOLD RECONSTRUCTION

5.2.1 *Regularization*

As seen in the LS method, the interdependence of OEF and DBV can easily lead to an underestimation of one parameter and a corresponding overestimation of the other. As shown by Sedlacik and Reichenbach [2010]; Christen et al. [2012b, 2013], if one parameter is set to a fixed value in the physiological range, the other one can be properly estimated. However, a constant value does not allow for variations and, accordingly, leads to poor data fidelity if

the predetermined parameter is not measured by other means. As a compromise between the fixation of one parameter and the free variation of both in the LS approach, a regularization approach was introduced. The goal of the regularization was to suppresses the influence of noise on the estimated OEF and DBV and let the estimates converge in a physiological range.

The strength of the regularization term was adjusted by a weighting factor in the minimization cost function. An increase of the weighting factor led to an increased precision, since the parameter variance was influenced less by noise. However, the smoothing effect also reduced the structural information of the measured tissue. Furthermore, the parameter estimates increasingly converged towards the prior for an increased weighting factor. This potentially led to an increased bias for larger weighting factors.

In order to find the best compromise of the weighting factor, an L-curve analysis was performed. The factor that led to the highest curvature in the in vivo data was chosen for all further studies. With this weighting factor, the regularization yielded a good trade-off between reasonable parameter estimates and data fidelity. The regularized approach with optimized weighting factor showed a homogeneous OEF distribution in healthy brain tissue, which is in agreement with the findings of PET studies [Raichle et al., 2001]. The heavy artifacts present in the LS approach were suppressed. As visible in the difference between GM and WM in the DBV map, structural information of the tissue was preserved by the reconstruction.

SIMULATED PATHOLOGY The influence of different weighting factors of the regularization term on the estimated OEF was analyzed for a map comprising a baseline level (40%) and a region of increased OEF (80%) to mimic a pathology with increased oxygen demand. Here, the emphasis lay on the ability to recognize a contrast in OEF between the baseline and the pathology. Due to the penalty for solutions that deviate from the prior, hotspots experienced a bias from their true value, which led to a decreased accuracy for higher weightings. For moderate weighting, a trade-off between noise-suppression and data-fidelity led to a distinct contrast between hotspot and baseline and thus to an advantage of the regularization approach over conventional LS regression with its huge variance. Remarkably, the range of this enhanced contrast spans over approximately three orders of magnitude, which makes it robust against an imperfect choice of weighting.

5.2.2 *Artificial Neural Network*

On the basis of the initially proposed ANN by Domsch et al. [2018], a fast and more robust ANN method was developed. First, the input data were normalized to the signal at SE, termed S_0. This parameter is merely a scaling factor related to the signal magnitude in arbitrary units and contains no physiological information about the oxygenation. The normalization yields the advantage of a reduced number of free parameters, which makes the training process more efficient. Second, the parameter distribution of the training

set was adjusted to better reflect in vivo conditions. In previous implementation, the training parameters were uniformly distributed. Instead, a more physiological Gaussian distribution was implemented here.

The ANN was applied to a healthy volunteer as well as simulated data in order to demonstrate its feasibility. In the healthy volunteer, the reconstructed R_2 values were in accordance with the LS and regularization approach. Similarly, a bias in the mean value of approximately 1.5 Hz was found for both GM and WM. The OEF in both GM and WM is in the expected range of $30-45\%$ and in good agreement with the literature [Carpenter et al., 1991; Diringer et al., 2000; Ito et al., 2004; Bulte et al., 2012; Gauthier and Hoge, 2012; Wise et al., 2013]. DBV in GM and WM is in good agreement with the literature; however, GM is on the lower end of the expected range [An and Lin, 2002a,b; Bulte et al., 2007].

The simulation yields comparable results. The SD is significantly lower than in the in vivo data, which is plausible since potential imaging artifacts and inhomogeneities are not incorporated in the simulation.

SENSITIVITY ANALYSIS In the next step, several parameters of the ANN were varied and the influence on the parameter reconstruction were analyzed. The change from the uniform training distribution to the Gaussian distribution yielded an improvement in both accuracy and precision. It suggests that the reconstruction was improved by the more realistic representation in the training data. The change from one Gaussian distribution to two separate distributions for GM and WM, however, did not improve the results significantly. The number of nodes within the hidden layer of the ANN did not have a significant effect on the reconstructed parameters. Since the size of the hidden layer determines the complexity of the network, this indicates that the complexity was sufficient for the given task. A more complex network is required for more advanced reconstruction problems as can be seen by the large number of nodes and layers used in deep learning for other medical image processing tasks [Maier et al., 2019]. An increase of the training set size led to a better performance in GM and WM both in accuracy and precision. It could be expected that a larger training set contains more information for the network to learn from. An upper limit is set by the required memory space and the computing time. However, since the network only has to be trained once, this is no big drawback for the clinical application. An increase in training SNR led to an increase in the reconstruction SD. If the training SNR was to high compared to the SNR of the data, the network did not learn to recognize noise in the data. Therefore, it tended to attribute noise to a change in the reconstruction parameters. If the training SNR was too small, the network failed to learn the effect of the parameters and the reconstructed distribution became artificially narrow with the parameters being mostly set to the mean value. Best results could be reached by choosing the training SNR comparable to the expected in vivo SNR.

In the scenario of varied SNR of the ground truth data, all three trained ANNs showed accurate parameter estimation over a wide SNR range. The pre-

cision increased with the ground truth SNR in all cases. For R_2, the influence of the training SNR was negligible. For OEF and DBV, lower training SNR led to a higher precision. This again indicates that the ANN attributed noise to parameter changes at lower SNR. Training with an SNR of 100 leads to the best trade-off for OEF estimation for all tested SNR values. It yielded the highest accuracy as well as a SD below 10% for an input SNR of 100 corresponding to in vivo data. In case of variation of the ground truth itself, R_2 could always be robustly fitted. However, OEF and DBV showed a strong coupling, which makes independent fitting of these two parameters difficult. Similar issues have been found previously using standard qBOLD techniques [Sedlacik and Reichenbach, 2010]. The fact that the reconstructed parameters tend to lie within a reasonable range suggests that the ANN introduces a regularization effect on the reconstructed parameters. It might arise due to the training in a limited parameter range. This may offer the possibility to adjust the regularization effect of the ANN by changing the training set.

5.2.3 *Healthy Volunteers*

The LS, regularization and ANN method were applied to GESSE data of a group of healthy volunteers. R_2 results of all three methods agreed very well with each other in both GM and WM. The OEF maps of the regularization and ANN method both did not exhibit the strong artifacts that were present in the LS reconstruction. Both methods yielded an OEF well within the physiological range of $30 - 45\%$ given in the literature [Leenders et al., 1990; Carpenter et al., 1991; Diringer et al., 2000; Bolar et al., 2011; Bulte et al., 2012]. Additionally, the narrow parameter distribution is in accordance to the homogeneous maps found in PET measurements [Gusnard and Raichle, 2001]. A slight underestimation of the OEF might arise from neglecting diffusion effects in the qBOLD model as reported by Dickson et al. [2010]. Similar results were found in the DBV maps, in which most of the artifacts were suppressed in the regularization and ANN method. In the regularization map, some regions of unphysiological DBV values were left. The SD was higher in the regularization method compared to the more homogeneous ANN results. However, the regularization expected contrast between GM and WM was more pronounced in the regularization method.

5.3 IN VIVO STUDIES

5.3.1 *Oxygenation and Perfusion in Smokers*

In the smoker study, an MRI-based ASL and multiparametric qBOLD method were applied in never-smokers and smokers, the latter undergoing an acute cigarette smoking challenge. Additionally, GESSE images were acquired and reconstructed with the ANN approach. To the best of our knowledge, this is the first time that the acute and chronic effects of smoking on brain oxygenation and perfusion have been examined with MRI.

Previous PET studies have produced conflicting evidence concerning the changes in brain metabolism caused by acute and chronic smoking in human smokers. One possible explanation for the differential results may be the broad scope of physiological effects cigarette smoke has on the body [Talhout et al., 2011]. A study investigating cerebrovascular changes in rats after nicotine administration revealed an interesting biphasic vascular response [Iida et al., 1998]. Iida et al. found that initial vasoconstriction was followed by vasodilation, with the vasodilatory effects subsiding with repeated nicotine exposure across time. This suggests that the precise time point at which cerebrovascular changes are measured and whether administration is acute or chronic might influence results. Beyond time, location is also a crucial factor. It appears that instead of homogeneously either increasing or decreasing CBF, cigarette smoking induces a redistribution of blood flow, increasing blood flow to certain regions, such as the visual cortex and cerebellum, while decreasing blood flow to other areas, in particular those associated with drug craving and reinforcement [Zubieta et al., 2005].

In general, it has been suggested that chronic cigarette smoking reduces global CBF mainly by impairing a central mechanism for cerebral vasodilation [Toda and Okamura, 2016]. On the other hand, acute nicotine exposure appears to both transiently increase and decrease CBF and energy metabolism, depending on smoking status and brain region. An increase is observed especially in regions, such as the thalamus and visual cortex [Uchida et al., 2009]. Taken together, these findings support a view in which chronic, repeated nicotine administration reduces both baseline brain metabolism, as well as cerebral vascular reactivity to nicotine, while the effects of acute nicotine exposure are more variable, especially with respect to regional differences.

Firstly, in this study, pre- and post-smoking states across three physiological parameters of brain metabolism – CBF, $CMRO_2$, and OEF – were contrasted in order to assess possible acute effects of cigarette smoking. CBF did not change significantly, which is in agreement with previous work by Shinohara et al. [2006]. However, it contradicts other studies, in which increased CBF was found after smoking [Skinhoj et al., 1973; Vafaee et al., 2015; Yamamoto et al., 2003]. In our case, the CBF in all smoking states was lower than the values measured in other studies, for example, by Vafaee et al. in gray matter. Similarly, no significant difference was detected in $CMRO_2$, which supports Skinhoj et al. [1973], but stands in opposition to Vafaee et al. [2015]. Also, no significant difference was found in the OEF following cigarette smoking, for which, to our knowledge, no previous results exist in the literature. Despite the fact that the absolute values of the reconstructed parameters were much more realistic in case of the ANN reconstruction, both methods came to the same results of no significant change for all three parameters.

Secondly, smokers were compared to never-smokers to identify any potential effects of chronic smoking on brain metabolism. The multiparametric reconstruction yielded no significant difference in CBF for the post-smoking group when compared to never-smokers. The same goes for the comparison of the pre-smoking group with the never-smokers. These results con-

flict with Yamamoto et al. [2003], who found a decrease comparing post-smoking to never-smokers. Vafaee et al. [2015] reported a decrease in the pre-smoking state compared to never-smokers in global gray matter, which then normalized in the post-smoking state over time. With the ANN reconstruction, however, a significant increase was found in the occipital lobe for the post-smoking group compared to the never-smokers. $CMRO_2$ has previously been found to decrease first and then normalize after smoking in global gray matter [Vafaee et al., 2015]. Our results yielded a significant $CMRO_2$ decrease for never-smokers in the putamen when compared to post-smoking state reconstructed with the multiparameter method and a decrease in the occipital lobe reconstructed with the ANN method. Otherwise, we found no significant differences. Interestingly, a region of the brain specifically involved in addiction circuitries, the putamen, seems to be more active in smokers than in never-smokers. This is in line with work by Akkermans et al., which showed that resting state functional connectivity between the putamen and insula is stronger in smokers than in non-smokers [Akkermans et al., 2018]. Finally, OEF resulted in no significant difference for all parameters, brain regions and reconstruction methods.

It must be noted that some of the model assumptions used for the qBOLD approach may not be fulfilled. In particular the arterial oxygen saturation is commonly assumed to be 98%; however, this may not be the case for chronic smokers. This could be overcome by measuring the arterial oxygen saturation directly in future studies.

The multiparameter approach implemented here involves a drawback compared to the GESSE-based method because three separate measurements are combined. Biases of the individual measurements or the registration process could propagate into the final parameter maps. The measured OEF is significantly higher than physiologically expected and partly exceeds 100%. This is a known issue in multiparametric qBOLD measurements [Hirsch et al., 2014]; yet, it does not pose a problem for the relative comparison of two groups. However, this further encourages the use of the ANN method.

The mean CBF in cortical gray matter of all smoking states lies within the range of $40 - 100\,\mathrm{ml}/\,100\,\mathrm{g}/\,\mathrm{min}$ given in the literature [Alsop et al., 2015], however, at the lower limit. This might indicate an underestimated perfusion caused by imperfect labeling [Alsop et al., 2015] and varying arrival times of the inflowing blood [Bokkers et al., 2012]. Possible biases in the CBF might propagate indirectly to the OEF via the DBV and directly to the $CMRO_2$. These issues could be overcome by more advanced ASL techniques [von Samson-Himmelstjerna et al., 2016].

The mean $CMRO_2$ exceeds the physiological range of $120 - 180\,\mu\mathrm{mol}/\,100\,\mathrm{g}/\,\mathrm{min}$ [Bolar et al., 2011; Leenders et al., 1990; Zhang et al., 2015], which might be due to the overestimation of the OEF. It is difficult to determine the sensitivity of the method proposed here without the direct comparison to a gold standard such as PET. The high standard deviation of the measured physiological parameters could dominate small changes linked to the smoking state.

The methods implemented here form the basis for more extensive studies on the effects of cigarette smoking. This will help in obtaining a deeper understanding and, hopefully, an eventual scientific consensus on the acute and chronic effects of smoking on brain oxygenation and perfusion. If future studies confirm that the acute effects of smoking have little to no influence on the oxygenation metabolism of the brain, this fact would also have a significant impact on fMRI studies in smokers. Brain activations found in such studies could then be solely attributed to pharmacological or psychological effects rather than being caused by oxygenation or perfusion.

5.3.2 *Oxygenation in Tumor Patients*

In this study, a group of three tumor patients were examined with the GESSE sequence and parameter maps were reconstructed with both the regularization and the ANN method. The parameters within the tumor ROI and the contralateral side were compared. For R_2, a significant decrease was found in the tumor for all three patients. The edema present in the vicinity of the tumor slows down the T_2 relaxation. The OEF is significantly increased in the tumor region compared to the contralateral side for all three patients. Despite the fact that tumor tissue is highly aggressive, which goes along with an increased metabolism, one would expect a decreased OEF according to the Warburg effect. The increase found here might be due to the tumor being in a phase with aerobic metabolism, in which more oxygen is consumed compared to healthy tissue. Another explanation could be that the qBOLD model falsely allocated other effects to changes in the OEF. The model takes into account a physiological distributions of blood vessels in homogeneous tissue, but does not include any pathologies or otherwise altered tissue. For DBV, again a significant increase was found for the tumor ROI for all three patients with the regularization method. The ANN method only found a significance in the first two patients. An increased DBV is plausible due to the increased vascularization in tumor tissue, which increases the general blood volume.

The qBOLD approach in general entails some inherent limitations. It is important to note that in deep gray matter, iron depositions could potentially influence the MR signal [Zheng et al., 2013] and, thus, might be interpreted as physiological effects. Similarly, the results in cortical gray matter could be affected by air tissue interfaces. A possible solution is the use of more advanced approaches, such as the Quantitative Susceptibility Mapping (QSM) + qBOLD model, which allow for a more precise separation of the aforementioned effects [Cho et al., 2018; Feng et al., 2018; Hubertus et al., 2019a,b].

Similarly, white matter poses a challenge when using the approach presented here due to its anisotropic nature and myelin compartment [Bouvier et al., 2013; Ulrich and Yablonskiy, 2016]. In future studies, more advanced MR-based techniques could be utilized, such as multicompartment qBOLD [He and Yablonskiy, 2007]. Furthermore, CBF measurements in white matter with ASL are difficult, as well, due to the low perfusion and, hence, low SNR. This might lead to an underestimated DBV and, thus, to an overestimation in OEF.

These effects could be responsible for the unexpected contrast between gray and white matter in the OEF maps.

Nonetheless, the MRI-based methods to measure brain oxygenation and perfusion as implemented here open the way for a future clinical application. After a successful validation, the methods represent a readily available and easily accessible alternative to the gold standard ^{15}O PET that allow for a higher resolution and do not require ionizing radiation.

6 CONCLUSION AND OUTLOOK

Measuring the oxygenation in the brain is highly valuable for the diagnosis and treatment planning of various diseases. The MRI-based approach for oxygenation mapping yields huge advantages compared to the gold standard ^{15}O PET because of the lack of ionizing radiation and the wide availability of MRI scanners. However, the qBOLD method is still not ready for the application under clinical conditions.

The aim of this thesis was to transfer this method into clinical applicability. The main obstacle that needed to be overcome was the high sensitivity to noise of qBOLD that prevented the use in a clinically acceptable scan time. To tackle this, a more robust reconstruction method needed to be developed. In this thesis, two novel approaches, namely the regularization and the ANN method, were implemented and optimized.

The regularization method incorporated prior information into the reconstruction in order to encourage a convergence in a physiological range. This method yielded homogeneous OEF maps in healthy tissue in accordance with the literature. The precision of the parameter reconstruction could be improved compared to the standard method. Via an L-curve analysis, the influence of the regularization term was adjusted in order to identify the best trade-off between noise suppression and data fidelity.

The ANN method used simulated data to learn the OEF reconstruction. The method was improved by normalizing the input data to the signal at the spin echo. This way, the data could be used more efficiently for the physiological parameters. Additionally, a Gaussian distribution was implemented into the training data set to better fit the in vivo conditions. Variations in the hidden layer size did not have a significant influence on the parameter reconstruction. This suggests that the network architecture is sufficiently complex for the reconstruction problem. A larger training set improved the reconstruction quality in both accuracy and precision. An increased training SNR led to a higher standard deviation. This shows that the training SNR should be chosen to match the in vivo data in order to prevent overfitting. It could be shown that the reconstructed OEF was well within the expected range and in good agreement with the literature.

Through the incorporation of prior information in the regularization approach and the optimization of the training data in the ANN approach, the qBOLD method was now robust enough to be applied under clinical conditions. Therefore, two in vivo studies have now been conducted.

In the smoker study, both the acute and chronic effects of cigarette smoking on the brain metabolism were examined. So far, PET studies have reported contradictory results about increased, decreased or unchanged oxygen consumption. In this study, the OEF did not show significant differences both

before and after smoking a cigarette and in comparison with never-smokers. In contrast to former PET studies, this work has opened the way for further in-depth MRI studies on a larger scale in order to reach a consensus on the acute and chronic effects of smoking.

In the tumor study, a group of brain tumor patients was examined and the OEF within the tumor tissue was compared to the contralateral side of the brain. The study found a significantly increased OEF in the tumor region compared to healthy tissue illustrating the vast importance of measuring the OEF for tumor assessment. For a final validation, a study with a larger patient cohort should be carried out as well as a direct comparison to ^{15}O PET measurements should be drawn. Subsequently, the improved and validated qBOLD technique could be readily implemented into clinical diagnosis and treatment planning.

In future implementations, the regularization method could be further improved by introducing a more complex model of the vascular network [He and Yablonskiy, 2007]. If larger cohorts of patients are examined, these in vivo data could be incorporated into the ANN training. This could greatly benefit the training process and correspondingly improve the accuracy of the OEF reconstruction even further.

In summary, the MRI-based qBOLD approach could be significantly improved by using the regularization and the ANN method. Both methods show the ability to reconstruct the OEF under clinical conditions and have the potential to finally bring qBOLD into the clinical routine.

A

APPENDIX

A.1 PUBLICATIONS

Below, a list of the peer-reviewed journal articles and conference contributions is given that were written in the course of this doctorate.

Peer-Reviewed Journal Articles

Hubertus, S., **Thomas, S.**, Cho, J., Zhang, S., Wang, Y., and Schad, L. R. (2019b). Comparison of gradient echo and gradient echo sampling of spin echo sequence for the quantification of the oxygen extraction fraction from a combined quantitative susceptibility mapping and quantitative BOLD (QSM + qBOLD) approach. *Magnetic Resonance in Medicine*, https://doi.org/10.1002/mrm.27804.

Hubertus, S., **Thomas, S.**, Cho, J., Zhang, S., Wang, Y., and Schad, L. R. (2019c). Using an artificial neural network for fast mapping of the oxygen extraction fraction with combined QSM and quantitative BOLD. *Magnetic Resonance in Medicine*, https://doi.org/10.1002/mrm.27882.

Conference Contributions

Thomas, S., Hubertus, S., Lee, A., Vollstädt-Klein, S., and Schad, L. R. (2020). Chronic effects of smoking on the brain oxygenation and perfusion using ASL and quantitative BOLD MRI. In *Proceedings of International Society for Magnetic Resonance in Medicine*, volume 28, page 2035. Virtual Meeting

Hubertus, S., **Thomas, S.**, Cho, J., Zhang, S., Wang, Y., and Schad, L. R. (2020). Using an Artificial Neural Network for Fast Mapping of the Oxygen Extraction Fraction with Combined QSM and qBOLD. In *Proceedings of International Society for Magnetic Resonance in Medicine*, volume 28, page 1867. Virtual Meeting

Thomas, S., Hubertus, S., Skampardoni, I., Hartig, N., Vollstädt-Klein, S., and Schad, L. R. (2019). The Acute Effects of Cigarette Smoking on Brain Oxygenation and Perfusion Measured by Multi-Parametric Quantitative BOLD and Arterial Spin Labeling MRI: Preliminary Results. In *Proceedings of International Society for Magnetic Resonance in Medicine*, volume 27, page 2925. Montreal, Canada.

Hubertus, S., **Thomas, S.**, Cho, J., Zhang, S., Kovanlikaya, I., Wang, Y., and Schad, L. R. (2019a). MRI-based oxygen extraction fraction and cerebral metabolic rate of oxygen mapping in high-grade glioma using a combined

quantitative susceptibility mapping and quantitative blood oxygenation level-dependent approach. In *Proceedings of International Society for Magnetic Resonance in Medicine*, volume 27, page 0391. Montreal, Canada.

Hubertus, S., **Thomas, S.**, Cho, J., Zhang, S., Wang, Y., and Schad, L. R. (2019d). Comparison of Gradient Echo and Gradient Echo Sampling of Spin Echo Sequence for the Quantification of the Oxygen Extraction Fraction by Combining Quantitative Susceptibility Mapping and Blood Oxygenation Level Dependency. In *Proceedings of International Society for Magnetic Resonance in Medicine*, volume 27, page 2721. Montreal, Canada.

Thomas, S., Hubertus, S., Domsch, S., and Schad, L. R. (2018a). How does the weighting factor in a regularized quantitative BOLD approach affect the estimated oxygen extraction fraction? In *Proceedings of International Society for Magnetic Resonance in Medicine*, volume 26, page 2093. Paris, France.

Thomas, S., Hubertus, S., Förster, A., and Schad, L. R. (2018b). Messung des Sauerstoffverbrauchs im Gehirn einer Glioblastom-Patientin mittels regularisierter qBOLD-Auswertung. In *Proceedings of Jahrestagung der Deutschen Gesellschaft für Medizinische Physik*, volume 21, page 102. Nürnberg, Germany.

Hubertus, S., **Thomas, S.**, Domsch, S. and Schad, L. R. (2017). How do the number of echoes and the echo spacing affect the quality of non-linear field estimates in QSM? In *Proceedings of European Society for Magnetic Resonance in Medicine and Biology*, volume 34, page 105. Barcelona, Spain.

BIBLIOGRAPHY

Akkermans, S. E. A., Luijten, M., van Rooij, D., Franken, I. H. A., and Buitelaar, J. K. (2018). Putamen functional connectivity during inhibitory control in smokers and non-smokers. *Addict Biol*, 23(1):359–368. (Cited on page 87.)

Alsop, D. C., Detre, J. A., Golay, X., Günther, M., Hendrikse, J., Hernandez-Garcia, L., Lu, H., Macintosh, B. J., Parkes, L. M., Smits, M., Van Osch, M. J. P., Wang, D. J. J., Wong, E. C., and Zaharchuk, G. (2015). Recommended implementation of arterial spin-labeled perfusion MRI for clinical applications: A consensus of the ISMRM perfusion study group and the European consortium for ASL in dementia. *Magnetic Resonance in Medicine*, 73(1):102–116. (Cited on pages 33, 34, and 87.)

An, H., Ford, A. L., Vo, K. D., Liu, Q., Chen, Y., Lee, J.-M., and Lin, W. (2014). Imaging oxygen metabolism in acute stroke using MRI. *Current Radiology Reports*, 2(3):39. (Cited on page 1.)

An, H. and Lin, W. (2002a). Cerebral oxygen extraction fraction and cerebral venous blood volume measurements using MRI: Effects of magnetic field variation. *Magnetic Resonance in Medicine*, 47(5):958–966. (Cited on pages 2 and 84.)

An, H. and Lin, W. (2002b). Cerebral venous and arterial blood volumes can be estimated separately in humans using magnetic resonance imaging. *Magnetic Resonance in Medicine*, 48(4):583–588. (Cited on pages 37 and 84.)

Aslan, S., Xu, F., Wang, P. L., Uh, J., Yezhuvath, U. S., van Osch, M., and Lu, H. (2011). Estimation of labeling efficiency in pseudo-continuous arterial spin labeling. *Magnetic Resonance in Medicine*, 63(3):765–771. (Cited on page 34.)

Baker, T. B., Piper, M. E., Stein, J. H., Smith, S. S., Bolt, D. M., Fraser, D. L., and Fiore, M. C. (2016). Effects of nicotine patch vs varenicline vs combination nicotine replacement therapy on smoking cessation at 26 weeks: A randomized clinical trial. *Jama*, 315(4):371–9. (Cited on page 28.)

Bokkers, R. P. H., Hernandez, D. A., Merino, J. G., Mirasol, R. V., van Osch, M. J., Hendrikse, J., Warach, S., Latour, L. L., and On behalf of the, N. (2012). Whole-brain arterial spin labeling perfusion MR imaging in patients with acute stroke. *Stroke*, 43(5):1290–1294. (Cited on page 87.)

Bolar, D. S., Rosen, B. R., Sorensen, A. G., and Adalsteinsson, E. (2011). Quantitative imaging of extraction of oxygen and tissue consumption (QUIXOTIC) using venular-targeted velocity-selective spin labeling. *Magnetic Resonance in Medicine*, 66:1550–1562. (Cited on pages 85 and 87.)

Bouvier, J., Castellani, S., Debacker, C. S., Pannetier, N., Tropres, I., Krainik, A., and Barbier, E. L. (2013). Evaluation of multiparametric qbold in white matter: a simulation study. *Proceedings of the 21st Annual Meeting of ISMRM, Salt Lake City, UT*, page Abstract 2492. (Cited on page 88.)

Bulte, D., Chiarelli, P., Wise, R., and Jezzard, P. (2007). Measurement of cerebral blood volume in humans using hyperoxic MRI contrast. *Journal of Magnetic Resonance Imaging*, 26(4):894–899. (Cited on page 84.)

Bulte, D. P., Kelly, M., Germuska, M., Xie, J., Chappell, M. A., Okell, T. W., Bright, M. G., and Jezzard, P. (2012). Quantitative measurement of cerebral physiology using respiratory-calibrated MRI. *NeuroImage*, 60(1):582–591. (Cited on pages 84 and 85.)

Carpenter, D. A., Grubb, R. L., Tempel, L. W., and Powers, W. J. (1991). Cerebral oxygen metabolism after aneurysmal subarachnoid hemorrhage. *Journal of Cerebral Blood Flow & Metabolism*, 11(5):837–844. (Cited on pages 84 and 85.)

Centers for Disease Control & Prevention, C. D. C. (2010). *How tobacco smoke causes disease: The biology and behavioral basis for smoking-attributable disease: A report of the surgeon general*. (Cited on page 28.)

Cho, J., Kee, Y., Spincemaille, P., Nguyen, T. D., Zhang, J., Gupta, A., Zhang, S., and Wang, Y. (2018). Cerebral metabolic rate of oxygen (CMRO2) mapping by combining quantitative susceptibility mapping (QSM) and quantitative blood oxygenation level-dependent imaging (qBOLD). *Magnetic Resonance in Medicine*, 80(4):1595–1604. (Cited on pages 37 and 88.)

Christen, T., Bolar, D. S., and Zaharchuk, G. (2013). Imaging brain oxygenation with MRI using blood oxygenation approaches : Methods, validation, and clinical applications. *AJNR. American journal of neuroradiology*, pages 1–10. (Cited on pages 26 and 82.)

Christen, T., Lemasson, B., Pannetier, N., Farion, R., Segebarth, C., Remy, C., and Barbier, E. L. (2011). Evaluation of a quantitative blood oxygenation level-dependent (qBOLD) approach to map local blood oxygen saturation. *NMR in Biomedicine*, 24(4):393–403. (Cited on page 3.)

Christen, T., Schmiedeskamp, H., Straka, M., Bammer, R., and Zaharchuk, G. (2012a). Measuring brain oxygenation in humans using a multiparametric quantitative blood oxygenation level dependent MRI approach. *Magnetic Resonance in Medicine*, 68(3):905–911. (Cited on page 3.)

Christen, T., Zaharchuk, G., Pannetier, N., Serduc, R., Joudiou, N., Vial, J.-C., Remy, C., and Barbier, E. L. (2012b). Quantitative MR estimates of blood oxygenation based on T2*: a numerical study of the impact of model assumptions. *Magnetic Resonance in Medicine*, 67(5):1458–68. (Cited on page 82.)

Ciris, P. A., Qiu, M., and Constable, R. T. (2014). Noninvasive MRI measurement of the absolute cerebral blood volume – cerebral blood flow relationship during visual stimulation in healthy humans. *Magnetic Resonance in Medicine*, 72(3):864–875. (Cited on page 37.)

Dickson, J. D., Ash, T. W. J., Williams, G. B., Harding, S. G., Carpenter, T. A., Menon, D. K., and Ansorge, R. E. (2010). Quantitative BOLD: The effect of diffusion. *Journal of Magnetic Resonance Imaging*, 32(4):953–61. (Cited on page 85.)

Diringer, M. N., Yundt, K., Videen, T. O., Adams, R. E., Zazulia, A. R., Deibert, E., Aiyagari, V., Dacey, R. G., Grubb, R. L., and Powers, W. J. (2000). No reduction in cerebral metabolism as a result of early moderate hyperventilation following severe traumatic brain injury. *Journal of Neurosurgery*, 92(1):7–13. (Cited on pages 84 and 85.)

Domino, E. F., Minoshima, S., Guthrie, S., Ohl, L., Ni, L., Koeppe, R. A., and Zubieta, J. K. (2000). Nicotine effects on regional cerebral blood flow in awake, resting tobacco smokers. *Synapse*, 38(3):313–21. (Cited on pages 1 and 28.)

Domino, E. F., Ni, L., Xu, Y., Koeppe, R. A., Guthrie, S., and Zubieta, J. K. (2004). Regional cerebral blood flow and plasma nicotine after smoking tobacco cigarettes. *Prog Neuropsychopharmacol Biol Psychiatry*, 28(2):319–27. (Cited on pages 1 and 28.)

Domsch, S., Mürle, B., Weingärtner, S., Zapp, J., Wenz, F., and Schad, L. R. (2018). Oxygen extraction fraction mapping at 3 Tesla using an artificial neural network: A feasibility study. *Magnetic Resonance in Medicine*, 79(2):890–899. (Cited on pages 3, 41, and 83.)

Evans, A., Collins, D., Mills, S., Brown, E., Kelly, R., and Peters, T. (1993). 3d statistical neuroanatomical models from 305 mri volumes. *1993 IEEE Conference Record Nuclear Science Symposium and Medical Imaging Conference*, 3(1):1813–1817. (Cited on page 34.)

Fan, A. P., Govindarajan, S. T., Kinkel, R. P., Madigan, N. K., Nielsen, a. S., Benner, T., Tinelli, E., Rosen, B. R., Adalsteinsson, E., and Mainero, C. (2014). Quantitative oxygen extraction fraction from 7-Tesla MRI phase: Reproducibility and application in multiple sclerosis. *Journal of Cerebral Blood Flow & Metabolism*, 35(1):131–139. (Cited on page 1.)

Feng, X., Deistung, A., and Reichenbach, J. R. (2018). Quantitative susceptibility mapping (QSM) and R2* in the human brain at 3T: Evaluation of intra-scanner repeatability. *Zeitschrift für Medizinische Physik*, 28(1):36–48. (Cited on page 88.)

Fischl, B. (2012). Freesurfer. *Neuroimage*, 62(2):774–781. (Cited on page 34.)

Gauthier, C. J. and Hoge, R. D. (2012). Magnetic resonance imaging of resting OEF and CMRO2 using a generalized calibration model for hypercapnia and hyperoxia. *NeuroImage*, 60(2):1212–1225. (Cited on page 84.)

Günther, M., Oshio, K., and Feinberg, D. A. (2005). Single-shot 3d imaging techniques improve arterial spin labeling perfusion measurements. *Magnetic Resonance in Medicine*, 54(2):491–498. (Cited on pages 26 and 82.)

Gusnard, D. A. and Raichle, M. E. (2001). Searching for a baseline: Functional imaging and the resting human brain. *Nature*, 2(10):685–694. (Cited on pages 26 and 85.)

Haacke, E. M., Brown, R. W., Thompson, M. R., and Venkatesan, R. (1999). *Magnetic Resonance Imaging: Physical Principles and Sequence Design*. John Wiley and Sons, Inc., Hoboken, NJ, USA. (Cited on pages 6 and 13.)

Hansen, P. C. and O'Leary, D. P. (1993). The use of the L-curve in the regularization of discrete ill-posed problems. *SIAM Journal on Scientific Computing*, 14(6):1487–1503. (Cited on page 41.)

He, X. and Yablonskiy, D. A. (2007). Quantitative BOLD: Mapping of human cerebral deoxygenated blood volume and oxygen extraction fraction: Default state. *Magnetic Resonance in Medicine*, 57(1):115–126. (Cited on pages 35, 88, and 92.)

He, X., Zhu, M., and Yablonskiy, D. A. (2008). Validation of oxygen extraction fraction measurement by qBOLD technique. *Magnetic resonance in medicine*, 60(4):882–8. (Cited on pages 2 and 82.)

Herscovitch, P. and Raichle, M. E. (1985). What is the correct value for the brain-blood partition coefficient for water? *Journal of Cerebral Blood Flow & Metabolism*, 5(1):65–69. (Cited on page 34.)

Hirsch, N. M., Toth, V., Förschler, A., Kooijman, H., Zimmer, C., and Preibisch, C. (2014). Technical considerations on the validity of blood oxygenation level-dependent-based MR assessment of vascular deoxygenation. *NMR in Biomedicine*, 27(7):853–862. (Cited on page 87.)

Hockel, M., Schlenger, K., Mitze, M., Schaffer, U., and Vaupel, P. (1996). Hypoxia and radiation response in human tumors. *Seminars in Radiation Oncology*, 6(1):3–9. (Cited on page 1.)

Hubertus, S. (2019). *Quantitative Susceptibility Mapping to Measure the Local Tissue Oxygenation*. PhD thesis, Heidelberg University. (Cited on pages 7, 12, 14, 24, and 42.)

Hubertus, S., Thomas, S., Cho, J., Zhang, S., Wang, Y., and Schad, L. R. (2019a). Comparison of gradient echo and gradient echo sampling of spin echo sequence for the quantification of the oxygen extraction fraction from a combined quantitative susceptibility mapping and quantitative BOLD (QSM+qBOLD) approach. *Magnetic Resonance in Medicine*. (Cited on page 88.)

Hubertus, S., Thomas, S., Cho, J., Zhang, S., Wang, Y., and Schad, L. R. (2019b). Using an artificial neural network for fast mapping of the oxygen extraction fraction with combined QSM and quantitative BOLD. *Magnetic Resonance in Medicine*. (Cited on pages 3 and 88.)

Ibaraki, M., Shimosegawa, E., Miura, S., Takahashi, K., Ito, H., Kanno, I., and Hatazawa, J. (2004). PET measurements of CBF, OEF, and CMRO2 without arterial sampling in hyperacute ischemic stroke: Method and error analysis. *Annals of Nuclear Medicine*, 18(1):35–44. (Cited on page 1.)

Iida, M., Iida, H., Dohi, S., Takenaka, M., and Fujiwara, H. (1998). Mechanisms underlying cerebrovascular effects of cigarette smoking in rats in vivo. *Stroke*, 29(8):1656–65. (Cited on page 86.)

Ito, H., Kanno, I., Kato, C., Sasaki, T., Ishii, K., Ouchi, Y., and Iida, A. (2004). Database of normal human cerebral blood flow, cerebral blood volume, cerebral oxygen extraction fraction and cerebral metabolic rate of oxygen measured by positron emission tomography with 15 O-labelled carbon dioxide or water, carbon monoxide and oxygen: A multicentre study in Japan. *European Journal of Nuclear Medicine and Molecular Imaging*, 31(5):635–643. (Cited on pages 26, 82, and 84.)

Leenders, K. L., Perani, D., Lammertsma, A. A., Heather, J. D., Buckingham, P., Healy, M. J., Gibbs, J. M., Wise, R. J., Hatazawa, J., Herold, S., Beaney, R. P., Brooks, D. J., Spinks, T., Rhodes, C., Frackowiak, R. S. J., and Jones, T. (1990). Cerebral blood flow, blood volume and oxygen utilization. Normal values and effect of age. *Brain*, 113(1):27–47. (Cited on pages 26, 82, 85, and 87.)

Levitt, M. H. (2008). *Spin Dynamics – Basics of Nuclear Magnetic Resonance. Second edition*. John Wiley and Sons, Ltd., West Sussex PO19 8SQ, England. (Cited on page 5.)

Lu, H., Clingman, C., Golay, X., and van Zijl, P. C. M. (2004). Determining the longitudinal relaxation time (T1) of blood at 3.0 Tesla. *Magnetic Resonance in Medicine*, 52(3):679–682. (Cited on page 34.)

Maier, A., Syben, C., Lasser, T., and Riess, C. (2019). A gentle introduction to deep learning in medical image processing. *Zeitschrift für Medizinische Physik*, 29(2):86–101. (Cited on pages 3 and 84.)

Mie, M. (2011). *Quantification of Brain Tissue Oxygenation: Comparison of Different Gradient Echo/Spin Echo MRI Techniques at 3 Tesla*. PhD thesis, Heidelberg University. (Cited on pages 21, 22, and 27.)

Nasrabadi, N. M. (2007). Pattern recognition and machine learning. *Journal of Electronic Imaging*, 16(4). (Cited on page 3.)

Ogawa, S., Lee, T. M., Kay, A., and Tank, D. (1990). Brain magnetic resonance imaging with contrast dependent on blood oxygenation. *Proc Natl Acad Sci USA*, 87:9868–9872. (Cited on page 2.)

Pauling, L. and Coryell, C. D. (1936). The magnetic properties and structure of hemoglobin, oxyhemoglobin and carbonmonoxyhemoglobin. *Proceedings of the National Academy of Sciences*, 22(4):210–216. (Cited on page 2.)

Raichle, M. E., MacLeod, A. M., Snyder, A. Z., Powers, W. J., Gusnard, D. A., and Shulman, G. L. (2001). A default mode of brain function. *Proceedings of the National Academy of Sciences of the United States of America*, 98(2):676–82. (Cited on page 83.)

Rink, C. and Khanna, S. (2011). Significance of brain tissue oxygenation and the arachidonic acid cascade in stroke. *Antioxidants & Redox Signaling*, 14(10):1889–1903. (Cited on page 1.)

Rofstad, E. K., Sundfør, K., Lyng, H., and Tropé, C. G. (2000). Hypoxia-induced treatment failure in advanced squamous cell carcinoma of the uterine cervix is primarily due to hypoxia-induced radiation resistance rather than hypoxia-induced metastasis. *British Journal of Cancer*, 83(3):354–359. (Cited on page 1.)

Rose, J. E., Behm, F. M., Westman, E. C., Mathew, R. J., London, E. D., Hawk, T. C., Turkington, T. G., and Coleman, R. E. (2003). Pet studies of the influences of nicotine on neural systems in cigarette smokers. *American Journal of Psychiatry*, 160(2):323–333. (Cited on pages 1 and 28.)

Saver, J. L. (2006). Time is brain – quantified. *Stroke*, 37(1):263–266. (Cited on page 1.)

Schnurr, A.-K., Chung, K., Russ, T., Schad, L. R., and Zöllner, F. G. (2019). Simulation-based deep artifact correction with convolutional neural networks for limited angle artifacts. *Zeitschrift für Medizinische Physik*, 29(2):150–161. (Cited on page 3.)

Sedlacik, J. and Reichenbach, J. R. (2010). Validation of quantitative estimation of tissue oxygen extraction fraction and deoxygenated blood volume fraction in phantom and in vivo experiments by using MRI. *Magnetic Resonance in Medicine*, 63(4):910–921. (Cited on pages 82 and 85.)

Shinohara, T., Nagata, K., Yokoyama, E., Sato, M., Matsuoka, S., Kanno, I., Hatazawa, J., and Domino, E. F. (2006). Acute effects of cigarette smoking on global cerebral blood flow in overnight abstinent tobacco smokers. *Nicotine Tob Res*, 8(1):113–21. (Cited on pages 1, 28, and 86.)

Skinhoj, E., Olesen, J., and Paulson, O. B. (1973). Influence of smoking and nicotine on cerebral blood flow and metabolic rate of oxygen in man. *J Appl Physiol*, 35(6):820–2. (Cited on pages 1, 28, and 86.)

Stadlbauer, A., Zimmermann, M., Kitzwogerer, M., Oberndorfer, S., Rossler, K., Dorfler, A., Buchfelder, M., and Heinz, G. (2017). MR imaging-derived oxygen metabolism and neovascularization characterization for grading and IDH gene mutation detection of gliomas. *Radiology*, 283(3):799–809. (Cited on page 1.)

Stanaway, J. D., Afshin, A., Gakidou, E., et al. (2018). Global, regional, and national comparative risk assessment of 84 behavioural, environmental and occupational, and metabolic risks or clusters of risks for 195 countries and territories, 1990-2017: a systematic analysis for the global burden of disease study 2017. *The Lancet*, 392(10159):1923 – 1994. (Cited on pages 1 and 28.)

Sukstanskii, A. L. and Yablonskiy, D. A. (2001). Theory of FID NMR signal dephasing induced by mesoscopic magnetic field inhomogeneities in biological systems. *Journal of Magnetic Resonance*, 151(1):107–117. (Cited on page 35.)

Talhout, R., Schulz, T., Florek, E., van Benthem, J., Wester, P., and Opperhuizen, A. (2011). Hazardous compounds in tobacco smoke. *Int J Environ Res Public Health*, 8(2):613–28. (Cited on page 86.)

Thun, M. J., Day-Lally, C. A., Calle, E. E., Flanders, W. D., and Heath, C. W., J. (1995). Excess mortality among cigarette smokers: changes in a 20-year interval. *Am J Public Health*, 85(9):1223–30. (Cited on page 28.)

Toda, N. and Okamura, T. (2016). Cigarette smoking impairs nitric oxide-mediated cerebral blood flow increase: Implications for alzheimer's disease. *J Pharmacol Sci*, 131(4):223–32. (Cited on page 86.)

Uchida, S., Hotta, H., and Kawashima, K. (2009). Long-term nicotine treatment reduces cerebral cortical vasodilation mediated by alpha4beta2-like nicotinic acetylcholine receptors in rats. *Eur J Pharmacol*, 609(1-3):100–4. (Cited on page 86.)

Ulrich, X. and Yablonskiy, D. A. (2016). Separation of cellular and BOLD contributions to T2* signal relaxation. *Magnetic Resonance in Medicine*, 75(2):606–615. (Cited on page 88.)

Vafaee, M. S., Gjedde, A., Imamirad, N., Vang, K., Chakravarty, M. M., Lerch, J. P., and Cumming, P. (2015). Smoking normalizes cerebral blood flow and oxygen consumption after 12-hour abstention. *J Cereb Blood Flow Metab*, 35(4):699–705. (Cited on pages 1, 28, 86, and 87.)

von Samson-Himmelstjerna, F., Madai, V. I., Sobesky, J., and Günther, M. (2016). Walsh-ordered Hadamard time-encoded pseudocontinuous ASL (WH pCASL). *Magnetic Resonance in Medicine*, 76(6):1814–1824. (Cited on page 87.)

Wang, J. Z., Li, X. A., and Mayr, N. A. (2006). Dose escalation to combat hypoxia in prostate cancer: A radiobiological study on clinical data. *The British Journal of Radiology*, 79(947):905–911. (Cited on page 1.)

Weisskoff, R. M. and Kiihne, S. (1992). MRI susceptometry: Image-based measurement of absolute susceptibility of MR contrast agents and human blood. *Magnetic Resonance in Medicine*, 24(2):375–383. (Cited on page 26.)

Wen, P. Y. and Kesari, S. (2008). Malignant gliomas in adults. *New England Journal of Medicine*, 359(5):492–507. (Cited on pages 1 and 28.)

Whittall, K. P., MacKay, A. L., Graeb, D. A., Nugent, R. A., Li, D. K., and Paty, D. W. (1997). In vivo measurement of T2 distributions and water contents in normal human brain. *Magnetic Resonance in Medicine*, 37(1):34–43. (Cited on page 82.)

Wise, R. G., Harris, A. D., Stone, A. J., and Murphy, K. (2013). Measurement of OEF and absolute CMRO2: MRI-based methods using interleaved and combined hypercapnia and hyperoxia. *NeuroImage*, 83:135–147. (Cited on page 84.)

Yablonskiy, D. A. (1998). Quantitation of intrinsic magnetic susceptibility-related effects in a tissue matrix. Phantom study. *Magnetic Resonance in Medicine*, 39(3):417–428. (Cited on pages 2 and 35.)

Yablonskiy, D. A. and Haacke, E. M. (1994). Theory of NMR signal behavior in magnetically inhomogeneous tissues: The static dephasing regime. *Magnetic Resonance in Medicine*, 32(6):749–763. (Cited on pages 2 and 35.)

Yablonskiy, D. A. and Haacke, E. M. (1997). An MRI method for measuring T2 in the presence of static and rf magnetic field inhomogeneities. *Magnetic Resonance in Medicine*, 37(6):872–876. (Cited on page 35.)

Yablonskiy, D. A., Sukstanskii, A. L., and He, X. (2013). Blood oxygenation level-dependent (BOLD)-based techniques for the quantification of brain hemodynamic and metabolic properties - theoretical models and experimental approaches. *NMR in Biomedicine*, 26(8):963–986. (Cited on page 82.)

Yamamoto, Y., Nishiyama, Y., Monden, T., Satoh, K., and Ohkawa, M. (2003). A study of the acute effect of smoking on cerebral blood flow using 99mtc-ecd spet. *Eur J Nucl Med Mol Imaging*, 30(4):612–4. (Cited on pages 1, 28, 86, and 87.)

Zhang, J., Liu, T., Gupta, A., Spincemaille, P., Nguyen, T. D., and Wang, Y. (2015). Quantitative mapping of cerebral metabolic rate of oxygen (CMRO2) using quantitative susceptibility mapping (QSM). *Magnetic Resonance in Medicine*, 74(4):945–952. (Cited on page 87.)

Zheng, W., Nichol, H., Liu, S., Cheng, Y.-C. N., and Haacke, E. M. (2013). Measuring iron in the brain using quantitative susceptibility mapping and X-ray fluorescence imaging. *NeuroImage*, 78:68–74. (Cited on page 88.)

Zöllner, F. G., Emblem, K. E., and Schad, L. R. (2010). Support vector machines in DSC-based glioma imaging: suggestions for optimal characterization. *Magnetic Resonance in Medicine*, 64(4):1230–1236. (Cited on page 3.)

Zubal, I. G., Harrell, C. R., Smith, E. O., Rattner, Z., Gindi, G., and Hoffer, P. B. (1994). Computerized three-dimensional segmented human anatomy. *Medical Physics*, 21(2):299–302. (Cited on pages 39 and 40.)

Zubieta, J. K., Heitzeg, M. M., Xu, Y., Koeppe, R. A., Ni, L., Guthrie, S., and Domino, E. F. (2005). Regional cerebral blood flow responses to smoking in tobacco smokers after overnight abstinence. *Am J Psychiatry*, 162(3):567–77. (Cited on pages 1, 28, and 86.)